Physical Investigations of Small Particles: (I) Aerosol Particle Charging and Flux Enhancement and (II) Whispering Gallery Mode Sensing

Thesis by

Xerxes López-Yglesias

In Partial Fulfillment of the Requirements
for the Degree of
Physics

California Institute of Technology
Pasadena, California

2013
(Submitted May 13, 2013)

To my parents and grandparents for all their support throughout this endeavor.

Acknowledgments

I would like to take this opportunity to thank my advisor, Rick Flagan, for all his help throughout my time here at Caltech. It has been a pleasure to work with him, as he has been a constant source of ideas and support. Under his guidance my skills as an independent researcher and scientific writer have flourished; I feel well-prepared to tackle my next job.

I would also like to thank Jack Beauchamp, Frank Porter, and John Seinfeld for serving on my thesis defense committee and evaluating this work.

Throughout my time here I have also had the opportunity to work with the talented people of the Flagan/Seinfeld lab group. Within that group, special thanks has to go to a few select people: Jason Gamba is my co-researcher and co-author on the subject of whispering gallery mode sensors, featured later in this work. His camaraderie helped make the work enjoyable even when we were at our wit's end. Andy Downard provided invaluable commentary and scientific discussion on my first charging paper and always interjected a sense of fun and humor into the proceedings. Lindsay Yee read and discussed several early drafts of my second charging paper, by far the longest of my works, with very good humor.

Last but not least, I would like to thank my parents for their love, support, and encouragement in pursuing my dream.

Abstract

Part I

Particles are a key feature of planetary atmospheres. On Earth they represent the greatest source of uncertainty in the global energy budget. This uncertainty can be addressed by making more measurement, by improving the theoretical analysis of measurements, and by better modeling basic particle nucleation and initial particle growth within an atmosphere. This work will focus on the latter two methods of improvement.

Uncertainty in measurements is largely due to particle charging. Accurate descriptions of particle charging are challenging because one deals with particles in a gas as opposed to a vacuum, so different length scales come into play. Previous studies have considered the effects of transition between the continuum and kinetic regime and the effects of two and three body interactions within the kinetic regime. These studies, however, use questionable assumptions about the charging process which resulted in skewed observations, and bias in the proposed dynamics of aerosol particles. These assumptions affect both the ions and particles in the system. Ions are assumed to be point monopoles that have a single characteristic speed rather than follow a distribution. Particles are assumed to be perfect conductors that have up to five elementary charges on them. The effects of three body interaction, ion-molecule-particle, are also overestimated. By revising this theory so that the basic physical attributes of both ions and particles and their interactions are better represented, we are able to make more accurate predictions of particle charging in both the kinetic and continuum regimes.

The same revised theory that was used above to model ion charging can also be

applied to the flux of neutral vapor phase molecules to a particle or initial cluster. Using these results we can model the vapor flux to a neutral or charged particle due to diffusion and electromagnetic interactions. In many classical theories currently applied to these models, the finite size of the molecule and the electromagnetic interaction between the molecule and particle, especially for the neutral particle case, are completely ignored, or, as is often the case for a permanent dipole vapor species, strongly underestimated. Comparing our model to these classical models we determine an "enhancement factor" to characterize how important the addition of these physical parameters and processes is to the understanding of particle nucleation and growth.

Part II

Whispering gallery mode (WGM) optical biosensors are capable of extraordinarily sensitive specific and non-specific detection of species suspended in a gas or fluid. Recent experimental results suggest that these devices may attain single-molecule sensitivity to protein solutions in the form of stepwise shifts in their resonance wavelength, λ_R, but present sensor models predict much smaller steps than were reported. This study examines the physical interaction between a WGM sensor and a molecule adsorbed to its surface, exploring assumptions made in previous efforts to model WGM sensor behavior, and describing computational schemes that model the experiments for which single protein sensitivity was reported. The resulting model is used to simulate sensor performance, within constraints imposed by the limited material property data. On this basis, we conclude that nonlinear optical effects would be needed to attain the reported sensitivity, and that, in the experiments for which extreme sensitivity was reported, a bound protein experiences optical energy fluxes too high for such effects to be ignored.

Contents

List of Figures

List of Tables

Chapter 1

Introduction

In Part I of this work we will examine the description of the kinetics of charge/mass transfer. The kinetics of charge transfer are of vital importance to atmospheric research for reasons of both measurement and basic theoretical understanding of aerosol population development. First, the vast majority of instrumentation used to measure aerosol particles, in either an atmosphere or lab environment, actually only measure the charged fraction of an aerosol population. This is true both of simple particle counters that measure electrical current as a proxy for particle number, and also for more complex systems that segregate particles based on their electrical mobility before counting the populations. For much of the particle size range considered in this paper the only measurement technique that counts all particles, charged or neutral, is a laser particle counter, which, in practice, is almost never used without a mobility analysis stage in front of it. Unfortunately, the fraction of aerosol particles charged can be as little as 0.1% within our range of interest, and from this the total aerosol population is inferred (Hoppel and Frick, 1986). This makes the ability to accurately predict the charge distribution within a given environment vital to accurate measurements. Second, on a more fundamental level, recent theoretical and experimental work strongly suggests that ion-induced nucleation and ion-enhanced particle growth are very important, perhaps the most important, paths to particle formation (Kirkby et al., 2011; Nadykto, 2003; Yu and Turco, 2001), at least within Earth's atmosphere.

The kinetics of mass transfer are also quite relevant to atmospheric research of aerosol particles. The flux of a vapor species to a cluster or nascent aerosol particle is going to partially determine the nucleation rate and the particle growth rate. Classical theories that describe nucleation and condensation, in use today, tend to neglect the finite size of the vapor species and/or the electromagnetic potential between a particle and a vapor species(Lavvas and Griffith, 2011; Nadykto, 2003; Pruppacher and Klett, 1998; Seinfeld and Pandis, 1998; Yu and Turco, 2001). In particular, none of the theories that we are aware of describe the effects of potential between a vapor species and a neutral particle, which make up the vast majority of the particles in the aerosol population for most of the size range considered here.

In order to study the effects outlined above we consider a bath with a majority background gas population and a dilute gas ion/neutral vapor molecule population with aerosol particles suspended in it, and model the flux of the dilute ions/vapor to the particle. The presence of the bath gas changes the problem from one of simply describing a classical two body orbit from some distance away, into a problem that has two distinct limiting case behaviors based on the ratio, Kn=λ/a, of the two length scales present, the radius of the particle, a, and the mean free path of the vapor or ion in the bath gas, λ. The flux of the vapor/ion species towards the particle is analytically described in the limits that Kn$\rightarrow 0$, continuum case, or Kn$\rightarrow \infty$, kinetic case. To bridge the solutions for the limiting cases an approximation is made where the continuum and kinetic flux are made equal at a limiting sphere. This sphere is of order the mean free path away from the particle surface. This approximation, used throughout the rest of this thesis, is based upon the classic work of Fuchs, Natanson, and Keefe et al.(Fuchs, 1963; Keefe, Nolan, and Scott, 1968; Natanson, 1960), who were the first to employ the model to describe an ion flux towards a particle in a background gas.

In Part II of this thesis we re-examine physical processes in whispering gallery mode, WGM, sensors to derive a new model to determine their ultimate sensitivity. Although these devices come in wide variety of geometries, sizes, and compositions, this work will focus on toroidal resonators made of silica with radii of $<200\mu$m. It is in these sensors, in particular, that the highest reported sensitivities have been found, stepwise single molecule detection(Armani, 2010). This level of detection is well outside the bounds of established theory for these devices (Arnold, Khoshsima, and Teraoka, 2003; Arnold, Shopova, and Holler, 2010; Vollmer et al., 2002).

This work was actually begun by my colleague, Jason Gamba, who has a strong background in chemical engineering. I became involved in the work when he found that he needed someone with a strong physics background to complement him and help describe the basic interaction between a single molecule species and the intense electromagnetic field produced by these resonators. Together, we performed a review of the existing theoretical descriptions of this interaction, and then proposed a new model to determine the theoretical lower bound of detectable species' size.

Thesis Outline

Part I of this thesis will review, examine, and revise the theory of ion/vapor flux calculations and, in the case of ions, the steady-state distribution. Chapter 2 begins by describing the existent theory for calculating the steady-state charge distribution of aerosol particles. The assumption of steady-state conditions is re-examined, as is the assumed decoupling of the ion and aerosol populations. Steady-state conditions are generally found to hold true, but the decoupling assumption is found to fail in several realistic instances within Earth's troposphere. In the steady-state distribution, the number of allowed charge states per aerosol particles is increased from 11, for previous theories, to 201, here. This truncation in terms is shown to have large repercussions for particles of radius >0.5 μm. Finally, the actual number of charge states needed to represent the physics as a function of particle size is found. Chapter 3 continues by re-deriving the theory used to calculate ion flux coefficients from the ground up. This new model includes basic physical parameters like the finite-size of the ion and the dielectric constant of both the ion and particle. It also considers the distribution of ion speeds, rather than a single characteristic speed, and re-examines the energy argument for three-body trapping, where the ion collides with a neutral molecule and loses sufficient energy to be caught in the particle's potential well. The potential considered is revised to accommodate dielectrics, and both the ion and the particle can have an image induced on them. The flux coefficients and steady-state charge distribution are re-calculated using the revised theory for different dielectric constant, pressure, and temperature. The revisions lead to significant differences in charge distribution at both the low end and high end of the size range due mainly to the finite size of the ion at the low end and the truncation of terms at the high end. Changing the pressure and temperature leads to massive changes in the predicted distributions, especially for particles smaller than 100 nm. Chapter 4 and 5 both apply the theory developed to calculate ion flux to a particle to instead calculate vapor flux to a particle. All that this actually requires is a change in the potential under examination. Instead of charge-charge and charge-dipole interactions we instead have charge-dipole and dipole-dipole interactions. Many of the classical theories to model vapor flux in an atmosphere omit the effects of the finite size of the molecule and/or the potential that the molecules experience. The model described here is directly compared to those classical models to determine an enhancement factor that describes the importance of the neglected interactions as a function of size. This is specifically done in each of these papers for a few particular systems on Earth and Titan.

In Chapter 6, we move to Part II of this work, where a review of existing WGM theories is discussed, and a new model is proposed and explored.

Appendix A contains a proof for certain approximations made in Chapter 2. Appendix B contains empirical results for the ion flux coefficients and the steady state charge distribution for Chapter 3. Appendix A contains supplemental material to better describe the WGM sensing model used in Chapter 6.

Bibliography

[1] Armani, A (2010). "Single Molecule Detection Using Optical Microcavities," *Photonic Microresonator Research and Applications*, Springer Series in Optical Sciences, Vol. 156, Ed. I.

[2] Arnold, S.; Khoshsima, M.; Teraoka, I.; Holler, S. & Vollmer, F. Shift of whispering-gallery modes in microspheres by protein adsorption *Opt. Lett.*, 2003, 28, 272-274

[3] Arnold, S.; Shopova, S. I. & Holler, S. Whispering gallery mode bio-sensor for label-free detection of single molecules: thermo-optic vs. reactive mechanism *Optics Express*, 2010, 18, 281-287

[4] Fuchs, N.A. (1963). On the Stationary Charge Distribution on Aerosol Particles in a Bipolar Ionic Environment. *Geofis. Pura Appl.* **56**:185-192.

[5] Hoppel, W.A. and Frick, G.M. (1986). Ion-Aerosol Attachment Coefficients and the Steady-State Charge Distribution on Aerosols in a Bipolar Ion Environment. *Aerosol Sci. Technol.* **5**:1-21.

[6] Keefe, D., Nolan, P.J., Scott, J.A. (1968). Influence of Coulomb and Image Forces in Combination of Aerosol. *Proc. R. Irish. Acad.* **60A**:27-44.

[7] Kirkby, J. et al. (2011). Role of sulphuric acid, ammonia and galactic cosmic rays in atmospheric aerosol nucleation. *Nature* **476**:429–433

[8] Lavvas, P., Griffith, CA and Yelle, RV (2011). "Condensation in Titan's atmosphere at the Huygens landing site." *Icarus* 215.2: 732-750.

[9] Nadykto, A. and Yu, F. (2003). Uptake of neutral polar vapor molecules by charged clusters/particles: Enhancement due to dipole-charge interaction. *J. Geophys. Research* **108**:D23:4717.

[10] Natanson, G.L. (1960). On the Theory of Charging of Amicroscopic Aerosol Particles as a Result of the Capture of Gas Ions. *Soviet Physics Technical Physics* **5**:538-551.

[11] Pruppacher, HR and Klett, JD (1998). *Microphysics of clouds and precipitation.*

[12] Seinfeld, J. and Pandis, S. (1998). *Atmospheric Chemistry and Physics.* Wiley, New York, pp. 454-459.

[13] Vollmer, F.; Braun, D.; Libchaber, A.; Khoshsima, M.; Teraoka, I. & Arnold, S. Protein detection by optical shift of a resonant microcavity *Applied Physics Letters*, 2002, 80, 4057-4059

[14] Yu, F. and Turco, R. (1998). The formation and evolution of aerosols in stratospheric aircraft plumes: Numerical simulations and comparisons with observations. *J. Geophys. Research.* **103**:D20:25,915-25,934.

Part I

Aerosol Particles: Charging and Vapor Flux Enhancement

Chapter 2

Population Balances of Micron-Sized Aerosols in a Bipolar Ion Environment

Xerxes López-Yglesias and Richard C. Flagan

The present work re-examines the assumptions that go into place for a steady-state charge distribution analysis to be valid. First, the common approximation that there are only 11 charge states available to the distribution is relaxed to allow for 201 charge states to be available to the particle distribution. This is found to have large repercussions on the behavior of the distribution for radii greater than 0.5 μm. The steady-state assumption itself is then re-examined by calculating the time required to reach steady state for many different ion pair production rates and initial particle charge states as a function of radius. In the steady-state model, the ion populations are often assumed to decouple completely from the aerosol; this is shown to be false throughout the troposphere. Finally, the number of positive and negative charge states needed to accurately model a particle population of a given size is determined.

Introduction

The greatest source of uncertainty in aerosol mobility analysis is the fraction of particles that is counted, largely due to the small number of particles that are charged. Size distribution measurements made using the differential mobility analyzer, DMA, to classify particles according to size therefore require accurate knowledge of the aerosol charge distribution as a function of particle radius (Biskos, 2004; Hoppel and Frick, 1986). Quantitative analysis of aerosols is of paramount importance in understanding the chemical and physical processes that govern atmospheric particle formation and growth. In ambient measurements, errors in the charge distribution could cause nucleation events to be mistaken as noise. To measure aerosol yields in chamber studies, the particle size distribution is monitored as particles grow. Biases due to imperfect knowledge of the fraction of particles that carry charge and that can, therefore, be classified may introduce substantial error in estimates of the amount of secondary organic aerosol formed, a key parameter in studies of the role of aerosols in climate change.

Charge transfer is a well-studied kinetic process, yet questions remain. In the transition size regime, the classic studies by Natanson (1960), Fuchs (1963), and Keefe et al. (1968) describe an ion current through a "limiting sphere". Inside the sphere, one is in the free molecular regime; outside the sphere, one is in the continuum regime. At the boundary, the currents must be equal. Work has continued on the problem since then with contributions from studies by Hoppel and Frick (1986), Lushnikov and Kulmala (2004a), and Lushnikov and Kulmala (2004b), among others. In the present paper, we examine the charge distribution over particles between 1 nm and 10 μm, using the Hoppel and Frick (1986) model, henceforth referred to as HF, which extended the classical description and numerically evaluated the steady-state charge distribution for bipolar, diffusive charging. As in HF, we focus here on the steady-state charge distribution while relaxing computational limitations that were imposed in that earlier work. This steady-state charge distribution both describes the charge state of the atmospheric aerosol and provides the fraction in each possible charge state that is needed to deduce the particle size distribution from mobility analysis data. The present analysis shows that computational limitations in the range of charge states and average ion speeds considered by HF profoundly affect the charge distribution at the upper end of the mobility analysis size range. The resulting changes in the estimated fraction of charged particles are important in estimations of the aerosol mass and volume from DMA measurements.

Models

To deduce the statistical macroscopic charge state of a monodisperse aerosol from the attachment coefficient, one must solve a system of balance equations that describe the time evolution of the ion and aerosol populations (Isreal, 1971). These are simply coupled rate equations, just as are found in model chemical reactions. Assuming a single ion species for each polarity, the ion concentrations, n_1 and n_{-1}, are described by

$$\frac{dn_1}{dt} = q - \alpha n_1 n_{-1} - n_1 \sum_{k=-\infty}^{\infty} \beta_{k,1} N_k \tag{2.1}$$

and

$$\frac{dn_{-1}}{dt} = q - \alpha n_1 n_{-1} - n_{-1} \sum_{k=-\infty}^{\infty} \beta_{k,-1} N_k . \tag{2.2}$$

where N_k is the concentration of particles with charge state k, and q is the rate of creation of new ions per unit volume. Ion recombination is proportional to the product of the concentrations of positive and negative ions. α is the so-called recombination rate coefficient. In the limit of low particle concentrations, N, n_1 and n_{-1} are determined by ion recombination, and the loss of ions to aerosol particles can be decoupled from the ion kinetics. More generally, the particles can influence the ion population, as indicated by the summation of ion-particle charge scavenging rates over particle charge state k.

The ion attachment coefficients, $\beta_{k,i}$, determine the charge distribution, and are calculated as described by the HF model with one exception. The HF model uses two average "characteristic" ion kinetic energies to describe the ion-particle interaction: $4k_{\mathrm{B}}T/\pi$ for uncharged particles and $k_{\mathrm{B}}T$ for charged particles, where k_{B} is the Boltzmann constant and T is temperature. This is a subset of the five "characteristic" kinetic energies described by Keefe et al. (1968). Four energies will be used here: $4k_{\mathrm{B}}T/\pi$ for uncharged particles, $k_{\mathrm{B}}T$ for attractive interactions with charged particles, $1.25k_{\mathrm{B}}T$ for attractive interactions with charged particles larger than 1μm, and $1.5k_{\mathrm{B}}T$ for repulsive interactions. This slight extension will improve the estimate of the required number of charge states as a function of particle size later in this paper.

The ions are assumed to carry only one elementary charge, a good approximation in the limit of small ions. The time evolution of the aerosol population is

$$\frac{dN_k}{dt} = \beta_{k-1,1} n_1 N_{k-1} - \beta_{k,1} n_1 N_k + \beta_{k+1,-1} n_{-1} N_{k+1} - \beta_{k,-1} n_{-1} N_k, \tag{2.3}$$

assuming that there are no particle sources or sinks, and that the particles only change charge states through ion attachment. It then logically follows that the total charge per unit volume,

$$\rho_0 = \mathrm{e}\left(n_1 - n_{-1} + \sum_{k=-\infty}^{\infty} k N_k\right), \tag{2.4}$$

and total particle concentration,

$$N_T = \sum_{k=-\infty}^{\infty} N_k, \tag{2.5}$$

are conserved. Equations (2.1-2.5) can be solved to determine the time-dependent charge distribution.

In bipolar diffusion charging, the charge distribution asymptotically approaches a steady-state at which

$$\left(\frac{dN_k}{dt}\right)_{ss} = 0 = \beta_{k-1,1} n_1 N_{k-1} - \beta_{k,1} n_1 N_k + \beta_{k+1,-1} n_{-1} N_{k+1} - \beta_{k,-1} n_{-1} N_k.$$

The ratio of concentration in successive charge states is found to be

$$\frac{N_k}{N_{k-1}} = \frac{\beta_{k-1,1} n_1}{\beta_{k,-1} n_{-1}\left(1 + \frac{\beta_{k,1} n_1}{\beta_{k,-1} n_{-1}} - \frac{\beta_{k+1,-1}}{\beta_{k,-1}} \frac{N_{k+1}}{N_k}\right)}. \tag{2.6}$$

For $k \to K$ large enough such that both $\frac{\beta_{k,1} n_1}{\beta_{k,-1} n_{-1}}$ and $\frac{\beta_{k+1,-1}}{\beta_{k,-1}} \frac{N_{k+1}}{N_k}$ are arbitrarily close to 0, Eq. (2.6) can be approximated[1] by

$$\frac{N_K}{N_{K-1}} = \frac{\beta_{K-1,1} n_1}{\beta_{K,-1} n_{-1}}. \tag{2.7}$$

The steady-state approximation implies that Eq. (2.7) is true for all k. In the past, this relationship has been incorrectly invoked without proof as an expression of microscopic reversibility, which would imply that a captured ion can be re-emitted by the capturing particle. The rate of such charge emission is negligible near room temperature, so charge equilibrium will not be established on any reasonable time scale. Instead, charged particle neutralization occurs via preferential attachment of ions with charge opposite of that of the particle, leading to the hypothesized steady-state charge distribution.

We may relate the concentration of particles in a given charge state to that of neutral particles by multiplying successive concentration ratios, i.e.,

$$\frac{N_k}{N_0} = \prod_{l=1}^{k} \frac{N_l}{N_{l-1}}. \tag{2.8}$$

This number can be used to construct the ratio of the total particle concentration to that of neutral particles,

$$\frac{N_T}{N_0} = \sum_{k=-K^-}^{K^+} \frac{N_k}{N_0} \tag{2.9}$$

where K^+ is the maximum charge state k considered in the positive direction, and K^- is the maximum charge state k considered in the negative direction. The fraction of particles in charge state k then becomes

$$\frac{N_k}{N_T} = \frac{N_k/N_0}{N_T/N_0}. \tag{2.10}$$

Similar expressions can be obtained for negatively charged particles. It is worth noting that the value for K^+ or K^- that is needed to account for all charged particles is **strongly** size dependent, e.g., virtually no particles smaller than 10 nm will acquire

---

[1] See Appendix A for details.

more than one charge, while most supermicron particles will be multiply charged. The limiting k values in the positive and negative directions are not necessarily symmetric due to differences in the mobilities of positive and negative ions. In plasma environments, which rely on the same underlying physics, particles can actually hold a large fraction of the negative charge in the system (Khrapak and Morfill, 2009). In this study, the values for mobility and mass from HF are used: 150 AMU and $1.2 \cdot 10^{-4} \mathrm{m}^2 \mathrm{V}^{-1} \mathrm{s}^{-1}$ for positive ions and 90 AMU and $1.35 \cdot 10^{-4} \mathrm{m}^2 \mathrm{V}^{-1} \mathrm{s}^{-1}$ for negative ions.

In the discussion that follows, we examine the effect of the values of K^+ and K^-on the estimate of the steady-state charge distribution, extending our calculations well beyond the limits employed by HF, $K^+_{HF} = K^-_{HF} = 5$; this value was chosen to model particles of up to ∼500 nm in radius at typical atmospheric conditions. One reason for this cut off was likely computational limitations of the time. In our return to this topic, we first examine the steady-state charge distribution and the number of charges, $K^\pm$, that must be considered. We then explore the time required to achieve that steady-state distribution, and the effect of the ion production rate on both the charge distribution and the time required to achieve it by using a transient model, which was integrated using a fifth-order Runge-Kutta-Fehlberg algorithm. The transient model assumes that creation and destruction of ions occur uniformly throughout the volume, and that the equations describing the evolution of the population of ions and the aerosol are **not** decoupled, as they were in the HF model.

Results and Discussion

In the following discussion, we consider the addition of more “characteristic” kinetic energies in the calculation of flux coefficients and the determination of flux coefficients for high charge states that were excluded from the calculations of HF. The flux coefficients calculated using the HF model and the present model are shown in Fig. 2.1. The inclusion of more kinetic energies leads to a slight enhancement in the flux coefficient during repulsive interactions for particles less than 200 nm in radius.

Otherwise the present model agrees well with the HF model for all flux coefficients previously calculated. Although the effect of this extension to HF on the flux coefficients is small, it will eliminate nonphysical behavior as we evaluate the effects of truncating the sums in calculating the steady-state charge distribution.

Before we discuss the resultant steady-state charge distribution from these flux coefficients, we should ask a much more basic question: Is the steady-state approximation valid for the DMA measurements to which they are normally applied? To answer this, we undertook a general study of $n\tau_{ss}$, where τ_{ss} is the time it takes the charged fraction of the particle population to reach steady state, as a function of particle size, and n is the negative ion population (which varies by $< 10\%$ from the positive ion population in all subsequent calculations). These transient simulations examine ion-aerosol systems in which the ion-pair creation rate was varied between $4.33 \cdot 10^{11}$ ions/(cm^3·s), a typical ion pair production rate for a 2 mCi Po neutralizer (Cooper and Reist, 1973), and 2 ions/(cm^3·s), the rate at the bottom of the troposphere. The recombination coefficient was held at $3{\cdot}10^{-6}$ cm^3/s (Cooper and Reist, 1973), and the aerosol concentration was held at 10 particles/cm^3, with all particles beginning neutral. For all of these cases τ_{ss} was defined as the time it takes for the charged particle population to reach 90% of its asymptote. The results are shown in Fig. 2.2 as a function of particle size. No significant changes were observed to result from changing the ion pair production rates. However, a spot check at different initial particle charges led to significant changes in $n\tau_{ss}$. This deviation suggests that the initial particle charge distribution may have a significant effect on τ_{ss}. τ_{ss} becomes undefined at large particle size for all the initially charged particle populations because the final charged particle population deviates no more than 10% from the initial charged particle population or because the value overshoots by greater than 10% after first approach. More concretely, for an aerosol population that begins neutral, the time to achieve 99% of the steady-state value was 6 ms or less for 1 nm to 10 μm radii particles with concentrations ranging from 10 particles/cm^3 to 10^6 particles/cm^3 at ion concentrations of $3.8 \cdot 10^8$ ions/cm^3. At a concentration of 10^7 particles/cm^3 with particles of 10 μm radius the time increased to 17 ms at the same ion concentra-

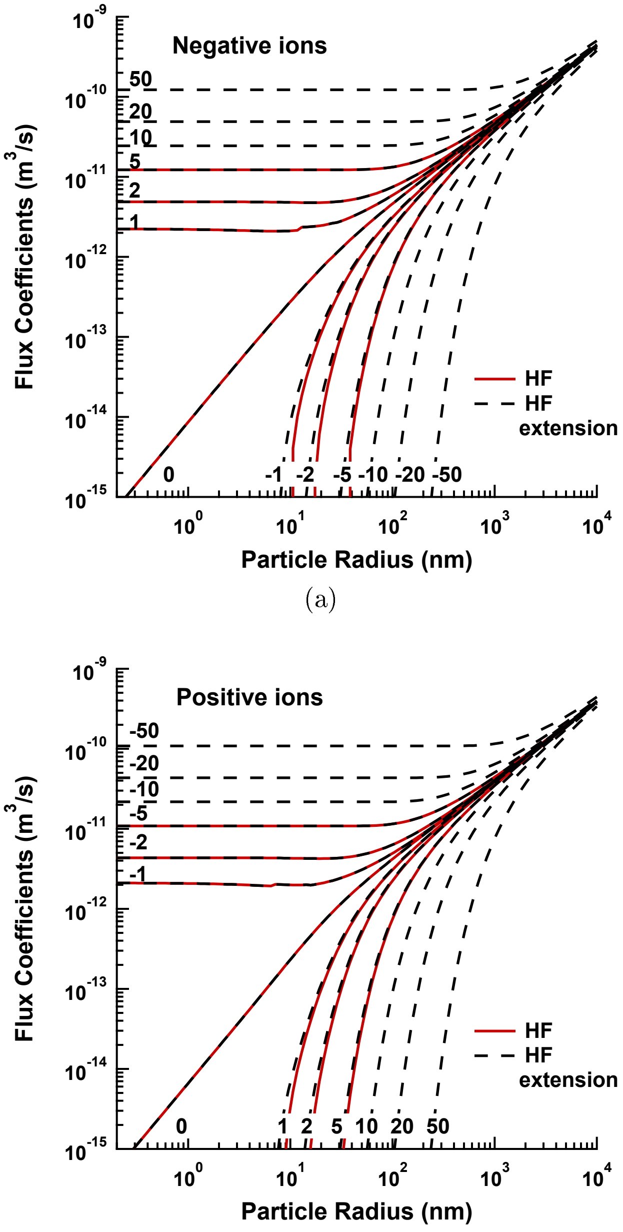

(a)

(b)

Figure 2.1: Flux coefficients for negative, (a), and positive, (b), ions to aerosol particles of various charge states.

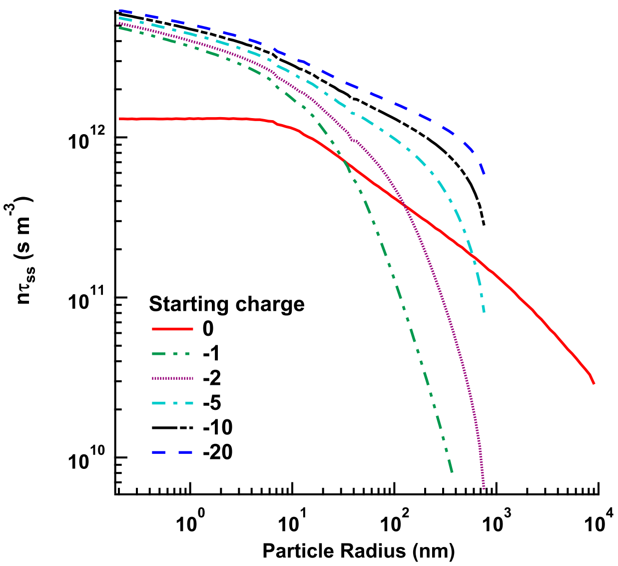

Figure 2.2: The product of the ion concentration and the time to reach steady state as a function of particle radius. Each curve represents a different starting charge for the particle population.

tion. With typical residence times of 3 seconds or greater in a neutralizer, the aerosol particles achieve the steady-state charge distribution within the neutralizer.

The resultant steady-state charge distributions calculated using $K^+ = K^- = 5$, as in the HF model, is shown in Fig. 2.3. Here it is compared to the distribution calculated by extending the HF model to $K^+ = K^- = 100$ and including more "characteristic" kinetic energies. This more closely approximates the full Maxwellian ion velocity distribution. The truncation of the ion charge in the HF model leads all charge states to approach an asymptote at large particle sizes. In contrast, when the charge states are not so artificially bound, the fraction of particles in any given charge state decreases with size, but the fraction of charged particles ($k \neq 0$) asymptotically approaches unity. In contrast, the inclusion of the extra kinetic energies leads to only small shifts in the distribution, most readily noted in the populations of doubly charged aerosol at small size.

There is one other possible source of deviation that bears mentioning at this point. At high aerosol loading or low ion pair production, the assumption made in the steady-state solutions that the aerosol and ion population evolution are decou-

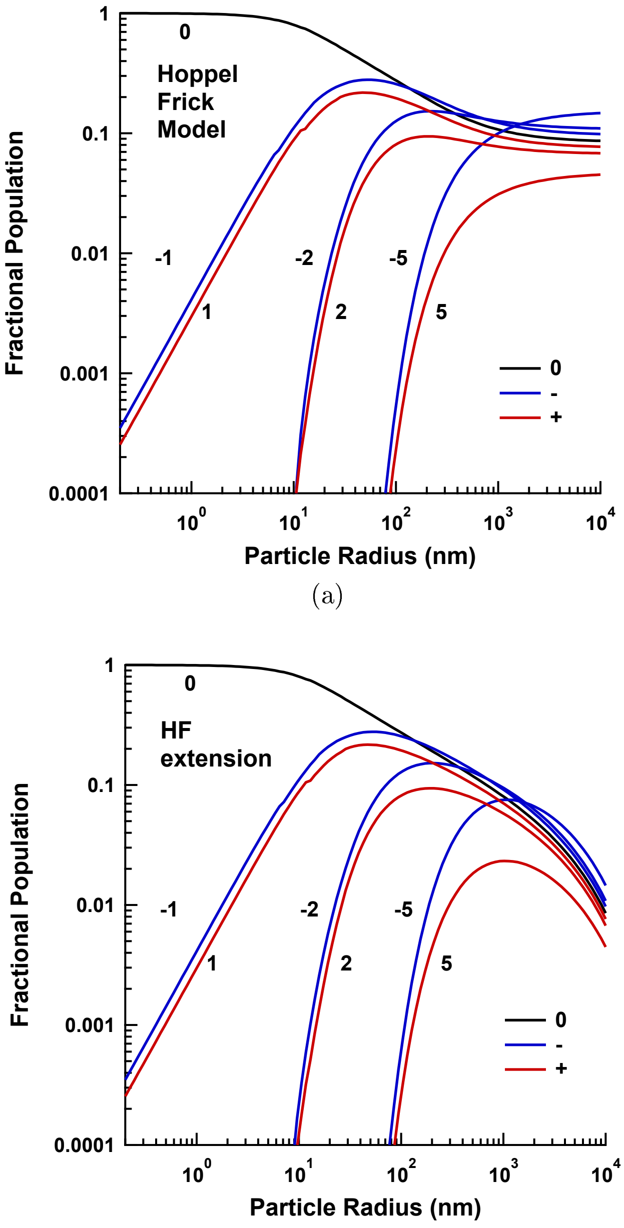

(a)

(b)

Figure 2.3: Steady state charge distributions for the HF model, (a), and the HF extended model, (b).

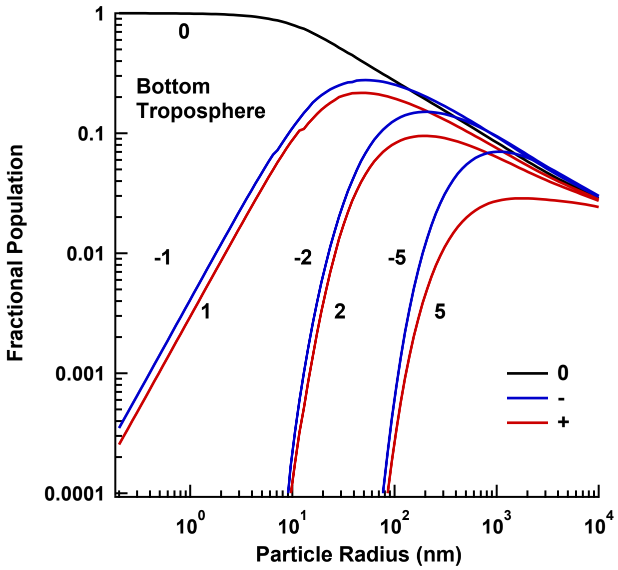

Figure 2.4: At large particle size the steady-state distribution in the troposphere is distributed due to the strong coupling between the ion and aerosol populations. This figure shows the distribution at the bottom of the atmosphere where the ion-pair production rate, ~2 $\text{cm}^{-3}\text{s}^{-1}$, is at its lowest, leading to the largest distortion.

pled breaks down at larger particle radii. Here, the population of highly charged states seriously alters the steady state ion concentration. For 10 μm particles this results in a deviation of 0.6%, 6%, 76%, and 260% from the decoupled solutions for concentrations of 10^4, 10^5, 10^6, and 10^7 particles/cm^3 respectively, assuming an ion pair production rate of $4.33 \cdot 10^{11}$ ions/(cm^3·s). This creates a distribution that lies somewhere between the original HF results and the present results. This population coupling is also exhibited in complex plasmas and in the troposphere due to the low ion pair production rates there. Figure 2.4 shows the bottom, 2 ions/(cm^3·s) and 10 particles/cm^3, of the troposphere with low aerosol loading. Further enhancement of the aerosol population or decrease in ion pair production will only exaggerate the distortion.

For the purpose of calculating both the transient and steady-state solutions described above, $K^{\pm}$ was assumed to be 100. However, this is far more terms than the calculation actually requires. A minimum value for each polarity must be established.

To that end, Fig. 2.5a presents the relationship between the fraction of the aerosol in a neutral charge state and the maximum number of negative charge states, K^-, allowed in the model. From this, we can infer K^-_{min}, the minimum number of negative charge states required to accurately describe the charge distribution at a given particle size. The points of charge K^-_{min} are represented as solid circles in Fig. 2.5a. They are defined as the point where the aerosol fraction reaches 99% of its asymptotic value. K^+_{min} can be determined in a similar fashion. $K^\pm_{min}$ are plotted as a function of particle size in Fig. 2.5b. The insets to this graph show discrete charge distributions at a few selected sizes. They show that the particle size and ion mobility greatly skew the resultant distribution.

Because charge is quantized, the increase in $K^\pm_{min}$ with respect to particle radius occurs in discrete steps. The points at the edge of each of these steps, represented in Fig. 2.5b as a filled diamond or a square with a cross through it, are fit to find the underlying functional form. The much greater mobility of the negative ions is shown to cause a wide disparity in the minimum number of charge states required for each polarity and in their functional form. K^-_{min} follows a power law,

$$K^-_{min} = C_0 a^t, \tag{2.11}$$

where $C_0 = (1.016 \pm .041) \cdot 10^5 \text{ m}^{-t}$, $t = 0.6597 \pm 0.0033$, and a is the particle radius. The additional ion kinetic energies mentioned above reduce the error in this fit. K^+_{min}, instead, follows a log normal distribution,

$$K^+_{min} = C_1 \exp(-[\ln(a - a_0)/w]^2), \tag{2.12}$$

where $C_1 = 10.55 \pm 0.19$, $a_0 = (8.25 \pm 1.25) \cdot 10^{-6}$ m, and $w = 3.42 \pm 0.16$ m. The underlying physical reason for this behavior is beyond the scope of this study, but the functional forms shown here may still allow others to budget their computing resources more appropriately.

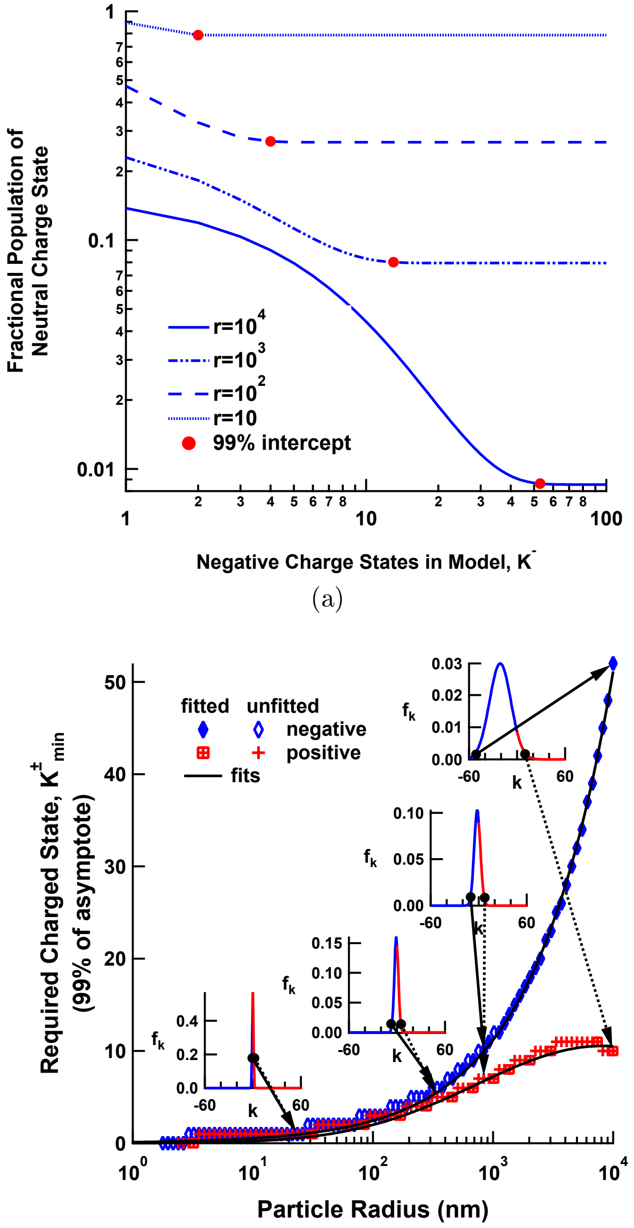

(a)

(b)

Figure 2.5: The fraction of the aerosol in a neutral charge state is given as a function of maximum, negative charge, K^-, in (a), where the solid circles show the points at 99% of the asymptotic values. These latter points are given as a function of particle size and fitted in (b), while the inset graphs show the charge distribution at a given size.

Conclusions

The Hoppel and Frick (1986) model has been extended to include higher charge states and more "characteristic" ion kinetic energies. This does little to affect the previously calculated flux coefficients, but the higher charge states prove very important at large particle radius, where it becomes increasingly likely that these states are populated. This creates huge differences in the resultant steady-state distribution at large size, where the previous model approaches an artificial asymptote at all charge states and the current model has a decreasing fractional population at all charge states.

The assumption that the particle distribution reaches steady-state for typical experimental neutralizer setups is also re-examined and found valid. A general dependence of the time required to achieve steady-state as a function of particle size and initial particle charging is shown. The assumptions that the ion and aerosol populations can be decoupled is verified for the most common cases. General calculations of the time to reach steady state based on the particle size and a few individual charge states are provided.

The assumption that the two populations under consideration, ions and particles, are decoupled is found to be dependent on aerosol loading and particle size; it is valid to within 6% for all particle sizes up to an aerosol concentration of 10^5 particles/cm^3 within a typical neutralizer. Calculating the minimum charge state necessary to accurately model a particle population of a given size allows us to determine a functional dependence with respect to the radius. We find that the negative charge states follow a power law, while the positive charge states follow a log normal distribution due to the large difference in their mobilities. Including more characteristic ion energies proves useful in reducing the error of this calculated power law. This raises several questions about the kinetics of ion capture, and, specifically, the approximation of an average ion velocity. These concerns will be addressed in a paper to follow.

Acknowledgments

We thank Andrew Downard for his time spent editing and discussing this manuscript. We would also like to thank the NASA Astrobiology Institute through the NAI Titan team managed at JPL under NASA Contract NAS7-03001 for the funding of this project, the Ayrshire Foundation for their support in making computing resources available, and Aerosol Science and Technology for their permission to reproduce this article, first published there, in my thesis.

Bibliography

[1] Biskos, G. (2004). *Theoretical and Experimental Investigation of the Differential Mobility Spectrometer.* University of Cambridge, Cambridge.

[2] Cooper, D.W. and Reist, P.C. (1973). Neutralizing Charged Aerosol with Radioactive Sources. *J Colloid Interface Sci*, Vol 45, No 1

[3] Fuchs, N.A. (1963). On the Stationary Charge Distribution on Aerosol Particles in a Bipolar Ionic Environment. *Geofis. Pura Appl.* **56**:185-192.

[4] Hoppel, W.A. and Frick, G.M. (1986). Ion-Aerosol Attachment Coefficients and the Steady-State Charge Distribution on Aerosols in a Bipolar Ion Environment. *Aerosol Sci. Technol.* **5**:1-21.

[5] Isreal, H. (1971). *Atmospheric Electricity*, Israel Program for Scientific Translations, Jerusalem.

[6] Keefe, D., Nolan, P.J., Scott, J.A. (1968). Influence of Coulomb and Image Forces in Combination of Aerosol. *Proc. R. Irish. Acad.* **60A**:27-44.

[7] Khrapac, S. and Morfill, G. (2009). Basic Processes in Complex (Dusty) Plasmas: Charging, Interactions, and Ion Drag Force. *Contrib. Plasma Phys.* 49, No. 3, 148 – 168.

[8] Lushnikov, A.A. and Kulmala, M. (2004b). Charging of aerosol particles in the near free-molecule regime. *Eur. Phys. J. D* **29**:345-355.

[9] Lushnikov, A.A. and Kulmala, M. (2004a). Flux-matching theory of particle charging. *Phys Rev E* **70**:046413.

[10] Natanson, G.L. (1960). On the Theory of Charging of Amicroscopic Aerosol Particles as a Result of the Capture of Gas Ions. *Soviet Physics Technical Physics* **5**:538-551.

Chapter 3

Ion-Aerosol Flux Coefficients and the Steady State Charge Distribution of Aerosols in a Bipolar Ion Environment

Xerxes López-Yglesias and Richard C. Flagan

Fuchs' theory, as corrected by Hoppel and Frick, is widely used to compute flux coefficients of ions to aerosol particles and the resultant charge distribution. We have identified approximations made in previous works that limit the theory's accuracy. Hoppel and Frick used 2 characteristic speeds or kinetic energies to calculate the flux coefficients of ions to aerosol particles in lieu of an average of the flux coefficients over the Maxwell-Boltzmann distribution of ion speeds. In the present work we show that this approximation artificially reduces the number of multiply charged particles. Ion capture may be enhanced by three-body trapping, a process wherein an ion has a collision with a neutral gas molecule and loses sufficient kinetic energy to be captured by the particle. The gas kinetic theory approach to three-body trapping has been refined to better account for the collision between the ion and a neutral gas molecule within the potential presented by the particle. Approximations to the calculation of energy losses and the probability of ion capture have been relaxed. The possibility that an image charge may be induced on the ion as well as on the particle is allowed. While the previous work was limited to electrically conductive particles, both the ion

and the particle are allowed to have any dielectric constant in the present work, and the finite size of the ions is taken into account when calculating minimum capture radii for the ion-particle interactions. The resulting ion flux coefficients differ from previous results both in the low nanometer regime, and in the continuum regime. We explore the influence of key parameters on the charge distribution, including dielectric constant, temperature, and pressure, to understand how operating conditions may affect the interpretation of differential mobility analyzer measurements of particle size distributions. Finally, an empirical expression for the new charge distribution is given to facilitate rapid calculations.

Nomenclature

$a_{p/i/g}$ = radius of particle/ion/gas

$a_g^{'}$ = enhanced radius of interaction between an ion and gas molecule

A = $(1 - 4\cos^2\varepsilon\frac{M_{gas}M_{ion}}{(M_{gas}+M_{ion})^2})^{1/2}$, a dimensionless parameter in three body trapping

b = modified interaction cross-section radius

b_{HF} = modified interaction cross-section radius for three body trapping in Hoppel Frick

b_0 = square root of the minimum physical $b^2(c_0)$

b_δ = b_0 for three body trapping

B_i = numerical fit coefficient

c = speed of ion at $r < r_0$

c_0 = speed of ion at r_0

$\bar{c}$ = mean speed of ion

c_c = cut-off speed in repulsive interactions

c_{char} = characteristic speed of ion in Keefe et al. (1968) approximation

c_f = speed of ion after collision with gas molecule

c_g = speed of ion at $r < r_1$

c_{g0} = speed of gas molecule at r_1

$c^{'}$ = speed of ion in reference frame with gas molecule at rest

$c_g^{'}$ = speed of gas molecule in reference frame where gas molecule is at rest
D_{ion} = diffusivity of ion
e = elementary charge
E = energy in the ion particle system
f = probability of ion capture
F = normalized Maxwell distribution
$g(k)$ = numerical approximation function
G = electric field produced by ion
h = maximum charge state, negative
H = ion-ion trapping distance
i = ion charge
$I_{k,i}$ = ion current of charge i to particle of charge k
j = index of charge states
$J_{k,i}$ = flux of ion with charge i to particle of charge k
k = number of charges on particle
k_B = Boltzmann constant
l = angular momentum
m = induced dipole moment
$M_{ion/gas}$ = mass of ion/gas molecule
n = concentration of ions
N_k = concentration of particles in charge state k
N_T = total aerosol concentration
$p_{i/if/g/gf}$ = momentum/final momentum of ion/gas
$p_{i/if/g/gf}^{'}$ = momentum/final momentum of ion/gas in frame $c_g^{'} = 0$
P = pressure
P_0 = initial pressure
q = ion creation rate per unit volume
r = distance from ion to aerosol particle
r_a = radius of smallest escape orbit apsoid
r_f = radius where force on ion is zero in repulsive interactions

r_{HF} = $\lambda_i + r_a$ or $\lambda_i + \delta$, whichever is greater, r_0 as used by Hoppel and Frick (1986)

$r_{0/1}$ = radius where ion/gas molecule begins its relevant lifespan

s = distance between ion and neutral gas molecule

S_c = Sutherland's constant

t = time

T = temperature

T_0 = initial temperature

W = Hoppel Frick change in potential for three body trapping

x = distance from center of ion/particle to portion of distributed image charge

y = maximum charge state, positive

α = ion recombination coefficient

$\beta_{k,i}$ = flux coefficient of an ion of charge i to a particle of charge k

$\gamma_{i/p}$ = $\frac{\chi_{i/p}-\chi_0}{\chi_{i/p}+\chi_0}$, a dimensionless parameter for calculating image charge

Γ = dimensionless factor of order unity

δ = three body trapping radius

Δ = potential energy between ion and gas molecule

ε = angle between p'_{gf} and particle's radial vector

ϵ_0 = permittivity of free space

η = viscosity of gas

θ = three body trapping angle

θ_c = critical angle demarcation between two and three body trapping

$\lambda_{i/g}$ = mean free path of ion/gas

μ_i = ion mobility

$\Xi_{i0/g0/i1/g1}$ = kinetic energy of an ion/gas molecule at r_0/just before collision

$\xi_{p/i}$ = $\frac{a_{p/i}^2}{r^2}$, a dimensionless parameter for calculating image charge

ρ = r_a or δ, whichever is greater

$\upsilon_{p/i}$ = $\frac{rx}{a_{p/i}^2}$, a dimensionless parameter for calculating image charge

$\phi_{k,i}$ = potential energy between an ion of charge i and a particle of charge k

$\chi_{i/p/0}$ = dielectric constant of ion/particle/atmosphere

ψ = potential energy between gas molecule and particle

Ω = polarizability

Introduction

When an aerosol is exposed to the gas ions produced by radioactive decay in a so-called *aerosol neutralizer,* the charge distribution asymptotically approaches a steady-state in which most particles in the submicron size regime carry at most one electrical charge. Classification of those particles that do acquire charge enables measurement of the particle size distribution. Over the past few decades, the differential mobility analyzer (DMA), the primary instrument used for such measurements, has been refined to enable high resolution measurement of particle mobility and, hence, size. While mobility-based particle size measurements can be made with high precision and accuracy, the charge distribution in the aerosol population is based upon models that, as will be shown below, involve a number of questionable assumptions. The charging probability thus remains the greatest source of uncertainty in mobility-based size distribution measurements.

In addition to its role in the measurement of fine aerosol particles, charge also influences the dynamics of the atmospheric aerosol. Gas ions can initiate particle formation at lower supersaturations than would be required for homogeneous nucleation of neutral vapor molecules (Nadykto and Yu, 2003; Yu and Turco, 1998). Recent studies have also shown that aerosol particle charge can enhance particle growth rates (Lushnikov and Kulmala, 2004; Tammet and Kulmala, 2005). These effects, known as ion-mediated nucleation, are the subject of numerous recent studies on the origins of new particles in the low nanometer size regime, both in the ambient atmosphere and in laboratory studies aimed at unraveling the mechanisms of new particle formation and understanding why observed nucleation and growth rates exceed those predicted by homogeneous nucleation theory.

Atmospheric ions are formed by radioisotope decay at the Earth's surface and by cosmic rays throughout the atmosphere. By reducing the barrier to nucleation, these ions are hypothesized to accentuate new particle formation and accelerate particle growth. Evidence for ion-mediated nucleation has been found in studies of atmospheric nucleation events by measuring the size distributions of the as-formed particles using DMAs without an external charge source. Laboratory measurements have also probed the role of ions in new particle formation. One such experiment is the Cosmics Leaving OUtdoor Droplets (CLOUD) experiment in which a pion beam from the proton synchrotron at CERN is used to simulate the cosmic ray intensity in the upper troposphere and lower stratosphere (Kirkby et al., 2011). In that experiment, an ion-clearing electric field enables experiments in which only neutral nucleation is possible. The different observations under neutral conditions and when ions are produced by galactic cosmic rays, or at higher rates by the pion beam, reveal that atmospheric ions substantially enhance the rate of new particle formation over that when no ions are present, or when ions are present only at low concentrations.

Knowledge of the charging kinetics is central to the interpretation of data obtained in all of these experiments. While mobility resolution of DMA measurements is high, uncertainty in the fraction of particles charged remains large. That uncertainty will similarly affect predictions of ion-mediated nucleation and growth rates and, thereby, impact the numbers of fine particles in the atmosphere. Theoretical descriptions of kinetics of charge transfer from gas ions to particles is based upon the classic works of Fuchs (1963), Natanson (1960), and Keefe et al. (1968) that employed a so-called "limiting-sphere model" to account for non-continuum effects on ion capture by neutral and charged aerosol particles. Most estimates of the charge distribution employ the extensions of Hoppel and Frick (1986), who identified and resolved a number of approximations in the classical theory. That study will be referred to as HF throughout this work. These approximations include: (i) ignoring image charge; and (ii) neglecting three-body trapping, wherein a collision of an ion with a neutral gas molecule reduces the kinetic energy of the ion sufficiently to enable trapping by a particle. HF also identified errors in the original theory, notably the assumption that the minimum capture radius for attractive ion-particle collisions must be the particle radius. The latter error was shown to lead to significant changes in the distribution of charged states, especially for particles with radii below about 10 nm. With these improvements, the HF model forms the basis for most discussion of the charge state of aerosols. Wiedensohler (1988) facilitated the wide use of this model by developing an empirical fit to the HF predictions that enables estimation of the steady-state charge distribution produced by bipolar diffusion charging without having to undertake detailed simulations of ion-particle collisions. To extend the fit to particles with more than $2e$ of charge, Wiedensohler applied an analytical expression from Gunn and Woessner (1956), which is valid for large particles.

Nature of Ion-Particle Interactions

In the discussion that follows, we re-examine Fuchs (1963) in light of HF's extension to Fuchs' model, and identify additional approximations and assumptions that limit the scope and/or accuracy of the ion flux coefficient predictions. The ion fluxes are used to predict the steady-state charge distribution in bipolar diffusion charging. Correcting the unnecessary assumptions alters the charging kinetics and the steady-state charge distribution for the low nanometer regime. Our model also incorporates the changes to the ion fluxes at large particle size explored in López-Yglesias and Flagan (2013). To facilitate use of the new predictions, an empirical fit to the charge distribution is provided, analogous to the approach of Wiedensohler (1988). In order to facilitate direct comparison with the earlier work, we employ the ion properties from HF. The predictions of HF using these properties accurately reproduced experimentally observed charging in the intermediate size range; we shall show below that our present model agrees with the earlier predictions in this regime.

As in the earlier studies, we are interested in charge transfer to particles ranging in size from the free molecular limit to the continuum regime, and employ the limiting-sphere model to span that range of diffusive Knudsen numbers, $\mathrm{Kn}_i = \lambda_i/a_p$ where λ_i

is the mean free path of the ion, not the gas, and a_p is the particle radius. The limiting sphere, or flux-matching model describes transport of ions to the particle surface from an outer region where continuum drag models are applied to describe the combined diffusive and electrophoretic migration fluxes. The resultant ion flux is matched to the flux that is predicted by kinetic theory in an inner region that extends outward from the particle surface a distance $\Gamma\lambda_i$ where Γ is a factor of order unity. To develop a quantitative model of the charge transfer process, we must understand all the forces that contribute to the interaction between the ion and the particle in both regimes. The key challenge in describing the charge transfer process arises in the modeling of transport in the inner region where forces between the particle and the ion lead to complex ion trajectories. From analyses of the orbital mechanics corresponding to different initial ion positions, trajectories, and velocities at the limiting sphere we seek to determine ensemble average ion fluxes to the particle surface. In the Fuchs/HF analyses, these fluxes are typically presented as attachment coefficients, with the implicit assumption that all charge that reaches the particle surface attaches to that surface. While the sticking probability can reasonably be expected to be unity for large particles, recent emphasis on charging of particles that approach molecular dimensions raises the need for caution. At the smallest sizes, the chemistry of charge transfer may lead to attachment probabilities lower than unity; therefore, we describe the kinetic parameters as ion flux coefficients. In the analysis of steady-state charge distributions, we will explicitly assume that the attachment probability is unity, but note that, below some as-yet-to-be-determined size, this assumption will break down. As with the prior work, the present model only considers the transport processes, not the charge transfer chemistry. Some of these chemical effects on aerosol diffusion charging are explored in Premnath et al. (2011).

The approach taken in this paper begins with the interaction between an ion and an aerosol particle, a two-body process. Charge is transferred from the ion to the particle by direct collision. To determine whether or not such a collision takes place, we examine the motion of an ion starting from a distance $r_0 = \Gamma\lambda_i + a_p + a_i$ from the center of the particle, where a_i is the radius of the ion. If there were no interaction force between the ion and the particle, charge transfer could occur only if the initial ion trajectory were to bring it within a distance $r_a = a_p + a_i$ from the center of the particle. r_a is thus the radius that defines the interaction cross section of the two bodies, πr_a^2.

To account for all Coulombic interactions between the particle and the ion we must examine the potential energy between an ion of charge i and a particle of charge k,

$$\phi_{k,i}(r) = \frac{e^2}{4\pi\chi_0\epsilon_0 r}\left(ik - \gamma_p\xi_p^{\frac{3}{2}}\int_0^1 d\upsilon_p\frac{\upsilon_p^{(1-\gamma_p)/2}}{2(1-\upsilon_p\xi_p)^2} - k^2\gamma_i\xi_i^{\frac{3}{2}}\int_0^1 d\upsilon_i\frac{\upsilon_i^{(1-\gamma_i)/2}}{2(1-\upsilon_i\xi_i)^2}\right), \tag{3.1}$$

where e is the electron charge, r is the distance between the ion and the particle, $\gamma_{i/p} = \frac{\chi_{i/p}-\chi_0}{\chi_{i/p}+\chi_0}$, χ_0 is the dielectric constant for the bulk gas, $\chi_{i/p}$ is the dielectric constant for the ion/particle respectively, x is the distance from the center of the ion or particle to a portion of the distributed charge, $\upsilon = \frac{rx}{a^2}$, and $\xi = \frac{a^2}{r^2}$. The first term of the potential is the simple Coulombic potential between two point charges. The second/third terms of the potential are the result of the image charge induced by the ion/particle on the particle/ion. The integral in the second/third terms sum the contribution to the potential from the interaction between the two induced images within the particle/ion and the source charge ion/particle. There are two differences of note between the second and third terms: there is a factor of k^2 in the third term because, unlike the ion, the particle can be multiply charged, and the radii, υ and ξ, are of the ion, not of the particle. This potential was derived by Neumann (1883), who treated the general problem of the electric potential due to source charges, placed inside or outside of a sphere of any dielectric value, and their resultant image charges (Norris, 1995). When a dielectric sphere is exposed to a source charge, there will be two images induced in the sphere to balance the charge. In the case that the dielectric constant of the sphere is larger than that of the surrounding medium, a point charge of opposite polarity from the source charge is induced a distance $\frac{a_{p/i}^2}{r}$ from the center of the sphere. There is also an image charge distribution of similar polarity to the source charge that extends from the image point charge back to the the origin of the sphere. This system of induced and source charges is shown in Fig. 3.1. This potential expands upon the works of Natanson (1960) and Keefe et al. (1968), who only considered the potential between the point charges and the image charge induced on a conductive particle. This description of interaction could still be further improved upon for the smallest particle sizes by accurately taking into account the constituent components of the particle (Amadon and Marlow, 1991a; Amadon and Marlow, 1991b).

Before we apply this new potential, an accurate description of the particle and ion is needed. For an aqueous particle we can assume that the particle is a charged conductor that allows charge to redistribute itself across the surface. On the other hand, for a solid, dielectric particle, e.g., a dry polystyrene bead, we assume that the charge is in the center of the particle and immobile. When the ion approaches the particle, it will induce redistribution of the charge in the particle.

Depending on its properties, the ion involved in the above interaction may be described either as a collection of constituent molecules or as a large, single, continuous entity. A small ion or ionic cluster is well described as a charge embedded in an unpolarizable material. A better description of the near interaction between the ion and particle in such a case would require detailed information about both the ion and the particle surface chemistry, and is well outside the scope of this paper. On the other hand, a large ion cluster can be modeled as a charge fixed in the center of a dielectric sphere. In each case the interaction cross-section is altered by the Coulomb interaction. For a particle whose kinetic energy is significantly greater than its potential energy, $r_a \approx a_i + a_p$. However, as the particle slows down, there are distinct limiting interaction radii for the attractive and repulsive cases. In the attractive case, the ion capture orbit can increase in size until it reaches a maximum at $r_a = r_0$, where the ion's relevant life began. In the repulsive case, the force includes two components: the force between the source charges, and the force exerted by the induced images on the sources. If, as in Earth's atmosphere, the dielectric constant of the particle and/or ion is greater than that of the surrounding atmosphere, then the

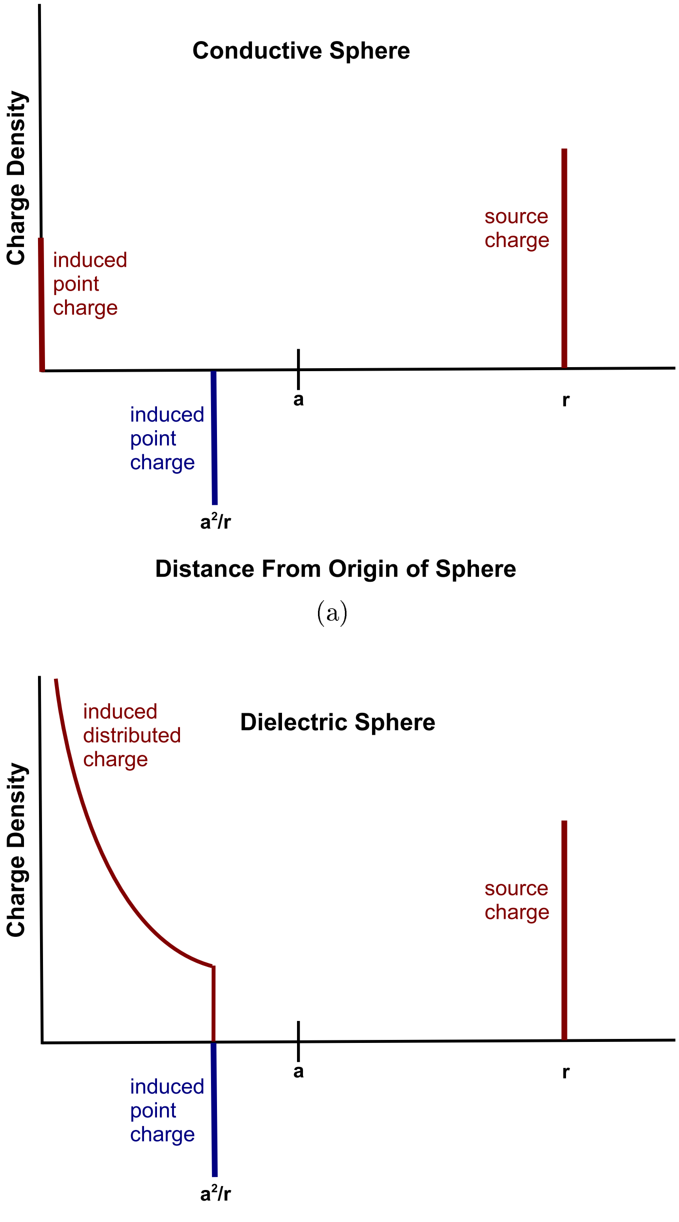

(a)

(b)

Figure 3.1: Charges induced on a (a) conductive or (b) dielectric sphere of radius a by a point charge at $r > a$. The origin here is the center of the sphere. It is assumed that the dielectric constant of the sphere in (b) is greater than its surroundings.

images induced on them will exert an attractive force that may exceed the repulsive force between the source charges. There exists a radius, r_f, where these two forces cancel. In order for the ion to be captured, it must have enough kinetic energy to reach $r_a = r_f$ or $r_a = a_i + a_p$, whichever is greater. The ion's trajectory towards the particle surface is, therefore, curved towards/away from the particle due to the attractive/repulsive forces between the two. This lensing effect will alter the capture cross-section presented to ions approaching the particle. The radius of this modified capture cross-section will be called b_0, as illustrated in Fig. 3.2. And, if $r_a = r_0$, it's maximum value, then $b_0 = r_0$ as well.

Lastly, we consider the effect of adding a third body to the interaction between the ion and the particle, a neutral gas molecule. An ion with too much kinetic energy to be trapped by the Coulomb force described above may still strike a neutral gas molecule and lose sufficient energy to be trapped in the particle's potential well. Three-body trapping is only relevant in attractive interactions, where a smaller kinetic energy aids ion capture.

Now that we have introduced the relevant physical interactions in the system, we can proceed with the construction of a model.

Modeling Flux Coefficients

We begin this process with a few physical parameters in hand that we will use to derive several other relevant parameters. We are given the ion mobilities at a set temperature and pressure and the ion masses, as well as the gas characteristics and the ambient atmospheric conditions from HF. From this we can derive the mean free paths of the ions and the gas, as well as the effective radius of each.

For ions, the base property is the ion mobility, μ_i, which will ultimately be used to calculate both the mean free path and effective radius. According to the kinetic theory of gases for hard sphere molecules, the ion mobility varies with temperature, T, and pressure, P, according to $\mu_i(T, P) = \mu_i(T_0, P_0)\frac{P_0 T}{P T_0}$, where the subscript 0 denotes a reference state at which the mobility is known. Although in air ion mobilities cannot

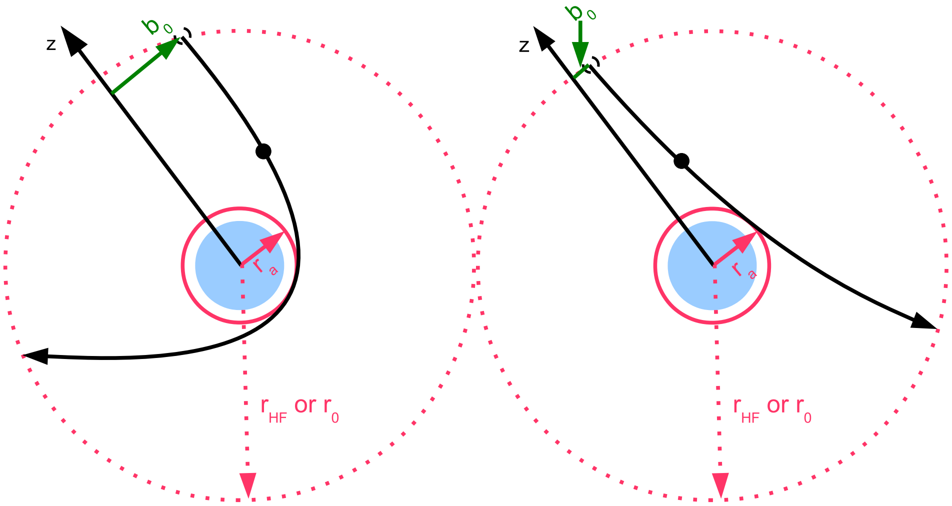

(a) (b)

Figure 3.2: Critical orbit, showing the boundary between capture and escape for ions with a given kinetic energy approaching a particle with (a) opposite charge and (b) similar charge.

actually be determined using hard sphere relationships due to the polarizability of the gases, the scaling relationships for pressure and temperature should still hold true (Tammet, 1995). Attractive and repulsive forces between the ions and the surrounding gas molecules can become important at low temperatures or high densities, when the potential energy begins to swamp the kinetic energy (Loeb, 1939). The diffusivity is related to the mobility through the Einstein relation, $D_{ion} = \frac{\mu_i k_B T}{\mathrm{e}}$. Here, k_B is the Boltzmann constant, and e is the electric charge. The mean free path of the ion is $\lambda_i = 32 D_{ion} / \left(3\pi \left(1 + \frac{M_{ion}}{M_{gas}} \right) \bar{c} \right)$, consistent with HF (Seinfeld and Pandis, 1998; Hoppel and Frick, 1986). M_{ion} and M_{gas} are the masses of the ion and gas respectively, and $\bar{c} = (\frac{8 k_B T}{\pi M_{ion}})^{\frac{1}{2}}$ is the mean speed of the ion. For the gas molecules, the mean free path and effective radius can be estimated from the viscosity, η. The viscosity varies with T according to Sutherland's formula, $\eta(T) = \eta(T_0) \frac{T_0 + S_c}{T + S_c} (\frac{T}{T_0})^{\frac{3}{2}}$ where the subscript 0 refers to a know viscosity reference state. Here, S_c is the so-called Sutherland's constant, which depends on gas composition. The mean free path of the gas molecules is, therefore, $\lambda_g = \frac{2\eta}{P \bar{c}}$ (Seinfeld and Pandis, 1998). The effective radius of a gas molecule, $a_g = (\frac{M_{gas} T k_B}{16 \pi^3 \eta^2})^{\frac{1}{4}}$, is calculated by equating two formulations for the mean free path, one based on gas viscosity, and the other on the interaction cross section between the gas molecules. The effective radius of an ion in the gas,

$$a_i = -a_g + \left(3(1 + \frac{M_{ion}}{M_{gas}})^{\frac{1}{2}} \bar{c} \frac{k_B T}{8PD_{ion}} \right)^{\frac{1}{2}}, \tag{3.2}$$

is calculated in the same manner (Seinfeld and Pandis, 1998).

With these relations in hand, the interactions between individual particles discussed in the background section can be used to determine the behavior of the ensemble. We have assumed that the only force acting upon the ion is exerted by a central ion/particle. This is a good approximation when the concentration of ions in the atmosphere is dilute. This is true at atmospheric temperatures for $n_i^{1/3} \ll 10^4$ ions/m^3, where n_i is the total concentration of ions of charge i (Natanson, 1959; Fuchs, 1947). In this dilute limit, the force exerted by the atmospheric ions is negligible (Natanson, 1959).

Following Natanson (1960) and Fuchs (1963) we consider transport in two regions: (1) an outer region where a continuum transport model is applied, and (2) an inner region that begins approximately one ion mean free path from the particle surface. Ion transport in this outer region is described by the convective diffusion equation,

$$\frac{\partial n_i}{\partial t} + \nabla \cdot J_{k,i} = 0, \tag{3.3}$$

where

$$J_{k,i} = (D_i \frac{\partial n_i}{\partial r} + \mu_i (\nabla \phi_{k,i}) n_i) \tag{3.4}$$

describes the ion flux of species i to a particle of charge k. This flux includes both the Brownian diffusion and electrophoretic migration as a result of the Coulomb force between the ion and the particle. If $(n_i \rho^3)^{1/2} \ll 1$ and $q\rho^3 \ll 1$: ρ is the ion capture radius about the particle, and q is the volumetric ion creation rate, so that ion destruction and creation events are very rare (Natanson, 1959; Fuchs, 1947), then at ambient temperatures one can also assume that the diffusive flow is stationary,

$$\frac{\partial n_i}{\partial t} = 0. \tag{3.5}$$

Combining Eqns. (3.3), (3.4), and (3.5) we obtain

$$\nabla \cdot (D_i \frac{\partial n_i}{\partial r} + \mu_i (\nabla \phi_{k,i}) n_i) = 0 \tag{3.6}$$

Integrating over the entire limiting sphere surface yields the ion current of species i to a particle of charge k in the continuum regime,

$$I_{k,i}^{(C)} = 4\pi r^2 (D_i \frac{\partial n_i}{\partial r} + \mu_i (\nabla \phi_{k,i}) n_i). \tag{3.7}$$

Integrating Eq. (3.7) subject to the boundary condition that the ion concentration far from the particle surface is

$$n_i(r = \infty, t) = n_{i0} \tag{3.8}$$

yields the steady-state current,

$$I_{k,i}^{(C)} = 4\pi D_i \frac{n_{i0} - n_i(r) \exp(\phi_{k,i}(r)/k_B T)}{\int_r^\infty r^{-2} \exp(\phi_{k,i}(r)/k_B T) dr}. \tag{3.9}$$

This ion current in the outer region, where this continuum model applies, must match that of the inner kinetic region,

$$I(c_0)_{k,i}^{(K)} = \pi c_0 b_0^2 (c_0) f(c_0) n_i(r_0) \tag{3.10}$$

at the radius of the limiting sphere, $r_0 = a_i + a_p + \Gamma \lambda_i$. For the purposes of this model we shall assume that $\Gamma = 1$ based on the best fit model curve of Keefe (1967). The microscopic current within the limiting sphere is, in general, proportional to the ion density. (Henceforth, λ_i can be taken as $\Gamma \lambda_i$ in order to relax this assumption.) $f(c_0)$ is the probability that the ion will be captured by the particle; c_0 is the ion speed at

r_0; and b_0 is the modified cross-section radius. By setting the two currents equal at the limiting sphere, we can solve for n_i. In the dilute limit considered here, the ion current is proportional to the ion concentrations, so we define a flux coefficient as

$$\beta(c_0)_{k,i} = I(c_0)_{k,i}/n_i(\infty). \tag{3.11}$$

Using Eqns. (3.9) and (3.10) this becomes

$$\beta(c_0)_{k,i} = \frac{\pi c_0 b_0^2(c_0) f(c_0) \exp(\frac{-\phi_{k,i}(r_0)}{k_B T})}{1 + \pi c_0 b_0^2(c_0) f(c_0) \exp(\frac{-\phi_{k,i}(r_0)}{k_B T})(4\pi D)^{-1} \int_{r_0}^{\infty} r^{-2} \exp(\frac{\phi_{k,i}(r)}{k_B T}) dr}. \tag{3.12}$$

This flux coefficient depends on the molecular speed of the ion. We seek the average for all aerosol particles of a given size. Natanson (1960) found this by calculating the ensemble average in several limiting cases, but did not solve for the general form of $\langle \beta_{k,i} \rangle$. Keefe et al. (1968) simplified this more general computation by calculating $\langle c_0 b_0^2(c_0) \rangle$, and estimating $\langle \beta_{k,i} \rangle$ by substituting this value for $c_0 b_0^2(c_0)$ in Eq. (3.12). He compared these estimates with those obtained substituting different values of c_0 into Eq. (3.12) to identify a characteristic ion speed, c_{char}, for which this $\beta(c_{\text{char}})_{k,i} \approx \langle \beta_{k,i} \rangle$ for a given particle/ion combination. HF use two of these characteristic speeds from Keefe in their calculations, one for ion-neutral particle interactions, and the other for ion-charged particle interactions.

The use of a characteristic value for c_0 oversimplifies the estimation of $\langle \beta_{k,i} \rangle$, as can readily be seen for repulsive interactions. Consider a Maxwellian distribution of ion speeds, which has a long tail on the high speed end of the distribution. In spite of the repulsive interaction, some small fraction of the ions will always have sufficient kinetic energy to overcome the repulsive forces and reach the particle surface, a fact that is overlooked in the Keefe et al. (1968) and HF models. Keefe et al. (1968) also introduced a questionable renormalization to his estimate of $\langle c_0 b_0^2(c_0) \rangle$ for repulsive interactions. Our analysis eliminates all of these unnecessary approximations. However, it still does not consider the effects of a strong potential on the ion speed and trajectory at the limiting sphere (Gopalakrishnan and Hogan, 2012).

We follow Natanson and calculate

$$\langle \beta_{k,i} \rangle = \int_0^\infty \beta(c_0)_{k,i} F(c_0, T) dc_0$$

using the normalized Maxwellian speed distribution, $F(c_0, T)$, without approximation to obtain the final form of the flux coefficient. However, to evaluate $\langle \beta_{k,i} \rangle$, we must first find $b_0(c_0)$ and $f(c_0)$.

We begin with the derivation of $b_0(c_0)$ by examining the equation of motion of the ion for escape orbits. For any ion that escapes, energy and angular momentum are conserved, so the total energy of the system is

$$E = \phi(r) + \frac{M_{ion} c^2}{2} = \phi(r_0) + \frac{M_{ion} c_0^2}{2} \tag{3.13}$$

where c is the speed of the ion at any $r < r_0$. c^2 can be broken into its radial and tangential components, so

$$E = \phi(r) + \frac{M_{ion}}{2}(\dot{r}^2 + r^2 \dot{\theta}^2). \tag{3.14}$$

The tangential component can be written in terms of the ion's angular momentum, l, as

$$E = \phi(r) + \frac{1}{2}\left(M_{ion} \dot{r}^2 + \frac{l^2}{M_{ion} r^2} \right). \tag{3.15}$$

The radial velocity thus becomes

$$\dot{r} = \left(2 \frac{E - \phi(r) - \frac{l^2}{2mr^2}}{M_{ion}} \right)^{1/2}. \tag{3.16}$$

Applying the chain rule to $\dot{r}$ yields

$$\dot{r} = \dot{\theta} \frac{dr}{d\theta} = \frac{l}{M_{ion} r^2} \frac{dr}{d\theta}. \tag{3.17}$$

Thus,

$$\frac{dr}{d\theta} = r\left(\frac{2M_{ion}r^2E}{l^2} - 1 - \frac{2\phi(r)M_{ion}r^2}{l^2}\right)^{1/2}. \tag{3.18}$$

The angular momentum, $l = M_{ion}c_0\sin(\theta)r$, is conserved throughout the ion's orbit, as there is no torque on the ion. Defining $b(c_0) \equiv r\sin(\theta)$, the angular momentum becomes $l = M_{ion}c_0b(c_0)$. If we choose a Cartesian coordinate system, CS1, with its origin at the center of the aerosol particle and the z-axis antiparallel to the initial trajectory of the ion, then $b(c_0)$ is a line segment perpendicular to the z-axis, connecting the axis to the ion at r_0. The minimum $b(c_0)$ to describe an escape orbit is b_0. Substituting l into Eq. 3.18 yields

$$\frac{dr}{d\theta} = r^2\left(b^{-2}(c_0) - r^{-2} - 2M_{ion}^{-1}c_0^{-2}b^{-2}(c_0)\left[-\phi(r_0) + \phi(r)\right]\right)^{1/2}. \tag{3.19}$$

The minimum radius of closest approach, r_a, where $\frac{dr}{d\theta} = 0$ is called the apsoid. For a given apsoidal radius,

$$b^2 = (r_a)^2\left(1 - 2\frac{\phi(r_a) - \phi(r_0)}{M_{ion}c_0^2}\right). \tag{3.20}$$

b_0 must now be found. Only b_0 for which

$$r_0 \geq r_a(b_0) \geq a_i + a_p \tag{3.21}$$

are physically attainable. The upper bound limits the solution to ions that approach the particle. The lower bound is set by the sum of the radii of the two bodies, where the ion would make physical contact.

This can be mathematically determined by finding the apsoidal radius, r_a, at which b^2 is a minimum, i.e.,

$$\frac{\partial b^2}{\partial r_a} = 0, \tag{3.22}$$

subject to the constraint that

$$\frac{\partial^2 b^2}{\partial r_a^2} > 0.$$

If this mathematical minimum leads to $r_a > r_0$, we find $b_0 = r_0$ and $r_a = r_0$, since the capture cross-section radius cannot exceed that of the limiting sphere. If $r_a < a_i + a_p$, we find $b_0 = 0$ and $r_a = a_i + a_p$. For a repulsive interaction wherein the ion has insufficient kinetic energy to achieve physical contact with the particle, the capture cross-section diminishes to 0. Since only deterministic two-body (ion + particle) interactions have been considered at this point, $f(c_0) = 1$. This constraint will be relaxed when random collisions of the ions with background gas molecules are taken into account in the discussion of so-called "three-body trapping."

In the HF model, the boundary between the diffusive and the free molecular regime is defined by $r_{HF} = r_a + \lambda_i$, so

$$b_{HF}^2 = (r_a)^2 \left(1 - 2\frac{\phi(r_a) - \phi(r_{HF})}{M_{ion}c_{\text{char}}^2}\right). \tag{3.23}$$

A more general form of this equation allows the two radii at which the potential is evaluated to be varied to account for electrostatic lensing between the two points:

$$b_{HF}^2(r_1, r_2) = (r_1)^2 \left(1 - 2\frac{\phi(r_1) - \phi(r_2)}{M_{ion}c_{\text{char}}^2}\right). \tag{3.24}$$

The HF limiting sphere radius, r_{HF}, can only be used if a constant characteristic value is assumed for the initial ion speed. In the present model we consider the entire Maxwellian speed distribution. This includes low speeds for which $r_a \to \infty$ as the ion's kinetic energy goes to 0. This implies that $r_{HF} \to \infty$ as does the capture cross-section, b_{HF}. More problematically, this means that the capture cross-section, b_{HF}, is defined in terms of a different limiting sphere radius, r_{HF}, for each c. Instead, we begin our calculations at r_0, where an ion begins with a speed c_0 with probability $F(c_0, T)$.

Three-Body Trapping

Presently, our limiting sphere model assumes that only two bodies, the ion and particle, exist within that sphere. But the mean free path is just that, a mean distance between collisions. The ion still has a finite probability of collision within the limiting sphere. If it does collide, the ion's energy will be altered, possibly leading to capture. This mechanism dominates charge capture in dusty plasmas (Khrapak and Morfill, 2009). This interaction, known as three-body trapping in the atmospheric literature, and as charge-exchange collision in the field of dusty plasmas, is illustrated in Fig. 3.3. In the present model, the ion is considered captured if it has insufficient kinetic energy to escape the limiting sphere after collision with a neutral gas molecule. By approximating the background gas as a homogeneous, isotropic medium, the probability that an ion with a given trajectory will collide with a neutral gas molecule may be calculated using the Beer-Lambert law.

To calculate the energy loss required for capture, we must consider the details of the ion-gas collision in the aerosol particle potential well. The ion begins a distance r_0 away from the center of the particle, having just undergone its last random collision. Unless a collision occurs, the ion has kinetic energy

$$\Xi_{i1} = \frac{1}{2}M_{ion}c_0^2 + \phi(r_0) - \phi(r) + \Delta(|\vec{r_0} - \vec{r_1}|) - \Delta(a_g + a_i) = \frac{1}{2}M_{ion}c^2, \tag{3.25}$$

where ϕ is the potential between the ion and the particle, and $\triangle$ is the potential between the ion and the gas molecule. The molecule begins a distance $r_1 = a_g + a_p + \lambda_g$ away from the center of the particle and has kinetic energy,

$$\Xi_{g1} = \frac{1}{2}M_{gas}c_{g0}^2 + \psi(r_1) - \psi(r) + \Delta(|\vec{r_0} - \vec{r_1}|) - \Delta(a_g + a_i) = \frac{1}{2}M_{gas}c_g^2 \tag{3.26}$$

where ψ is the potential between the molecule and the particle, and c_{g0} and c_g are the gas molecule speed at r_1 and $r < r_1$, respectively. In order to develop a simple model that accurately characterizes the interaction between the three bodies, we would like

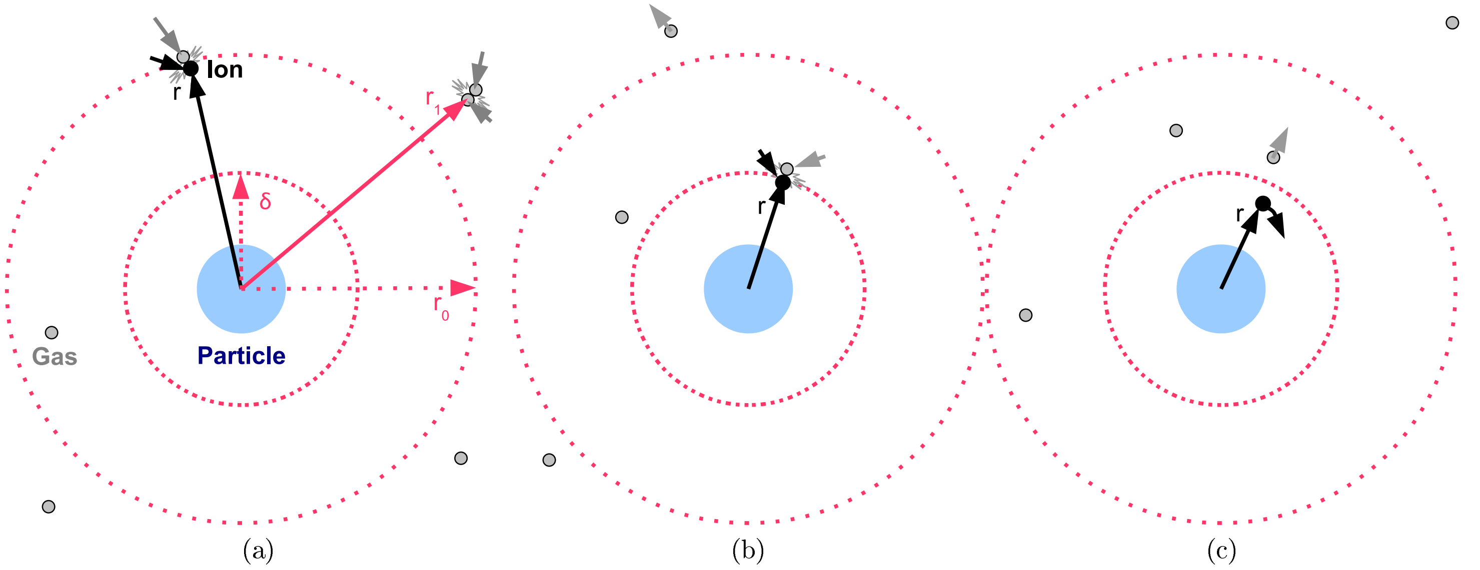

Figure 3.3: Schematic of the steps involved in three body capture. (a) The ion undergoes its last random scattering at radius r_0. (b) The ion collides with a gas molecule at radius $r \leq \delta$, losing kinetic energy. (c) The ion enters a collision course with the particle.

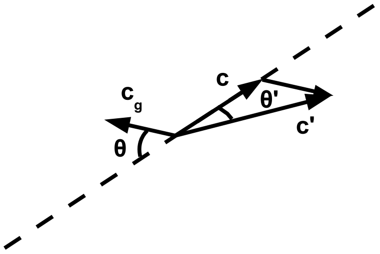

Figure 3.4: Conversion to primed frame.

to model the interaction between the ion and the molecule as the interaction between two 3-D, perfectly elastic spheres where $\Delta(r) = 0$. This is possible if the deflection of the trajectories by the attractive force is sufficiently short ranged. To describe how, we move into a frame of reference centered on the molecule,

$$c_g^{'} = 0. \tag{3.27}$$

Here

$$c^{'} = ((c + c_g \cos\theta)^2 + c_g^2 \sin^2\theta)^{1/2} = (c^2 + c_g^2 + 2cc_g \cos\theta)^{1/2} \tag{3.28}$$

where θ and $\theta^{'}$ are illustrated in Fig. 3.4. Now, as illustrated in Fig. 3.5, an attractive force between the two species will curve the ion's path towards the molecule. However, far from the molecule, the trajectory of the ion, both before and after collision, will reach an asymptote. This asymptotic trajectory can also be reached with two perfectly elastic spheres with no potential between them if the effective radius of the gas molecule is increased. We calculate this enhanced radius in the same manner as the impact parameter for an ion moving towards a particle,

$$(a_g^{'})^2 = (a_g + a_i)^2 \left[1 - 2\left(\Delta(a_g + a_i) - \Delta(a_g + a_i + \lambda_i)\right)\left(M_{ion}(c^{'})^2\right)^{-1}\right], \tag{3.29}$$

where the ion travels a mean free path to reach the gas molecule. In Earth's atmosphere the vast majority of gas molecules have no permanent electric dipole moment, so

$$m = \Omega G : \frac{\Omega}{4\pi\epsilon_0} \approx 2 \times 10^{-30}\mathrm{m}^3, \tag{3.30}$$

where m is the induced dipole moment for N_2 or O_2; Ω is the polarizability of the molecule; ϵ_0 is the permittivity of free space; and G is the field produced by the ion. This implies that the potential energy between the molecule and the ion is

$$\Delta = \frac{-m \cdot G}{2} = \frac{-\Omega |G|^2}{2} = -\frac{\Omega e^2}{2(4\pi\epsilon_0)^2 s^4}, \tag{3.31}$$

where s is the radial distance between the ion and the molecule.

The positive and negative ions present depend on the composition and relative humidity of the gas (Lee et al., 2005). To determine the extent to which the ion-molecule potential may influence these collisions, we note that the H_3O^+ and OH^- are common ions in Earth's atmosphere, and apply the molecular radius of water, 0.2 nm, to make an upper bound estimate of the effect. This underestimates the ion size and overestimates its mobility since most atmospheric ions are clusters of water molecules around an ionized core. For the gas molecule we assume a radius of 0.1 nm since this is a fair representation of N_2 or O_2. For a gas molecule that has the root mean square average speed before collision, and an ion that is initially at rest, the effective radius of the gas molecule is $(a_g^{'}) \approx 1.8(a_g + a_i)$, which is comparable to that of the molecules and ions, 0.1 nm, but two orders of magnitude below the length scale of λ_i, our escape distance. Thus, we model the ion/molecule collision as one between elastic spheres.

In these collisions, momentum can only be transferred in the direction of the normal force, and the normal force will not necessarily transfer all the momentum to the particle at rest. Conservation of momentum and the law of cosines lead to the expression

$$(p_{if}^{'})^2 = (p_{gf}^{'})^2 + (p_i^{'})^2 - 2p_i^{'}p_{gf}^{'} \cos \varepsilon, \tag{3.32}$$

where p is the momentum of a species, and the subscripts i and g refer to the ion or the gas, while the f subscript refers to the state after collision, and its absence refers to the state immediately before collision. The prime superscript refers to the modified frame of reference. This interaction and the relevant angles, ε and $\varepsilon^{'}$, are shown in Fig. 3.6. Conservation of energy leads to

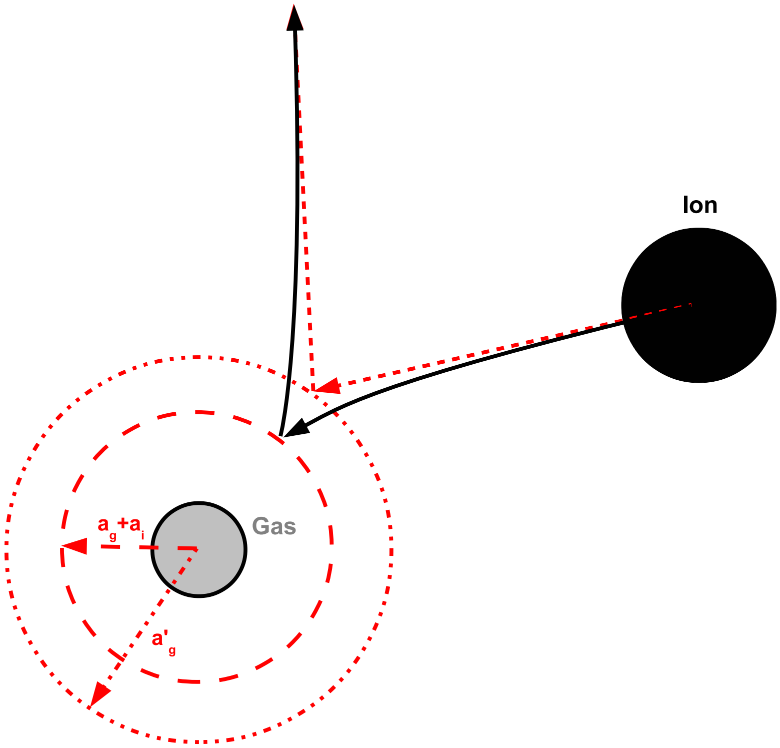

Figure 3.5: Collision between an ion and a gas molecule with an induced dipole moment that leads to an attractive potential. The ion trajectory is shown by the solid line. The equivalent collision trajectory with a larger gas molecule and no potential, shown by the dashed line.

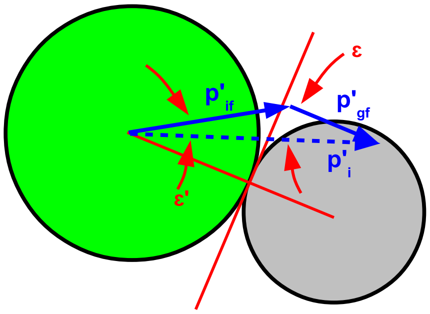

Figure 3.6: The collision between an ion and a gas molecule of different size and mass.

$$(p_i^{'})^2 = (p_{if}^{'})^2 + \frac{M_{ion}}{M_{gas}}(p_{gf}^{'})^2. \tag{3.33}$$

Combining Eqns. (3.32) and (3.33), we get, after some rearrangement,

$$p_{if}^{'} = \left(1 - 4\cos^2\varepsilon \frac{M_{gas}M_{ion}}{(M_{gas}+M_{ion})^2}\right)^{1/2} p_i^{'}, \tag{3.34}$$

which excludes the trivial case where $(p_i^{'})^2 = (p_{if}^{'})^2 = 0$. HF, Natanson (1960), and Fuchs (1963) only considered head-on collisions, for which

$$\lim_{\varepsilon\to 0} p_{if}^{'} = \frac{M_{ion} - M_{gas}}{M_{ion} + M_{gas}} p_i^{'}. \tag{3.35}$$

Translating $p_{if}^{'}$ into our original frame of reference and returning to the final speed yields

$$c_f^2 = (c_f^{'}\cos(\theta^{'} \pm \varepsilon^{'}) - c_g\cos\theta)^2 + (c_f^{'}\sin(\theta^{'} \pm \varepsilon^{'}) + c_g\sin\theta)^2. \tag{3.36}$$

After applying Eq. (3.34) and several trigonometric identities, we find

$$c_f^2 = (A^2+1)c_g^2 + A^2c^2 + 2Ac_g\left[Ac\cos\theta - c\cos(\theta \pm \varepsilon^{'}) - c_g\cos(2\theta \pm \varepsilon^{'})\right] \tag{3.37}$$

where

$$A = \left(1 - 4\cos^2\varepsilon \frac{M_{gas}M_{ion}}{(M_{gas}+M_{ion})^2}\right)^{1/2}. \tag{3.38}$$

Eq. (3.37) describes all possible collisions, and can be used to derive an ensemble average interaction between an ion and a gas molecule as a function of the ion's kinetic energy. The square of the ion velocity is averaged over all possible trajectories, $0 < \theta < 2\pi$, between the ion and the gas molecule to find

$$\left\langle c_f^2(r)\right\rangle_\theta = c_g^2(A^2+1) + c^2A^2. \tag{3.39}$$

Substituting the molecular kinetic energy immediately before collision, Eq. (3.26), and averaging over the Maxwellian distribution of gas molecule velocities yields

$$\left\langle c_f^2(r)\right\rangle_{\theta,c_g} = \frac{2}{M_{gas}}\left(\frac{3k_BT}{2}+\psi(r_1)-\psi(r)\right)(A^2+1)+c^2A^2. \tag{3.40}$$

The ensemble average with respect to ε of A is calculated in the range $\left[\frac{-\pi}{2},\frac{\pi}{2}\right]$ and yields,

$$\left\langle A^2\right\rangle_\varepsilon = \frac{M_{ion}^2+M_{gas}^2}{(M_{ion}+M_{gas})^2}. \tag{3.41}$$

Substituting Eqns. (3.25) and (3.41) into Eq. (3.39) yields

$$\begin{aligned}\left\langle c_f^2(r)\right\rangle_{\theta,c_g,\varepsilon} &= \frac{2}{M_{gas}}\left(\frac{3k_BT}{2}+\psi(r_1)-\psi(r)\right)\left(\frac{M_{ion}^2+M_{gas}^2}{(M_{ion}+M_{gas})^2}+1\right) && (3.42)\\ &+ \frac{2}{M_{ion}}\left(\frac{M_{ion}}{2}c_0^2+\phi(r_0)-\phi(r)\right)\frac{M_{ion}^2+M_{gas}^2}{(M_{ion}+M_{gas})^2}. && (3.43)\end{aligned}$$

If the potential energy change for the gas molecule is small, $|\psi(r_1)-\psi(a_p)| \ll |\frac{3k_BT}{2}|$, this simplifies to

$$\begin{aligned}\left\langle c_f^2(r)\right\rangle_{\theta,c_g,\varepsilon} &= \frac{2}{M_{gas}}\left(\frac{3k_BT}{2}\right)\left(\frac{M_{ion}^2+M_{gas}^2}{(M_{ion}+M_{gas})^2}+1\right)\\ &+ \frac{2}{M_{ion}}\left(\frac{M_{ion}}{2}c_0^2+\phi(r_0)-\phi(r)\right)\frac{M_{ion}^2+M_{gas}^2}{(M_{ion}+M_{gas})^2}. && (3.44)\end{aligned}$$

The deviations produced by this assumption are small, <7%, even for a 1 nm singly-charged particle, and <13% in the unlikely event (López-Yglesias and Flagan, 2013) that the particle is doubly charged. For particles of radii 10 nm and larger the deviation will be ∼0.1% or smaller for a well-modeled distribution.

Ion capture requires

$$\phi(r_0)-\phi(r) \geq \frac{M_{ion}}{2}\left\langle c_f^2(r)\right\rangle_{\theta,c_g,\varepsilon}. \tag{3.45}$$

The equality applies at the three body trapping radius, $r=\delta$; the resulting potential energy can now be used in Eq. (3.20) to calculate the capture cross-section radius b_δ.

The above analysis is applicable for a gas that does not have permanent dipoles, and whose ion species does not consist of free electrons. In this case the uni-molecular force scales as r^{-5}. If, instead of having only induced dipoles, the gas has a permanent dipole moment, the force would act over a considerably longer range, r^{-3}.

Natanson (1960) applied a similar approach, but assumed that the ion and gas molecule both have kinetic energy $3k_BT/2$ at r_0, and the gas molecule experiences no potential. The HF model took a different approach. The energy for the difference of potentials is based on the empirically determined ion recombination distance, H, of Natanson (1959). This method substitutes

$$W = \frac{e^2}{2}\left(\int_{H+\lambda_{ion}}^{H} r^{-2}dr\right) \tag{3.46}$$

for the difference in potential energy in Eq. (3.45). W, here, is the energy associated with two singly and oppositely charged point ions exerting a force on one another. This formulation omits the possibility of multiple charging, image charge, and finite size effects. We shall show later that the omitted interactions are important for the most populous species, the neutral particles, and will introduce a theoretical proportional relation to account for ion properties in the calculation of H.

To consider the influence of the Maxwellian distribution of initial ion speeds, $F(c_0)$, on the probability of ion capture, $f(c_0)$ consider the life of a single ion within the sphere. Because gas molecule collision with an approaching ion are stochastic in nature, some ions that enter the three-body capture sphere will escape. We define a new Cartesian coordinate system, CS2, identical to CS1, defined above, with one exception: the z-axis is antiparallel to the trajectory of the ion at $r = \delta$, rather than at $r = r_0$ as in the case of our model of the two-body collision, or $r_{HF} = \delta + \lambda$ in the HF model. The angle between the ion trajectory at $r = \delta$ and the z-axis is named θ_c as shown in Fig. 3.7b. To calculate the probability of an ion-molecule collision, we estimate the distance that the ion travels through the δ sphere as $\sim 2\delta\cos(\theta)$. By the Beer-Lambert law the ion has a probability of $\exp(-2\delta\cos(\theta)/\lambda_i)$ to pass through the sphere without a collision if θ is greater than the maximum angle, θ_c, that leads to direct intersection with the particle. The polar angle, θ, defines a ring about the z-axis across the surface of the sphere with radius $\delta \sin(\theta)$. All ions of a given speed that travel parallel to the z-axis through the sphere at a given polar angle θ will suffer the same probability of collision. The probability that an ion will enter at any given angle between θ and $\theta + d\theta$ is proportional to the infinitesimal ring cross section at that θ perpendicular to the ion path divided by the total cross sectional area of the δ sphere, $\frac{2\pi(\delta\sin(\theta))(\delta d\theta)(\cos(\theta))}{\pi\delta^2}$ or $2\cos(\theta)\sin(\theta)d\theta$. Integrating from θ_c to $\pi/2$ yields the total probability of the ion avoiding capture once it enters the sphere, i.e.,

$$1 - f(c_0) = \frac{\lambda_i^2}{2\delta^2}\left(1 - \exp(-\frac{2\delta\cos(\theta_c)}{\lambda_i})(1 + \frac{2\delta\cos(\theta_c)}{\lambda_i})\right). \tag{3.47}$$

θ_c can be determined by expressing the exponential in the integrand for the probability as an infinite power series in δ/λ_i. The resulting expression

$$f(c_0) = \sin^2(\theta_c) + 4\delta\cos^3(\theta_c)/(3\lambda_i) + O((\delta/\lambda_i)^2), \tag{3.48}$$

has one term with no dependence on $\frac{\delta}{\lambda_i}$, the unitless constant that characterizes probabilistic capture. This term is the fraction of captured ions that directly strike the aerosol particle. Simple trigonometry yields

$$\sin\theta_c = \frac{b_{HF}(r_a,\delta)}{b_{HF}(\delta,\delta)} = \frac{b_{HF}(r_a,\delta)}{\delta} \tag{3.49}$$

where $b_{HF}(r_a,\delta)$ is the length of a line segment perpendicular to the z-axis, connecting the axis to the ion at δ as shown in Fig. 3.7b. If the ion trajectory at δ is traced straight back to r_{HF}, as shown in Fig. 3.7c, then $\sin\theta_c = \frac{\sin\theta_1}{\sin\theta_2}$ where $\sin\theta_1 = \frac{b_{HF}}{r_0}$ and $\sin\theta_2 = \frac{\delta}{r_0}$. This geometry describes the three body trapping as implemented in HF. The problem with this approach is that the $b_{HF}(r_a,\delta)$ term accounts for the electrostatic lensing only between the δ and r_a spheres, but does not extend the effect to the ion's initial position. HF only use $b_{HF}(r_a,\delta)$ and $b_{HF}(\delta,\delta)$ to calculate $f(c_0)$. At the same time, HF use a different cross section, $b_{HF}(\delta,\delta+\lambda_i)$, that accounts for lensing in the outer region of δ to $\delta + \lambda_i$. However, the ion trajectory curvature makes the directly captured fraction of ions a function of where it is calculated, i.e., at r_0 or δ.

As illustrated in Fig. 3.7d, the present model accounts for the curvature of the ion trajectory along its entire path. The ratio of the modified, two-body cross-section, b_0, to the modified, three-body cross-section, b_δ, as measured at r_0, then becomes

$$\frac{\sin\theta_1}{\sin\theta_2} = \frac{b_0}{b_\delta}. \tag{3.50}$$

This probability correctly accounts for the enhanced cross sections due to electrostatic lensing as previously suggested by Natanson (1960). In any case, three-body trapping need only be taken into account in a model when $\delta > r_a$, as the ion will be caught regardless of whether it collides with a gas molecule when $r_a > \delta$.

The three-body trapping described here is a first order correction to the flux matching theory (Filippov, 1993). Much could still be learned by using a full Monte Carlo simulation with molecular descriptions of the gas, ions, and particles.

Modeling the Charge Distribution

To deduce the statistical macroscopic charge state of an aerosol from the flux coefficients one must solve a system of population balance equations for all sizes of particles that comprise the aerosol. This derivation is given in detail for particles of any size in López-Yglesias and Flagan (2013), so the results will only be briefly described here. Assuming a steady-state charge distribution, the ratio of the ion concentration at charge state k, N_k, and that at the next lowest charge state is

$$\frac{N_k}{N_{k-1}} = \frac{\beta_{k-1,1} n_1}{\beta_{k,-1} n_{-1}}, \tag{3.51}$$

from which it follows that

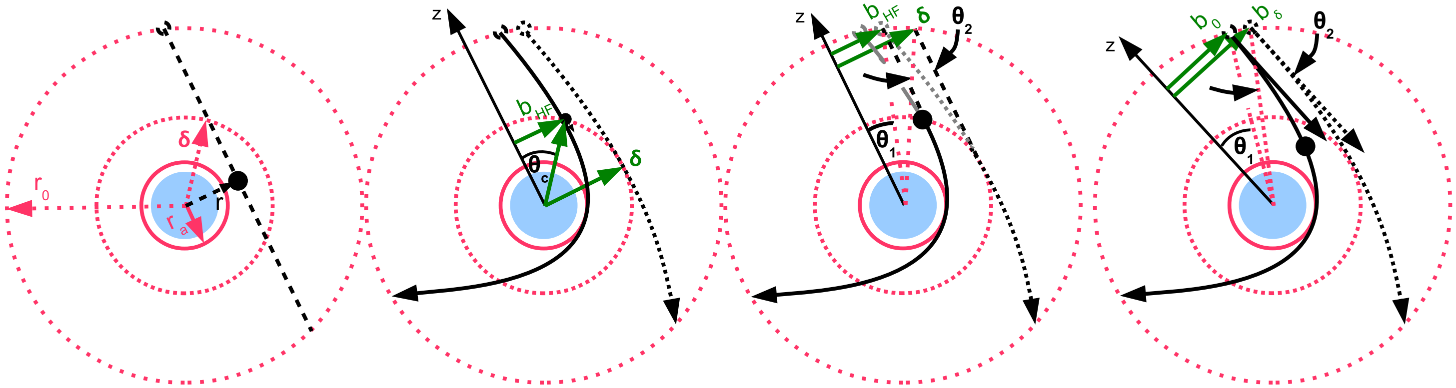

(a) The radius, r, pictured here, is the distance of closest approach. If $r < r_a$, then the ion is definitely captured. If $r_a < r < \delta$, then the ion has a chance of capture, dependent on the path length in the δ sphere. If $r > \delta$ there is no chance of ion capture.

(b) Three body trapping as implemented in HF. The radius of the direct capture cross-section, b_{HF}, is the perpendicular distance between the z-axis and the ion trajectory at δ. This ion trajectory is tangent to the r_a sphere. Electrostatic lensing is only considered between radius δ and r_a, so the radius of the probable capture cross-section has no enhancement and is simply δ.

(c) Outside of the δ sphere the ion is assumed to travel in a straight path, so we can trace back the trajectory to radius r_0 and deduce that $\sin\theta_c = \frac{\sin\theta_1}{\sin\theta_2}$.

(d) The ion trajectory is curved all the way to the beginning of its flight path, so electrostatic lensing takes place throughout the region between radius r_0 and r_a, leading to a capture radius b_0, and $\frac{b_0}{b_\delta} > \frac{b_{HF}}{\delta}$.

Figure 3.7: Three body capture and the calculation of the critical angles between definite and possible capture, θ_c, θ_1, and θ_2.

$$\frac{N_k}{N_0} = \prod_{j=1}^{k} \frac{N_j}{N_{j-1}}, \tag{3.52}$$

may be used to obtain the ratio between the concentration of particles in charge state k and those with charge state 0. Summing over all charge states, one finds

$$\frac{N_T}{N_0} = \sum_{j=-h}^{y} \frac{N_j}{N_0}. \tag{3.53}$$

In practice, the calculations are performed only over a finite range of charge states, $-k \leq j \leq y$. The charge distribution thus becomes

$$\frac{N_k}{N_T} = \frac{N_k/N_0}{N_T/N_0}. \tag{3.54}$$

The validity of the steady state assumption under different charging times and aerosol loadings is examined in detail in López-Yglesias and Flagan (2013).

Although the present work treats the negative and positive ions in this model as two singular species, this is a simplification. In reality, the ion masses and mobility follow a distribution, which depends upon the composition of the environment, and which will have an effect upon the resultant charge distribution (Lee et al., 2005).

Results

Hoppel and Frick (1986) previously modeled the charging of conductive particles up to 500 nm in radius. The present model relaxes several approximations in the earlier work, and treats particles of any dielectric constant. Furthermore, the particle charge is allowed to induce an image in the ion cluster. To allow direct examination of the influence of the relaxed approximations and broader range of aerosol materials, we employ the same ion properties, shown in Table 3.1, while examining a range of dielectric constants.

Figure 3.8 shows the variation in the calculated flux coefficients as a function of particle size for a wide range of charge states. The predictions for conductive

Table 3.1: Initial Parameters

Symbol	Value
T	298.15 K
P	101325 Pa
μ_{+ion}	$1.2 \cdot 10^{-4}$ m^{2}V^{-1}s^{-1}
μ_{-ion}	$1.35 \cdot 10^{-4}$ m^{2}V^{-1}s^{-1}
M_{+ion}	150 Da
M_{-ion}	90 Da
M_{gas}	28.97 Da
η	$18.27 \cdot 10^{-6}$ Pa·s

particles (solid lines) can be directly compared to those of HF (dotted lines). The two models agree well for large particles, though there are subtle differences that arise from consideration of the entire velocity distribution, and from the revised three-body trapping model which is applied to all attractive interactions.

The induced-charge effect diminishes with decreasing size, causing the interactions to switch from attractive to repulsive at the sizes indicated by circles in Fig. 3.8. These points correspond to the particle size at which there exists a cutoff speed below which the ion cannot reach the particle. Below this transition point the present model diverges from that of HF, since, rather than averaging over the speed distribution, HF use a single equivalent speed. This leads to rapid decrease and sharp cut off in their flux coefficients because the single speed used is no longer able to overcome the repulsive force. This difference becomes extremely important for calculating multiple charging events in a unipolar environment.

Another important difference between the two models is the consideration of finite ion size. HF assume that the ions are 0-D points, which implies that their flux coefficients can decrease to 0 with decreasing particle size. We may estimate the particle size below which finite ion size affects the flux coefficients as that for which the capture radius is the sum of both bodies' radii when the ion is traveling at speed $\bar{c} + \sigma$, where σ is the standard deviation of the Maxwellian distribution of ion speeds. Above the transition the models agree well. Below this transition point the present model approaches its asymptote, while the HF estimation continues to 0.

The situation is more complex for flux coefficients of oppositely charged ions and particles. Although there are transitions below which the appearance of the model changes, there is no smoking gun. The effects discussed in the beginning of this section are no longer subtle at low particle charge. The closest we can come to a true transition point may be when three-body trapping replaces two-body trapping in the HF model, shown as open or blue squares in Fig. 3.8. Here the difference between the two and three-body models considered becomes very pronounced. The two to three body transition point for our model is denoted by a closed, or red, square in Fig. 3.8. We may estimate this point by searching for the largest particle size where the resultant, unaveraged flux coefficient is larger in three-body trapping than in two-body trapping, while the ion is traveling at speed $\bar{c}+\sigma$. Below the transition point of the HF model, their calculated flux coefficients are greater than those of the present model due to the revised energy calculation and geometric effects discussed in the three-body trapping section of this paper. The two models would differ even more wildly at the smallest particle sizes if not for the fact that our model also undergoes a finite size transition, increasing our flux coefficients at these low sizes.

In addition to re-examining flux coefficients for conductive particles, we have also explored the difference in flux coefficients due to a lower dielectric constant. In particular, we examine aerosol particles with a dielectric constant of 2.6, corresponding to polystyrene, which is often used for calibrating DMAs. As expected, the image force for dielectric particles is weaker than for conductive ones, markedly accelerating the decrease of the flux coefficient in like-charged and ion-to-neutral-particle interactions. Ion-to-neutral-particle interactions regain the same flux coefficients as the conductive aerosol at small particle size due to the finite size transition. Oppositely charged particles are only affected in the transition between the dominance of the image charge force and source charge force.

Figure 3.9 shows the steady-state fractional population of the aerosol as calculated from the flux coefficients above. The corrections to HF at the high end of the model have previously been discussed in López-Yglesias and Flagan (2013). In the present

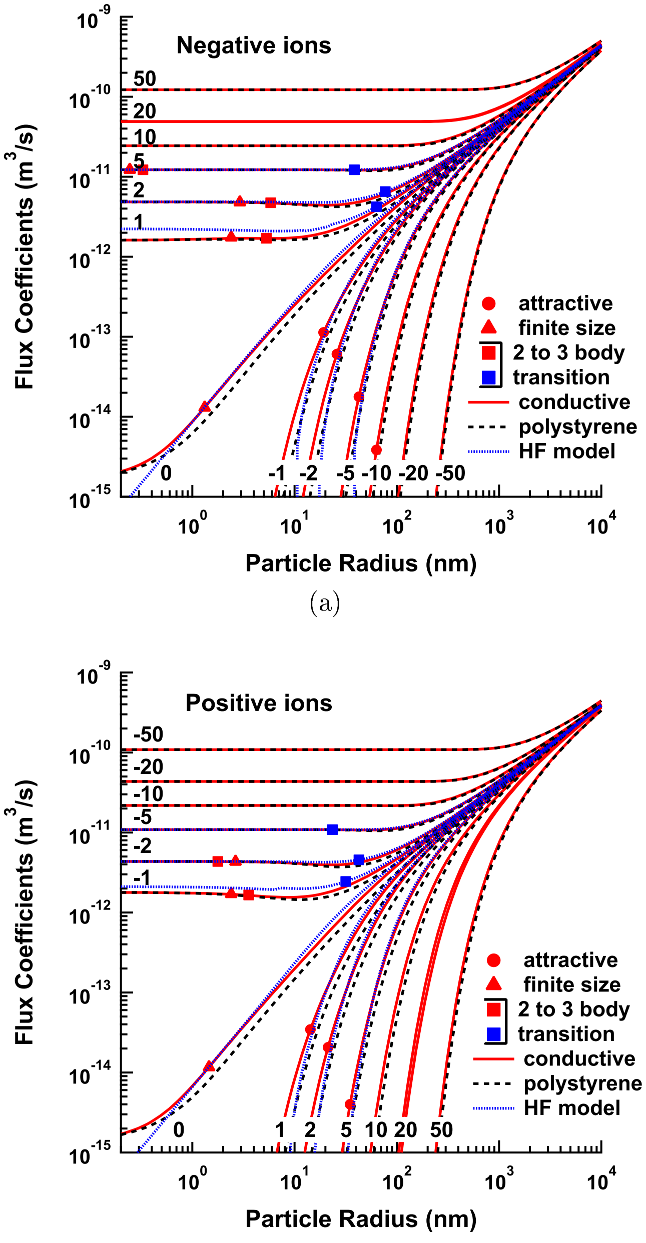

(a)

(b)

Figure 3.8: Flux coefficients for negative, (a), and positive, (b), ions to aerosol particles of various charge states.

model, the charged fraction approaches an asymptote at small sizes. The curvature results from the finite size effect in the ion-to-neutral-particle flux coefficients. For doubly charged particles of opposite polarity, HF predicts that the charging probabilities for positive and negative particles cross as size decreases, albeit at a very low charging probability. This crossing is eliminated in the present model by considering the full Maxwellian speed distribution. The Wiedensohler (1988) approximation is also included for the sake of comparison. Its parameters are based on the earlier works of Wiedensohler et al. (1986), Hussin et al. (1983), and HF. It is an approximation of the HF model valid for particles of $0.5 \leq a_p \leq 500$ nm radii that are neutral or have $\pm 1e$ of charge, and for particles of $10 \leq a_p \leq 500$ nm radii that have $\pm 2e$ of charge. For higher charge states Wiedensohler applied the analytical solution from Gunn and Woessner (1956), which is only valid for particles with $a_p > 25$ nm because it is based upon an equilibrium Boltzmann distribution. Furthermore, as clearly discussed by Fuchs (1963) and Mayya (1993), the equilibrium model is not applicable to ambient temperature aerosol charging because the “reverse reaction” to charge attachment, charged species desorption, is energetically unfavorable. Nonetheless, within the working regime of Gunn’s model, our model agrees well. However, it varies significantly from the HF charge distribution above 400 nm in radius and below 3 nm for particles with $\pm 1e$ or $\pm 2e$ of charge.

We also explored the effects of the image charge induced on the ion by the particle, for a water cluster with a dielectric constant of 80.1. The inclusion of the ion image charge raised the value of the flux coefficients for oppositely charged particles and ions by a maximum of 10% for singly charged particles below 2 nm in radius, leading to a similar decrease in the fraction of charged particles in the steady state distribution in this size range. Above this size and/or particle charge the effects are $< 1\%$ for oppositely charged species. The flux coefficients of similarly charged particles and ions increase by up to seven orders of magnitude in the nanometer size regime, but the ratio of these flux coefficients to those for the ion-to-neutral interactions, the dominant source of charged particles in this size regime, is still insignificant to the steady state charge distribution.

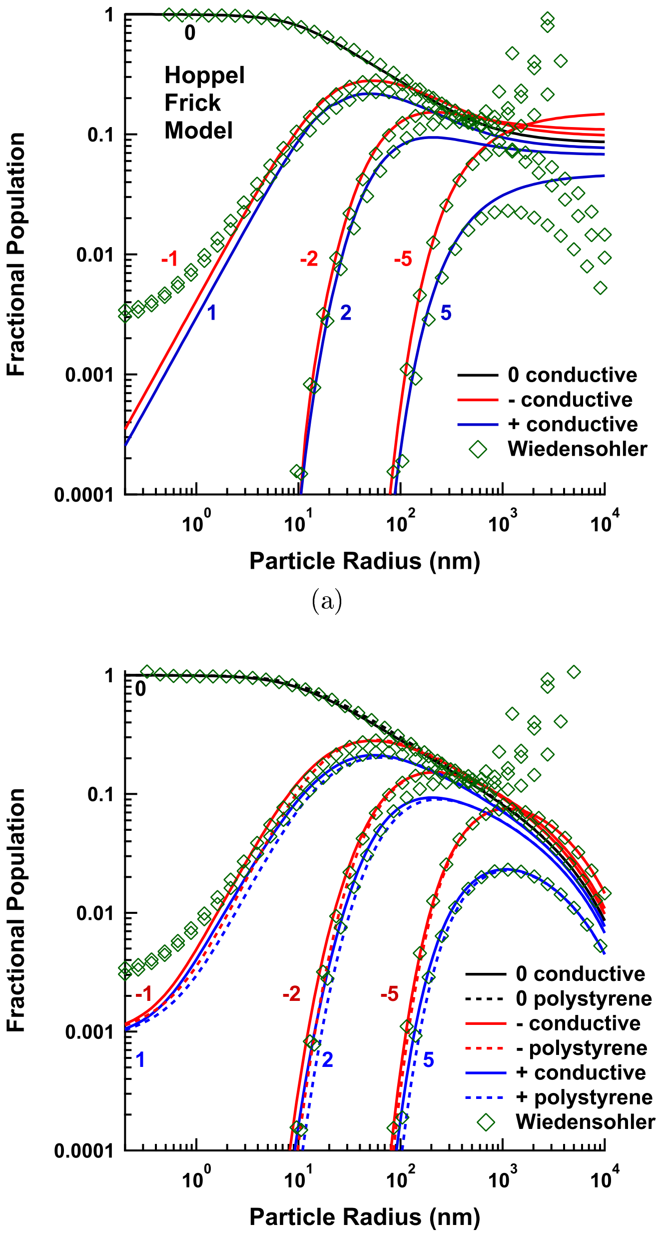

Figure 3.9: Steady state charge distributions for the HF model, (a), and the present model, (b).

Previous studies of aerosol charging only consider normal laboratory conditions, but aerosol measurements are made in many other environments. In particular, DMAs are extensively used to measure size distributions from airborne platforms. Therefore, we also consider the effect of a change in pressure and temperature, P=4480 Pa and T=218.15 K. This simulates the atmospheric conditions at an altitude of 20 km, as an upper bound to present DMA measurements. For this substudy, we consider only the conductive particles. The results are shown in Figs. 3.10 and 3.11. The flux coefficients between doubly and, especially, singly charged particles and ions of opposite charge are significantly reduced from the coefficients at sea level. Moreover, the flux coefficients for attractive interactions at high charge levels exhibit a pronounced minimum in the transition between the fine particle asymptote and the continuum diffusive regime. These effects are due to the greatly increased mobility and mean free path at high altitudes. The ions now begin their relevant lifespans further away, reducing the effect of the attractive force, especially at small particle charge. Because of this, the effects of image charge on a water ion as opposed to an "air" ion are significantly more pronounced than at ground level, leading to deviations of a factor of ~ 2 in both the flux coefficients and the steady state charge distribution for small particle sizes. These reduced flux coefficients lead to a significant increase in the singly charged fraction of the aerosol population at nanometer size. Thus, use of sea-level charging probabilities to invert airborne DMA measurements may lead to significant errors in the estimated particle size distribution depending on the altitude.

Conclusions

We investigated several corrections and extensions to the aerosol charging model of Hoppel and Frick (1986). The description of the potential between an ion and an aerosol particle was broadened to include dielectric bodies, and to allow for image charges to be induced on the ion. The effective radius of the ion, a_i, was derived, and a fixed starting point for the trajectory of the ion in its interactions with an aerosol particle, based solely on a_p, a_i, and λ_i, r_0, was formulated for use. The resulting flux

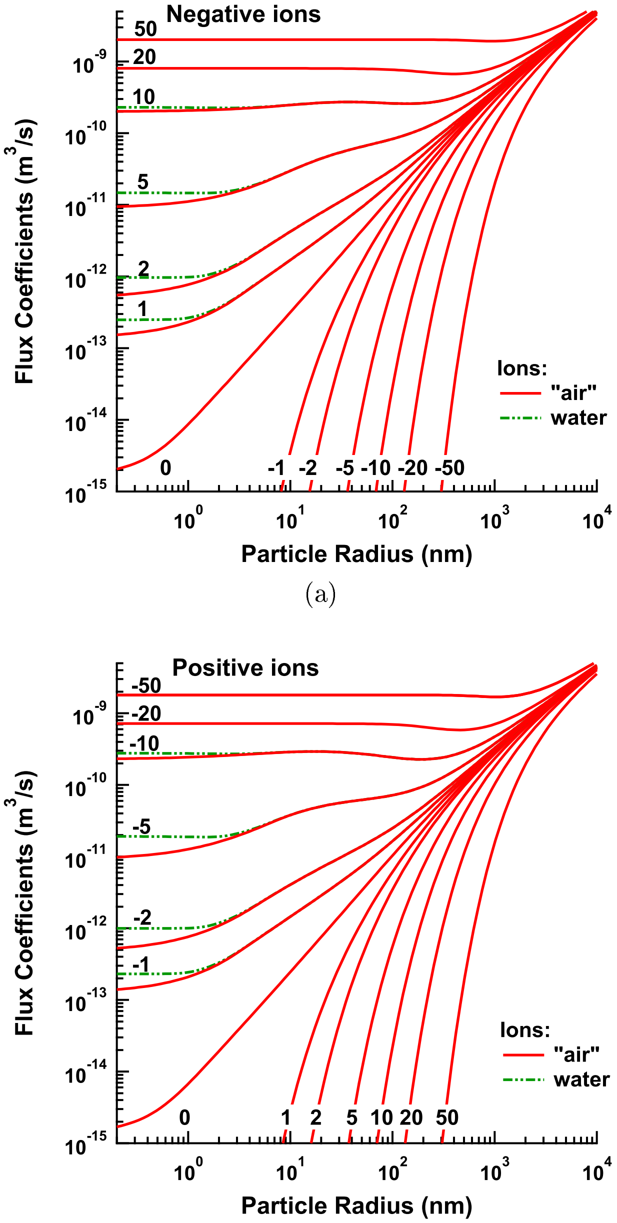

(a)

(b)

Figure 3.10: Flux coefficients for negative, (a), and positive, (b), ions to aerosol particles of various charge states at P=4480 Pa and T=218.15 K, conditions at an altitude of $\sim$ 20 km.

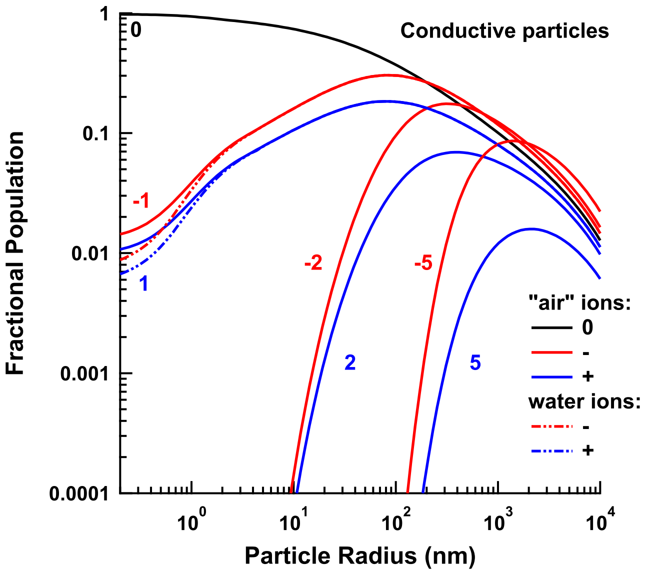

Figure 3.11: The resultant steady state charge distribution using the present model at an altitude of ∼ 20 km.

coefficients were then averaged over the Maxwellian velocity distribution of the ion at ambient conditions to obtain the ensemble average. The mechanism for three-body trapping was also revisited and improved upon. The calculation of the average energy lost in an ion-gas molecule collision within a particle's potential well was re-derived from kinetic theory, and the probability of ion capture was also revised to account more fully for the curvature of the ion's flight. In light of these changes, the flux coefficients and steady-state distributions of our model were compared to those from HF and the Wiedensohler approximation.

Using the same ionic and ambient parameters as HF, we found several points where the present model diverged significantly from the flux coefficients in HF. Consideration of the Maxwell-Boltzmann distribution of ion speeds leads to significant deviations from the HF ion flux coefficients for like-charged aerosol-ion interaction at 40 nm radii particle and below. Transitions for oppositely charged aerosol-ion interactions occur at radii $<$85 nm due to a combination of three-body trapping and the ion's finite size. Ion-to-neutral-particle interactions begin to deviate at low nanometer sizes due entirely to finite-size effects. These changes in the flux coefficients are reflected in quantitative and qualitative changes in the steady-state charge distribution. The most significant of these changes is a leveling off of the singly charged aerosol population at small radii due to finite size effects.

Varying parameters within the new model leads to further deviations from the original theory. Dielectric particles, often used to calibrate DMAs, have a significantly reduced image charge. This manifests itself as a reduced population of charged particles at all particle sizes due primarily to the suppression of the flux coefficients for like-charged particles and ions, and the reduced probability of ion capture by neutral particles. The latter effect reduces to ballistic ion capture in the absence of image charge. The population of singly-charged aerosol particles can decrease by $\sim \frac{2}{3}$.

We also examined the effect of atmospheric conditions on particle charging. At altitudes near the tropopause, the pressure and temperature both drop, increasing the ion mobility and mean free path, and decreasing the gas viscosity. This suppresses ion-particle recombination at small particle charge, increasing the fraction of charged aerosol at nanometric size by a factor of ~ 3 compared to sea level conditions.

Finally, for the bipolar charging that was the focus of this paper, the image charge on the ion has a small effect, at most 10%, on the steady state aerosol charge distribution at ground level, but causes deviations of up to a factor of 2 at high altitudes for nanometer sized particles. This ion image-charge potential may also be important in long time exposure to a unipolar environment, particularly in the nanometer size range.

The corrections and additions included in this study cause a wide range of changes to the aerosol charge distribution, especially for nanometer particles. As differential mobility analyzer studies continue to push the lower limit of observed particles into this range we feel that the effects presented here may prove useful for enhancing the accuracy of data in this size regime. The previously reported deviations at large particle size also lead to substantial overestimates of the particle concentrations above about 200 nm radius. This may significantly bias DMA-based estimates of the mass concentration of fine particles. We have provided curve-fits to the flux coefficients and charging probabilities in the manner of Wiedensohler, but note that these fits, and all of the calculations on which they are based, employ the ion properties that were used in the earlier Hoppel and Frick (1986) model. The ion properties, and this dependence on atmospheric parameters, especially relative humidity, needs to be reexamined, but this is beyond the scope of the present work.

Acknowledgments

We thank Lindsay Yee for her time spent editing and discussing this manuscript. We would also like to thank the NASA Astrobiology Institute through the NAI Titan team managed at JPL under NASA Contract NAS7-03001 for the funding of this project, the Ayrshire Foundation for their support in making computing resources available, and Aerosol Science and Technology for their permission to reproduce this article, first published within their journal.

Bibliography

[1] Amadon, A.S. and Marlowe, W.H. (1991a). Cluster-collision frequency. I. The long-range intercluster potential. *Phys. Rev. A* **43**:5483-5492

[2] Amadon, A.S. and Marlowe, W.H. (1991b). Cluster-collision frequency. II. Estimation of the collision rate. *Phys. Rev. A* **43**:5493-5499

[3] Filippov, A.V. (1993). CHARGING OF AEROSOL IN THE TRANSITION REGIME. *J. Aerosol Sci.* **24**(4):423-436.

[4] Fuchs, N.A. (1947). On the magnitude of electrical charges carried by the particles of atmospheric aerocolloids. *Izvestiya Acad. Sci. USSR Ser. Geogr. Geophys.* **1l**:341-348. In Russian with English summary.

[5] Fuchs, N.A. (1963). On the Stationary Charge Distribution on Aerosol Particles in a Bipolar Ionic Environment. *Geofis. Pura Appl.* **56**:185-192.

[6] Gopalakrishnan, R. and Hogan, C.J. (2012). Coulomb-influenced collisions in aerosols and dusty plasmas. *Phys. Rev. E* **85**,026410

[7] Gunn, R. and Woessner, R.H. (1956). Measurements of the Systematic Electrification of Aerosols. *J. Colloid. Sci.* **11**:254-259.

[8] Hoppel, W.A. and Frick, G.M. (1986). Ion-Aerosol Attachment Coefficients and the Steady-State Charge Distribution on Aerosols in a Bipolar Ion Environment. *Aerosol Sci. Technol.* **5**:1-21.

[9] Hussin, A., Scheibel, H., Becker, K., Porstendorfer, J. (1983). Bipolar Diffu-

sion Charging of Aerosol Particles-1. Experimental Results within the Diameter Range 4-30 nm. *J. Aerosol Sci.* **14**:671-677.

[10] Keefe, D., Nolan, P.J., Scott, J.A. (1968). Influence of Coulomb and Image Forces in Combination of Aerosol. *Proc. R. Irish. Acad.* **60A**:27-44.

[11] Kirkby, J. et al. (2011). Role of sulphuric acid, ammonia and galactic cosmic rays in atmospheric aerosol nucleation. *Nature* **476**:429–433

[12] Khrapac, S. and Morfill, G. (2009). Basic Processes in Complex (Dusty) Plasmas: Charging, Interactions, and Ion Drag Force. *Contrib. Plasma Phys.* 49, No. 3, 148 – 168.

[13] Lee, H.M., Kim C.S., Shimada, M., Okuyama, K. (2005) Effects of Mobility Changes and Distribution of Bipolar Ions on Aerosol Nanoparticle Diffusion Charging. *J. Chem. Eng. Japan* **38**:486-496.

[14] Loeb, L. (1939). *Fundamental Processes of Electrical Discharge in Gases.* Wiley, New York, pp.112-120.

[15] López-Yglesias, X. and Flagan, R. (2013) Population Balances of Micron-Sized Aerosols in a Bipolar Ion Environment. *Aerosol Sci. Technol.*, 47(6): 681–687.

[16] Lushnikov, A.A. and Kulmala, M. (2004). Charging of aerosol particles in the near free-molecule regime. *Eur. Phys. J. D* **29**:345-355.

[17] Mayya, Y.S. (1994). On the "Boltzmann Law" in Bipolar Charging. *J. Aerosol Sci.* **25**:617-621.

[18] Nadykto, A. and Yu, F. (2003). Uptake of neutral polar vapor molecules by charged clusters/particles: Enhancement due to dipole-charge interaction. *J. Geophys. Research* **108**:D23:4717.

[19] Natanson, G.L. (1959) The theory of volume recombination of ions. *Soviet Physics Technical Physics* **4**:1263-1269.

[20] Natanson, G.L. (1960). On the Theory of Charging of Amicroscopic Aerosol Particles as a Result of the Capture of Gas Ions. *Soviet Physics Technical Physics* **5**:538-551.

[21] Neumann, C. (1883). *Hydrodynamischie Untersuchen nebst einem Anhang uber die Probleme der Elecktrostatik und der magnetischen Induktion.* Teubner, Leipzig, pp. 279-282.

[22] Norris, W.T. (1995). Charge images in a dielectric sphere. *IEE Proc.-Sci. Meas. Technol.* **142**:2:142-150

[23] Premnath, V., Oberreit, D., and Hogan Jr., C.J. (2011). *Aerosol Sci. Technol.*, 45:712–726.

[24] Seinfeld, J. and Pandis, S. (1998). *Atmospheric Chemistry and Physics.* Wiley, New York, pp. 454-459.

[25] Tammet, H. (1995). Size and Mobility of Nanometer Particles, Clusters and Ions. *J. of Aerosol Sci.* **26**(3):459-475.

[26] Tammet, H. and Kulmala, M. (2005). Simulation tool for atmospheric aerosol nucleation bursts. *J. Aerosol Sci.* **36**:173-196.

[27] Wiedensohler, A., Liitkemeier, E., Feldpausch, M., Helsper, C. (1986). Investigation of the bipolar charge distribution at various gas conditions. *J. Aerosol Sci.* **17**:413-416.

[28] Wiedensohler, A. (1988). An Approximation of the Bipolar Charge Distribution for Particles in the Submicron Size Range. *J. Aerosol Sci.* **19**:387-389.

[29] Yu, F. and Turco, R. (1998). The formation and evolution of aerosols in stratospheric aircraft plumes: Numerical simulations and comparisons with observations. *J. Geophys. Research.* **103**:D20:25,915-25,934.

Chapter 4

The enhancement in the uptake of neutral vapor to aerosol particles in the upper and lower Titan atmosphere due to electrostatic and finite size effects

Xerxes López-Yglesias and Richard Flagan

A rigorous model is presented to calculate the flux for the case of all particle sizes from 0.2 nm to 10 μm using several different vapors: HCN, C_6H_2, CH_4, H_2O and C_6N_2 and particle compositions: HCN, C_6H_2, CH_4, and a "bare" aerosol. It is found that at the smallest sizes under consideration, 0.2 nm radius, the model yields an order of magnitude or more enhancement using a neutral cluster or particle. For polar species the enhancement can cover the entire size range under consideration, and, the addition of charge, increases uptake by another order of magnitude at the smallest particle sizes. Progressively higher charge states further increase the flux, but they may be unimportant on physical grounds. Their frequency will depend not only upon the atmospheric charge distribution, but also on the state of the particle itself. In this case, a liquid particle's size and surface tension is used to estimate the maximum number of charges it can support. Polar species and C_6N_2 are able to support higher charge states at smaller sizes due to their high surface tension. The vapor species and particle compositions under consideration here are picked specifically for their

relevance to Titan microphysical models.

Introduction

Much effort has been directed to the study and understanding of the Titan atmosphere. Lavvas has examined aerosol formation and growth in both the upper and lower Titan atmosphere[7, 8, 9, 6, 5]. Still, there are many aspects of aerosol growth and formation that remain poorly understood. The model employed by Lavvas et al. [5] does not take into account attractive forces between the particle/cluster and vapor species due to charge-dipole and dipole-dipole interactions[15]. It also fails to take into account the finite size of the vapor molecule, an important consideration for small particle sizes. We will show that this leads to an underestimation of the vapor flux to the particle, and, thus, the particle's growth rate.

To narrow the scope of vapor species and ambient conditions under consideration, only the upper atmosphere, from 900-500 km, and the lower atmosphere, $<$100 km, are considered. Within these two regimes appropriate heights and vapor species are based upon Lavvas et al. [6] and Lavvas et al. [5] respectively. In the upper atmosphere, the species closest to supersaturation and condensation are H_2O and C_6N_2. The flux increase for a polymerizing radical, CN, proposed in Lavvas et al. [7] is also considered here, as aerosol particles are thought to be largely formed through polymerization at these altitudes. For all of these species only the flux onto a "bare" aerosol particle is considered. In the lower atmosphere, HCN, C_6H_2, and CH_4 will be the species of interest. These species are allowed to condense onto a bare particle or onto one already coated with one of the afore-mentioned condensing vapors.

Model

The model used to pursue this work is based on Lopez-Yglesias and Flagan [11, 12]. It considers a cluster or particle of a given size, charge, and composition suspended in a bath gas that can neither adhere to the particle nor have electrostatic interactions with the particle. The bath also contains a dilute vapor. If a vapor molecule collides with the particle or is trapped in the potential well, the molecule is assumed to "stick" to the particle. The flux of the vapor to the particle is calculated by dividing the space around the particle into two regimes based on the Knudsen number, Kn= λ/a, where λ is the mean free path of the vapor in the background gas, and a is the particle radius. The particle radius and vapor mean free path are the length scales that define the particle-vapor interaction. In the limit that Kn goes to 0 or ∞ then the vapor flux can be described through diffusion or free molecular approaches respectively, but this is not the case in the transition regime. Here, an approximation is made. A sphere is defined with radius r_0 where the diffusive and free molecular fluxes are matched at a distance of order the mean free path away from the particle surface. This approach to accounting for the transition from molecular to continuum transport regimes is known as a limiting sphere model[13]. This model yields a rate coefficient,

$$\beta(c_0) = \frac{I(c_0)}{n_\infty} = \frac{\pi c_0 b_0^2(c_0)\exp(\frac{-\phi(r_0)}{k_B T})}{1 + \pi c_0 b_0^2(c_0)\exp(\frac{-\phi(r_0)}{k_B T})(4\pi D)^{-1}\int_{r_0}^{\infty} r^{-2}\exp(\frac{\phi(r)}{k_B T})dr},$$

that determines the current to the particle if the vapor concentration at infinity is known. Here I is the vapor species' molecular current to the particle, c_0 is the speed of the vapor molecule, n_∞ is the concentration of the vapor infinitely far from the particle, b_0 is the capture cross section for the particle in the kinetic regime, ϕ is the potential energy between the vapor molecule and the particle, D is the diffusivity of the vapor in the background gas, k_B is the Boltzmann constant, and T is the temperature. This expression must be integrated over the Maxwellian distribution of velocities, c_0, to determine the average rate coefficient, $<\beta(b,\phi)>$. The enhancement is simply $\frac{<\beta(b,\phi)>}{<\beta(a,0)>}$.

The implementation of a limiting sphere model in this work varies from that described in Lopez-Yglesias and Flagan [11] in two ways. The previous work examined the flux of ions to both charged and uncharged particles. Here we examine the flux of a neutral vapor species to both charged and uncharged particles. Because of this, the vapor diffusivity rather than the ion mobility is used to determine both the mean free path and an approximate physical radius for the vapor, and, thereby, to constrain the minimum cross-section for collision. In addition, the potential has been changed to that between a vapor phase species capable of supporting a dipole moment and a charged or neutral particle of a given static dielectric constant,

$$\phi(r) = -\left(\frac{1}{4\pi\epsilon_0\chi_g r^2}\right)\left(m|k|e + \frac{\alpha k^2 e^2}{8\pi\epsilon_0\chi_g r^2} + \frac{m^2\gamma\xi^{\frac{3}{2}}}{2r}\int_0^1 d\alpha\frac{4-3\sin^2\phi+2\alpha\xi}{(1-\alpha\xi)^4}\alpha^{\frac{1-\gamma}{2}}\right),$$

where r is the radial distance from the center of the particle to the vapor phase species, k is the number of electron charges on the particle, e is the Coulomb charge on a single electron, m is the scalar value of the dipole moment on the condensing vapor, ϵ_0 is the vacuum permittivity, α is the polarizability of the vapor species, χ is the static dielectric constant, whether of the particle or the gas is determined by the subscripts p and g, $\xi = (a/r)^2$, $\gamma = \frac{\chi_p - \chi_g}{\chi_p + \chi_g}$, and ϕ is the angle between the dipole and a line extending from the center of the particle. The first term in the expression is the potential between a permanent, ideal dipole and a charged particle. The second term is the potential between a charged particle and the ideal dipole it induces. The third term is the potential between a permanent, ideal dipole and the image it induces on a particle[14]. There is no potential term between a non-polar species and an uncharged particle. Note that the full potential does not include the secondary or higher order induced images. This means that if the vapor species is polarizable, but has no permanent dipole moment, this potential will take into account the force between the induced dipole moment and the charged particle, but it will not take into account the image that this new dipole induces on the sphere. Thus, the attraction between a non-polar species and a charged particle will be completely independent of the composition of the charged particle. Neglecting these higher order terms is a valid assumption since each successive term has a force with significantly shorter range. The dipole-charge interaction described for non-polar species scales as r^{-5}. The higher order dipole-dipole interaction term omitted here would scale as r^{-11}. Thus, the higher order terms will be of negligible importance at r_0.

In the current model there are only four parameters needed to describe the particle: charge, size, surface tension, σ, if the particle is in the liquid phase, and static dielectric constant. The size and charge are variables explored within the model. The surface tension determines the maximum charge a liquid phase particle can support. The particle becomes unstable to physical perturbations at high charge as the electrical forces on the particle exceed the restoring force of its surface tension. The Rayleigh stability criterion,

$$q^2 < 64\pi^2 a^3 \epsilon_0 \chi_g \sigma, \tag{4.1}$$

places an upper bound on the number of charges, q, that a liquid particle of a given size can have[3]. This criterion is based on the stability of a spherical droplet with a uniform surface-charge upon deformation. Of course, since this criterion assumes that charge is continuous and spread along the surface of the particle, in the limit of a few charges the theory will break down, but it still provides a useful guideline. Only the particles in the lower atmosphere that are coated with a condensate are assumed to be in the liquid phase. The calculation of the dielectric constants of the particles can also be divided into those that are in the liquid phase, and those that are not. Liquid particles are assumed to be composed of just one condensed vapor species for the purpose of calculating the dielectric constant. The dielectric constants for the liquid particle compositions considered in this work are calculated from a polynomial fit, $\chi_p = a + bT + cT^2$, where the constants are taken from the CRC handbook, when the temperature on Titan is in range[10]. When it is not within the range of the empirical fit, the lowest valid temperature value in the range is used to compute the dielectric constant. For a bare tholin-like particle, the static dielectric constant value is $\chi_p = 4.71$, which is estimated from the index of refraction at the longest wavelength, 920 μm, measured by Khare and Sagan (1984)[4].

Modeling of the vapor phase species also requires four parameters: diffusivity, polarizability, dipole moment, and mass. The diffusivity of the vapor species considered in this work is based on the experimental data available, and then adjusted for

Table 4.1: Physical properties of the species under consideration.

	HCN	C_2H_6	CH_4	H_2O	C_6N_2	CN
$\alpha \cdot 10^{24}$ (cm^3)	2.59[10]	4.47[10]	2.59[10]	1.45[10]	10.182[1]	
$D \cdot 10^5$ (m^2/s)[16]	1.29 273 K, 1atm	1.48 298 K, 1 atm	1.96 273 K, 1 atm	2.32 273 K, 1 atm	ethane 1.48 298 K, 1 atm	
m (Debye)	2.984[10]	0[10]	0[10]	1.854[10]	0[1]	1.47[2]
σ (mN/m)	76 H_2O at 273 K[10]	28 C_2H_6 at 113 K[16]	18 CH_4 at 93 K[16]	76 H_2O at 273 K[10]	82.2[1]	
χ[10]	a=1.5996 b=$2.7434 \cdot 10^{-3}$ c=-$2.2086 \cdot 10^{-5}$ 91-184 K	a=2.0815 b=-$5.1493 \cdot 10^{-5}$ c=-$4.8148 \cdot 10^{-6}$ 95-295 K	a=$3.7331 \cdot 10^3$ b=-$2.318 \cdot 10$ c=$3.6963 \cdot 10^{-1}$ 258-299 K			

temperature and pressure using

$$D = D_0 \left(\frac{T}{T_0}\right)^{\frac{3}{2}} \left(\frac{P_0}{P}\right), \tag{4.2}$$

where D is diffusivity of the vapor species in the bath gas, here N_2, T is the temperature, and P is the pressure. The subscript zero denotes that these are the known experimental values. This relation uses the temperature and pressure dependencies of Chapman-Enskog theory, but ignores the temperature dependence of the collision integral as these values are normally of order unity[10]. The polarizability and dipole moment of the vapor phase species are assumed to be temperature independent.

Finally, there is one parameter associated with the bath gas, its dielectric constant. The dielectric constant of the gas, N_2, is calculated from

$$\chi_g = \frac{1 + \frac{8\pi\alpha P}{3k_BT}}{1 - \frac{4\pi\alpha P}{3k_BT}}. \tag{4.3}$$

Results and Discussion

The results for the lower atmosphere showed insensitivity to the particle dielectric constant. This must be the case for the non-polar species because of the potential used, but HCN also showed very little variability in the enhancement, 2% maximum.

As such, the flux enhancement depends only on the vapor species, the atmospheric height, and the particle size and charge, but does not depend on the particle composition.

The flux of the non-polar species varied little between species and/or heights and is well-represented by Fig. 4.1. The model used in Lavvas et al. (2011) does not take into account the finite molecular size of the vapor species. This means that even the neutral trace, whose only enhancement with a non-polar vapor species is due to finite size effects, shows flux enhancement extending to 10 nm in radius, with an enhancement factor of ∼10 at 0.2nm. Further enhancement due to electrostatic potential is relatively minor for this case; a single charge on the particle increases the flux by a factor of ∼3 over the neutral case at the smallest sizes, dropping to unity gain by ∼1 nm. Higher charge states are irrelevant in the case of liquid phase particles due to the low surface tension of the nonpolar species. The cutoffs are shown in Fig. 4.1 with blue dots.

The flux of the polar species, HCN, is enhanced by one to two orders of magnitude due to both electrostatic interactions and the finite size of the molecule at the smallest sizes considered here. The enhancement persists up to a particle radius of 1 μm at 75 km, and up to 200 nm at 30 km. A single charge on the particle raises the flux another order of magnitude at the smallest sizes. Further addition of charges contributes decreasing enhancements to the flux, a factor of two for the second charge and dropping. Enhancement due to charge effects persists until the particles are ∼20 nm in radius. In the case of liquid droplets, the stronger surface tension for the polar condensate means that multiply charged particles can contribute to the flux enhancement in this case, unlike the non-polar species. At 75 km there is a feature in the neutral particle enhancement at 0.6 nm, shown in the figure with a black square. At this point the vapor species is of the same size as the aerosol particle. Also included in Fig. 4.2a is the prediction for the traditional point-molecule condensation model which shows that this feature results from finite molecular size.

The results for the upper atmosphere show an even more pronounced enhancement due to the significantly larger mean free path. The nonpolar species here follow the

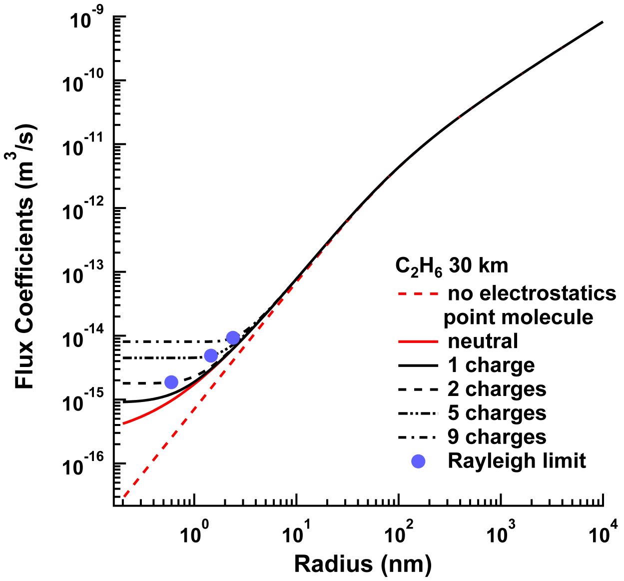

Figure 4.1: Flux enhancement for nonpolar vapor species in the lower atmosphere of Titan.

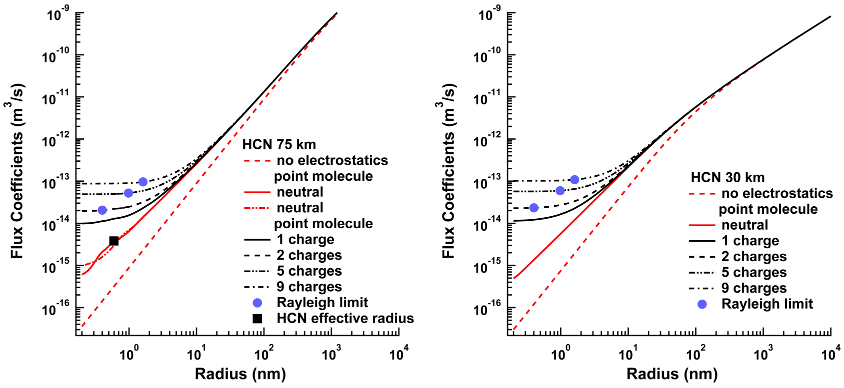

(a) (b)

Figure 4.2: Flux enhancement for polar vapor species at 75 (a) and 30 km (b) on Titan.

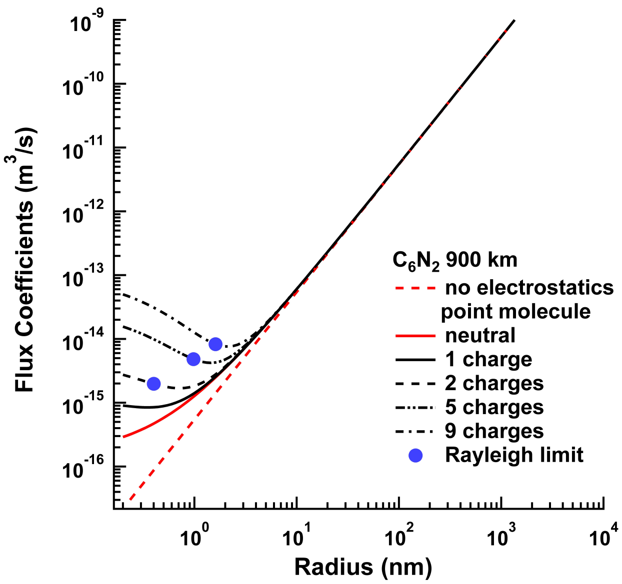

Figure 4.3: Flux enhancement for non-polar vapor species in the upper atmosphere of Titan.

trend for the lower atmosphere, in that the graphs are very similar at both 520 and 900 km, so only the 900 km graph is shown in Fig. 4.3. The effect of the finite molecule size can be seen for all radii <20 nm. At the smallest size, 0.2 nm, it enhances the flux by about an order of magnitude. Electrostatic enhancement can be seen for all particles with radii <4 nm. A single charge contributes another enhancement fact of ∼3 at the smallest sizes. The more exaggerated enhancement curvature for the charged particles in the upper atmosphere is due to having a larger mean free path as the particle is reduced in size. The molecule can approach more closely, and the trajectory can become more curved. C_6N_2 is predicted to have a very high surface tension, so, unlike the non-polars of interest in the lower atmosphere, here the higher charge states can contribute to flux enhancement and particle growth. The polar species, water, shows enhancement across the entire range of particle sizes due to the large mean free path and the induced charge on the particle. The other change of note from the non-polar case is that a single charge is sufficient to increase the flux by another order of magnitude rather than a factor of 3. The CN radical will behave very similarly as their dipole moments are quite close.

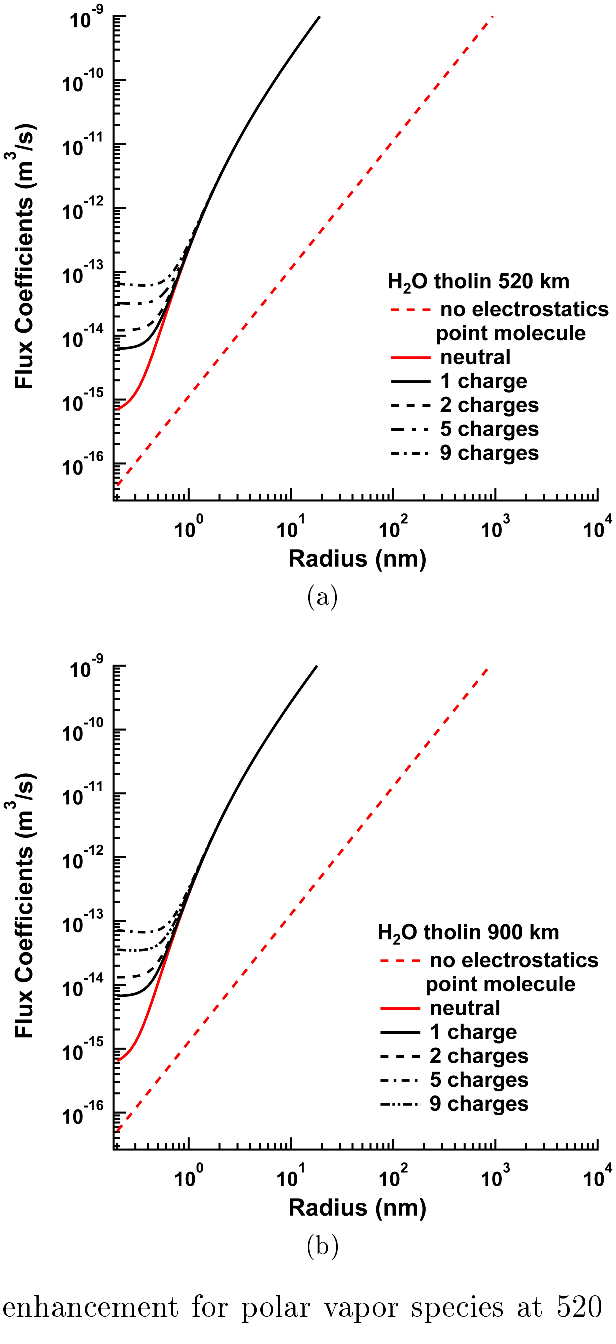

(a)

(b)

Figure 4.4: Flux enhancement for polar vapor species at 520 (a) and 900 km (b) on Titan.

Conclusions

The formation and growth of aerosol particles on Titan is a focus of intense research. Although models currently exist that consider the effects of nucleation and growth within the Titan atmosphere, none that we are aware of account for the flux enhancement of the vapor species to the aerosol particle due to dipole-charge, dipole-dipole, and finite size effects. The results shown here demonstrate that there is a significant enhancement to the flux at small particle sizes, especially for the polar vapor species, which can have flux increases of two orders of magnitude. This suggests that incorporation of these enhancement factors into a microphysical model could make substantial qualitative and quantitative differences to the understanding of aerosol formation and growth throughout the atmosphere.

Acknowledgments

We would like to thank the NASA Astrobiology Institute through the NAI Titan team managed at JPL under NASA Contract NAS7-03001 for the funding of this project, and the Ayrshire Foundation for their support in making computing resources available.

Bibliography

[1] Chemspider: the free chemical database.

[2] D Ajitha and Kimihiko Hirao. Dipole moments of 2Î£ and 2Î states of cn radical at different internuclear distances via fock space multi-reference coupled cluster linear response approach. *Chemical physics letters*, pages 121–126, February 2001.

[3] EJ Davis. The rayleigh limit of charge revisited: light scattering from exploding droplets. *Journal of Aerosol Science*, February 1994.

[4] BN Khare, C Sagan, ET Arakawa, and F Suits. Optical constants of organic tholins produced in a simulated titanian atmosphere: from soft x-ray to microwave frequencies. *Icarus*, February 1984.

[5] P Lavvas and CA Griffith. Condensation in titans atmosphere at the huygens landing site. *Icarus*, February 2011.

[6] P. Lavvas, R. V. von Yelle, C. A. Griffith, and R. V. von Yelle. Titan's vertical aerosol structure at the huygens landing site: Constraints on particle size, density, charge, and refractive index. *Icarus*, 210(2):832–842, 2010.

[7] P. P. Lavvas, A. Coustenis, and I. M. Vardavas. Coupling photochemistry with haze formation in titan's atmosphere, part i: Model description. *Planetary and Space Science*, 56(1):27–66, February 2008.

[8] P. P. Lavvas, A. Coustenis, and I. M. Vardavas. Coupling photochemistry with haze formation in titan's atmosphere, part ii: Results and validation with cassini/huygens data. *Planetary and Space Science*, 56(1):67–99, February 2008.

[9] Panayotis Lavvas, Roger von Yelle, and Véronique Vuitton. The detached haze layer in titan's mesosphere. *Icarus*, 201(2):626–633, July 2009.

[10] David R. Lide. *CRC Handbook of Chemistry and Physics 77th edition 1996-1997*. June 1996.

[11] Xerxes López-Yglesias and Richard Flagan. Ion-aerosol flux coefficients and the steady-state charge distribution of aerosols in a bipolar ion environment. *Aerosol Science and Technology*, 47(6):688–704, 2013.

[12] Xerxes López-Yglesias and Richard Flagan. Population balances of micron sized aerosol particles in a bipolar ion environment. *Aerosol Science and Technology*, 47(6):681–687, 2013.

[13] G. L. Natanson. On the theory of the charging of amicroscopic aerosol particles as a result of capture of gas ions. *SOVIET PHYSICS-TECHNICAL PHYSICS*, 5, February 1960.

[14] WT Norris. Charge images in a dielectric sphere. *IEE Proceedings-Science and Measurement Technology*, 142(2), April 1995.

[15] HR Pruppacher and JD Klett. Microphysics of clouds and precipitation. *1998*, February 1998.

[16] N. B. Vargaftik. *Tables on the thermophysical properties of liquids and gases : in normal and dissociated states*. February 1975.

Chapter 5

The enhancement in the uptake of neutral vapor to aerosol particles in Earth's troposphere due to electrostatic and finite size effects

Xerxes López-Yglesias and Richard Flagan

In this work a model is advanced to calculate the vapor flux to a particle from 0.2 nm to 10 μm in radius with 0 to 9 elementary charges on it. The vapor species considered here are H_2O, H_2SO_4, and NH_3. The aerosol particles that the vapor is approaching are also composed of one of these three species and are assumed to be in a liquid state. The ambient conditions we consider are the bottom and top of the boundary layer, 0 and 1 km respectively, as well as the midtroposphere at 6 km. This model yields enhancement factors of up to an order of magnitude for the smallest, neutral particles if both the finite size of the vapor phase species and the electrostatic potential were previously neglected. If only the potential between the vapor and the neutral particle was neglected, then the maximum enhancement is up to a factor of 3 with the maximum occurring between 1 and 2 nm in particle radius. A single charge on a particle leads to a further enhancement factor of 5, with increasing charge states yielding progressively less enhancement. The higher charge states may not be physically viable. This combination of altitudes and vapor/liquid species was chosen so that the model presented here has direct relevance to the ongoing CLOUD chamber experiments to characterize aerosol particle nucleation and growth.

Introduction

To accurately model and explain Earth's atmosphere and climate, one needs a good understanding of aerosol particle formation and growth. The CLOUD, Cosmics Leaving OUtdoor Droplets, project at CERN is a strong experimental contributor to this understanding[1]. CLOUD consists of an ultra clean atmospheric chamber where pure N_2 and O_2 are added along with controlled concentrations of H_2O, H_2SO_4, and NH_3. NH_3 is a also a contaminant in the chamber, but it can be measured, so the quantity is always known, even if the lower limit is not negligible. The large hadron collider then provides a source of energetic radiation to produce ion pairs to study ion-induced nucleation. The growth of these freshly nucleated particles is then observed within the controlled environment. However, there are many aspects of particle nucleation and growth that are still unknown. In this paper, we will explore a model to describe the enhancement of vapor species flux to a growing cluster/particle as a result of of induced or permanent charge,

Model

Vapor condensation onto a cluster or particle is generally described using a Fickian diffusion model for particles whose radius, a, is large compared to the mean free path of the gas, λ. Such particles are said to be in the continuum size regime. In contrast, transport to the surface of particles in the free molecular or kinetic regime, i.e., those for which $a \gg \lambda$, is described using methods derived from the kinetic theory of gases. No general solution exists for Knudsen numbers, Kn$= \lambda/a$, in the so-called transition regime where the particle radius is comparable to λ, i.e., where Kn$=O(1)$. The flux-matching method of Fuchs and Natanson[2,3] approximates the mass transfer rate in this intermediate regime by applying the kinetic theory model to an inner regime that extends a distance $\Delta = O(\lambda)$ from the surface of the particle, and Fickian diffusion outside of that so-called limiting sphere. By matching the fluxes at the limiting sphere, a factor $\beta(\text{Kn})$ is obtained which accounts for noncontinuous transport effects. Most applications of the flux matching method neglect the finite size of the vapor molecules and intermolecular forces. While these approximations may be reasonable for most aerosol particles due to their large size relative to that of the vapor molecules, it becomes questionable for small clusters involved in nucleation processes.

Here, we extend a model first described by López-Yglesias and Flagan[4,5] that describes molecular fluxes to a particle in the presence of an interaction potential and a background gas. While the prior work considered electromagnetic forces in particle charging, the present work examines the effects of these fields on condensation fluxes to neutral and charged particles. This same extension applied to Titan is gone over in detail in López-Yglesias and Flagan[6].

All of the constituent parts of the model: background gas, vapor species, and particles, must be appropriately parametrized. The background gas is the simplest. The one parameter it has associated with it in this model is it's dielectric constant, calculated from

$$\chi_g = \frac{1 + \frac{8\pi\alpha P}{3k_BT}}{1 - \frac{4\pi\alpha P}{3k_BT}},$$

where P is the pressure. The vapor phase species, though, requires a more detailed description. It has 4 parameters associated with it: diffusivity, polarizability, dipole moment, and mass. The diffusivity value is taken from experimental measurements, and then adjusted for pressure and temperature using the dependence described by Chapman-Enskog theory,

$$D = D_0 \left(\frac{T}{T_0}\right)^{\frac{3}{2}} \left(\frac{P_0}{P}\right),$$

where the 0 subscript refers to the experimental values. Technically, this relationship should also contain the dependence of the collision integral, but since the values are normally of order unity, it's neglected here. The temperature dependence of the polarizability and the dipole moment is similarly neglected in these calculations. Finally, the particle also has four parameters associated with its description: charge, size, surface tension, if it's in a liquid state, and the static dielectric constant. Charge and size are varied within the model. The surface tension, σ, can be used to calculate

Table 5.1: Physical properties of the species under consideration.

	NH_3	H_2SO_4	H_2O
$\alpha \cdot 10^{24}$ (cm^3)	2.81[8]	5.52	1.45[8]
$D \cdot 10^5$ (m^2/s)[9]	2.27 293 K, 1atm	0.75 at 75% RH -0.95 at 0% RH 298 K, 1 atm	2.32 273 K, 1 atm
m (Debye)	1.471[8]	2.9643	1.854[8]
σ (mN/m)	28.662 at 276 K 25.481 at 286 K 22.413 at 296 K[8]	124.135	75.64 at 273.15 K 74.23 at 283.15 K 72.75 at 293.15 K[8]
χ[8]	a=$6.6756 \cdot 10$ b=-$2.9696 \cdot 10^{-1}$ c=$2.5913 \cdot 10^{-4}$ 238.2-323.2 K	122 at 281.15 K 101 at 298.15 K	a=$2.4921 \cdot 10^{2}$ b=-$7.9069 \cdot 10^{-1}$ c=$7.2997 \cdot 10^{-4}$ 273.3-372.2 K

the highest charge state that a particle in the liquid phase can support according to the Rayleigh stability criterion[7],

$$q^2 < 64\pi^2 a^3 \epsilon_0 \chi_g \sigma.$$

This criterion assumes a spherical, liquid droplet covered with a uniform surface charge, totaling q. It then examines the droplet's stability when a physical perturbation is applied. The droplet is stable as long as the forces exerted by the surface tension can compensate for the electrostatic repulsion. Of course, since this analysis assumes continuous charge, it breaks down at low charge states, but it is still a useful gauge. Each particle is assumed to be composed of a single liquid species. To calculate the dielectric constant, a polynomial fit, $\chi_p = a + bT + cT^2$, is used with tabulated values for a, b, and c[8] to describe water and ammonia. Values for sulfuric acid could only be found at 2 temperatures, so we will use whichever value is closest to the temperature used in that simulation.

Results and Discussion

Although the flux enhancement of all three vapor species to all three particle types was considered at the top and bottom of the boundary layer, 0 and 1 km respectively, and in the midtroposphere, 6 km, the results were found to be nearly identical for all particle compositions and heights. The only significant qualitative and quantitative changes shown were in the difference in flux between sulfuric acid and the other two vapor phase species as shown in Fig. 5.1.

The dashed, red lines in Fig. 5.1 represents the results of potential-free, point molecule flux, only taking into account the mean free path, diffusivity, and average speed of the vapor species as the flux is calculated through the transition between the free molecular to continuous regimes. This leads to an enhancement factor of ∼13 for ammonia and water when the finite size of theses two molecules and the attractive potential are taken into account at the smallest particle radii. The potential enhances the flux all the way up to particles of ∼300 nm radius. For sulfuric acid, there is an extra enhancement factor of ∼2 at the smaller particle size due to large differences in the mean free path, diffusivity, and average vapor molecule speed. If the finite size of the vapor phase species is already taken into account, the case shown by the red, dot-dash line, then the enhancement factor from the electrostatic forces is ∼3 for all species with maximum flux enhancement between 1 and 2 nm.

Charge effects contributes a further enhancement factor. It is ∼5 at the smallest particle sizes for a single charge. Further charging leads to further enhancement, but the addition enhancement factor drops with each additional charge (e.g. a factor of ∼2 for the second charge). There is flux enhancement due to charging for particles up to ∼10 nm radius.

For sulfuric acid, the effects of relative humidity were examined to see if they would substantially shift the flux output, as the diffusivity is known to range between 0.075 cm^2/s at 75% RH and 0.095 cm^2/s at 0% RH. The results shown here are for the dry case. A background relative humidity of 70% was only found to cause quantitative changes in flux of up to 25%; thus these variations are omitted from the rest of our analysis.

The blue circles represent the predicted size cutoff from the Rayleigh criterion. Sulfuric acid and water have high surface tension, so the multiply charged states can persist at small particle size and contribute to the total enhancement effect for a given species. Ammonia's surface tension is weaker, and so multiply charged particle aren't likely in the regime where charge plays a role in enhancements. Although, given the ambient conditions modeled, and the charge distribution at these conditions, it is unlikely that any charge state higher than 1 will add a substantial contribution.

Conclusions

The nucleation and initial growth of aerosol particles in Earth's atmosphere is a topic of intense research. Within the field there exist models to calculate condensation, and some that look purely at enhancement effects to the vapor flux due to potentials. Some of these models take into account the molecular species finite size and/or parts of the interaction between a charged particle and a dipole vapor species. The exact potential used in a given model and the methodology of implementing it varies a great deal, but, to our knowledge, this is the first work to consider both dipole-charge and dipole-dipole enhancement effects upon neutral aerosol particles as well as charged particles. The quantitative effects at small particle sizes, like those studied in CLOUD, cause orders of magnitude difference in the predicted flux, including the flux to neutral particles. This suggests that inclusion of these effects in microphysical modeling could cause qualitative and quantitative change in predicted results.

Acknowledgments

We would like to thank the NASA Astrobiology Institute through the NAI Titan team managed at JPL under NASA Contract NAS7-03001 for the funding of this project, and the Ayrshire Foundation for their support in making computing resources available.

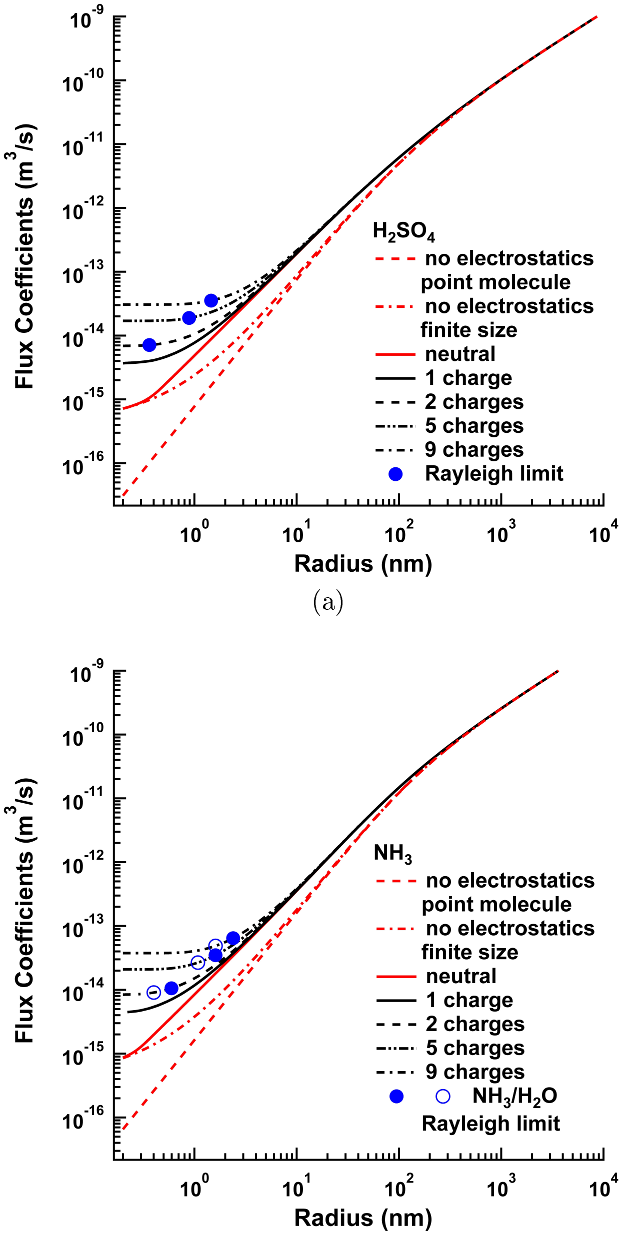

(a)

(b)

Figure 5.1: Enhancement of vapor flux to an aerosol particle due to finite size effects and charge-dipole and dipole-dipole interactions.

Bibliography

[1] Kirkby, J. et al. (2011). Role of sulphuric acid, ammonia and galactic cosmic rays in atmospheric aerosol nucleation. *Nature* **476**:429–433

[2] Fuchs, N.A. (1963). On the Stationary Charge Distribution on Aerosol Particles in a Bipolar Ionic Environment. *Geofis. Pura Appl.* **56**:185-192.

[3] Natanson, G.L. (1960). On the Theory of Charging of Amicroscopic Aerosol Particles as a Result of the Capture of Gas Ions. *Soviet Physics Technical Physics* **5**:538-551.

[4] López-Yglesias, X. and Flagan, R.C. (2013). Population Balances of Micron Sized Aerosol Particles in a Bipolar Ion Environment, *Aerosol Science and Technology* pp. 681-687

[5] López-Yglesias, X. and Flagan, R.C. (2013). Ion-Aerosol Flux Coefficients and the Steady-State Charge Distribution of Aerosols in a Bipolar Ion Environment, *Aerosol Science and Technology* pp. 688-704

[6] López-Yglesias, X and Richard Flagan, (In Progress). The enhancement in the uptake of neutral vapor to aerosol particles in the upper and lower Titan atmosphere due to electrostatic and finite size effects

[7] Davis, EJ. (1994). The Rayleigh limit of charge revisited: light scattering from exploding droplets, *Journal of Aerosol Science*

[8] Lide, DR. (1996). *CRC Handbook of Chemistry and Physics 77th edition 1996-1997*

[9] Vargaftik, NB. (1975) *Tables on the thermophysical properties of liquids and gases : in normal and dissociated states.*

Part II

Whispering Gallery Mode Sensing

Chapter 6

The Physics of Extreme Sensitivity in Whispering Gallery Mode Optical Biosensors[1]

Xerxes López-Yglesias[2], Jason M. Gamba[3], and Richard C. Flagan[4]

Whispering gallery mode (WGM) optical biosensors are capable of extraordinarily sensitive specific and non-specific detection of species suspended in a gas or fluid. Recent experimental results suggest that these devices may attain single-molecule sensitivity to protein solutions in the form of stepwise shifts in their resonance wavelength, λ_R, but present sensor models predict much smaller steps than were reported. This study examines the physical interaction between a WGM sensor and a molecule adsorbed to its surface, exploring assumptions made in previous efforts to model WGM sensor behavior, and describing computational schemes that model the experiments for which single protein sensitivity was reported. The resulting model is used to simulate sensor performance, within constraints imposed by the limited material property data. On this basis, we conclude that nonlinear optical effects would be needed to attain the reported sensitivity, and that, in the experiments for which ex-

---

[1] Reprinted with permission from Lopez-Yglesias, X., Gamba, J. M., & Flagan, R. C. (2012). The physics of extreme sensitivity in whispering gallery mode optical biosensors. Journal of Applied Physics, 111(8), 084701-084701. Copyright 2012, American Institute of Physics.

[2] Department of Physics

[3] The first two authors contributed equally to the present work.

[4] flagan@caltech.edu

Department of Chemical Engineering, California Institute of Technology, 1200 E. California Boulevard, Pasadena, California 91125, USA

treme sensitivity was reported, a bound protein experiences optical energy fluxes too high for such effects to be ignored.

Introduction

Whispering gallery mode (WGM) optical microresonators have emerged as extraordinarily sensitive tools for the label-free detection of biomolecules in solution[1,2,3]. These devices employ a circular resonator made from a dielectric material, most often silica, and typically have diameters less than 200 μm. This results in an adaptable surface chemistry and small effective sensing area. These traits, along with their ability to detect unlabeled biomolecules, make WGM biosensors an appealing technology for the development of analytical and diagnostic instruments, but further development requires an understanding of how these devices function and the limits of their abilities.

Soon after the first application of WGM optical resonators as biosensors[4], researchers demonstrated stepwise shifts in the resonant wavelength, λ_R, upon exposure to nanoparticle[5,6,7,8] and protein solutions[9,10], suggesting single-molecule sensitivity for these species. This intriguing possibility has inspired efforts to reconcile these results[11] with the established model for sensor response presented by Vollmer and Arnold[4,12]. However, that model implicitly assumes a linear optical response and approximates single-molecule contribution to the signal by extrapolating from response predicted for a full monolayer of material.

The adsorption of viral particles and polystyrene beads (200-750 nm diameter) were observed to produce shifts of 10–650 fm (10^{-15} m) in the resonant wavelength of spherical sensors[3,6,7]. It should be noted that these experiments may not fully represent molecular detection studies or be described by previous modeling efforts[4,12] since the analyte is sufficiently large that it does not experience uniform electromagnetic field intensity upon binding. A later study by Lu et al.[8] investigated wavelength shifts in a toroidal sensor due to the adsorption of smaller (25, 50, and 100 nm diameter) polystyrene beads, reporting shifts of 0.4–11 fm. Although significantly smaller than the previously observed beads, these are still an order of magnitude larger than a single protein and too large to experience a uniform field. The greatest WGM sensitivity reported thus far is the 1–30 fm resonance shifts upon *specific* binding of the proteins Interleukin-2 and streptavidin (M_w 15.2 kDa and 60 kDa, respectively, and diameters < 5 nm) to toroidal sensors by Armani et al.[9,10] using uniquely low-loss resonators and high coupled powers. The details of published single-molecule or single-particle experiments involving the measurement of changes to λ_R that result from adsorption of these species are included in Table 6.1 along with abbreviations used to refer to these publications. Additional single-particle studies that measure quantities other than changes in λ_R[13,14] are outside the scope of the present work since direct comparison is impossible.

This study examines the fundamental physical processes involved in the interaction between an optical WGM microresonator and material that adsorbs to its surface in an effort to understand the reported single-molecule sensitivity of these devices. We discuss the validity of assumptions made in previous efforts to model the behavior of WGM biosensors, and describe computational schemes necessary to capture the relevant physical phenomena. Finally, we apply these principles to predict sensor response according to computational capacity and available information about both the material properties and the experimental conditions and protocols employed in the different studies, and compare these results to data from single-molecule sensing experiments presented in SM1.

The WGM Biosensing Experiment

WGM optical resonators support circular modes that are confined to the periphery of the cavity via total internal reflection at the interface between the resonator and the surrounding medium. These modes are excited when the light introduced into the resonator can constructively interfere with itself by completing an integer number of optical cycles in the time required to make one revolution around the cavity. This occurs at the resonant wavelength, λ_R, which, assuming uniform properties around the entire resonator perimeter, can be expressed as

$$\lambda_R \approx 2\pi R_{mode}(T) n_{eff}(T)/M, \tag{6.1}$$

where M is the integer number of wavelengths in the cavity path length; T is temperature; R_{mode} is the effective radius of the mode; and n_{eff} is the effective refractive index of the mode (see Appendix C).

Total internal reflection at the resonator boundary produces an evanescent field in the medium outside the cavity. Material that binds to the device interacts with this electromagnetic field and changes λ_R of a given mode by directly altering the effective refractive index, n_{eff}, or by expanding R_{mode} either through material expansion or through the formation of a layer about the resonator. The resonant shift, $\Delta\lambda_R$, is described by[3]

$$\frac{\Delta\lambda_R}{\lambda_R} = \frac{\Delta n_{eff}}{n_{eff}} + \frac{\Delta R_{mode}}{R_{mode}} \tag{6.2}$$

Processes that alter either n_{eff} or R_{mode}, including the adsorption of material with a refractive index that differs from the medium surrounding the resonator, will result in a change in λ_R of a mode. The magnitude of the resonant shift increases with the contrast in refractive index between the adsorbed material and the surrounding medium it displaces, but sensitivity to single-molecule binding events requires that $\Delta\lambda_R$ exceed the measurement noise of the experiment, which was reported to be $\sigma_{\lambda_R} \approx 0.25$ fm in SM1.

Regardless of whether single molecule binding events are detected, WGM resonator sensors provide an extremely sensitive way to optically probe adsorbed species without measuring spectral features of the molecule or any tag that has been attached to it. Label-free techniques, such as this one avoid altering the behavior of the analyte molecule when attaching a tag, offering the opportunity to study the behavior of molecules in their native state. Detection of a specific analyte in a mixture may be accomplished by functionalizing the resonator surface with an antibody or other molecular recognition agent that binds exclusively to the species of interest. A variety of techniques have been reported for modifying silica surfaces[15].

The experiments leading to the reported single-molecule sensitivity of SM1 involved coupling approximately 1 mW of optical power into low-loss toroidal resonators, resulting in extremely intense electromagnetic fields within the cavity. This field strength is determined by the rate of energy coupled into the device and the rate of optical loss. The quality factor, Q, is the ratio of energy stored within the mode, W_{mode}, to the the energy lost per optical cycle, and serves as a figure of merit for resonant cavities. This quantity may be expressed as $Q = \omega W_{mode}/P_D$, where P_D is the power dissipated by the cavity and ω is the resonant angular frequency. At steady state, the power coupled into the device is equal to P_D. A high quality factor implies a resonator in which losses due to radiative mechanisms, absorption, or scattering are small[16,17].

The studies reported in Table 6.1 span a wide range of experimental and optical parameter space. Two types of resonators were employed: (i) microtoroidal resonators were used in SM1, SM2, and SP4; (ii) microsphere resonators were used in the other studies. Some studies used narrow-linewidth 680 nm lasers to achieve the highest possible Q by minimizing absorptive losses in water, while others used lasers at 765 nm, 1060 nm, and 1310 nm. In all cases, the laser was coupled into the resonator via a tapered optical fiber waveguide. The coupled power used for experiments varied by at least two orders of magnitude from a high of $P_D \approx 1$ mW in SM1; this important parameter is, unfortunately, not uniformly reported in WGM resonator studies. Finally, the quality factor varied from $Q \geq 10^8$ (SM1,SP4) to $0.6 \times 10^6 < Q < 1.5 \times 10^6$ (SP1, SP2, SP3).

The variation in reported sensitivities may, at least in part, be a function of the differences in experimental and physical parameters involved. In the discussion that follows, we model WGM resonator sensor performance for the system for which the greatest sensitivity has been reported, i.e., SM1[9]. In that experiment, the light transmitted through the waveguide was monitored with a photodetector while the wavelength was swept in a sawtooth pattern. None of the studies in Table 6.1 reported the scan rate; however, due to its importance, we obtained[18] the rate for SM1, $|\frac{d\lambda}{dt}| = 1.35\ \frac{\mathrm{nm}}{\mathrm{s}}$. A Lorentzian dip in the transmission spectrum centered at

λ_R indicated that light was coupled out of the waveguide and into a resonant mode, as illustrated in the simulated transmission spectrum in Figure 6.1 for a resonant mode in a device with Q of 10^8. The combination of high Q (10^8) and coupled power ($P_D \approx 1$ mW) used in SM1 has yet to be repeated.

Existing Models of WGM Biosensor Behavior

The first model to describe the WGM sensor response upon binding of protein molecules to its surface is presented by Arnold and Vollmer[12] and treats the bound material as a perturbation to the energy of the optical mode. The resulting shift in resonant wavelength is then expressed as

$$\frac{\delta\lambda_R}{\lambda_R} \approx \frac{\delta W_{mode}}{W_{mode}} \approx \frac{\alpha_{ex}|\mathbf{E}_0(\mathbf{r})^2|}{2\int \epsilon_R |\mathbf{E}_0(\mathbf{r})|^2 \, dV} \tag{6.3}$$

where W_{mode} is the mode energy, α_{ex} is the excess polarizability of the bound material (i.e., the difference in the polarizability of the protein compared and the water it displaced), $\mathbf{E}_0(\mathbf{r})$ is the electric field at position $\mathbf{r}$, ϵ_R is the permittivity of the resonator, and the denominator is integrated over all space. Applying the analytical solutions for the mode in a spherical device and integrating the effect of all molecules present at steady-state surface coverage provides an estimate of the frequency shift as a function of the surface density of bound proteins, σ_p, the refractive indices of the resonator and its surrounding medium, n_R and n_M, respectively, the permittivity of vacuum, ϵ_0, and the effective radius of the mode, R_{mode}, i.e.,

$$\frac{\delta\lambda_R}{\lambda_R} \approx \frac{\alpha_{ex}\sigma_p}{\epsilon_0(n_R^2 - n_M^2)R_{mode}}. \tag{6.4}$$

Teraoka, Arnold and Vollmer[19] completed a more detailed examination of the effect of the protein on the electromagnetic field; they showed that Eq. (6.4) is the first-order perturbation term for the whispering gallery mode resonance.

This model assumes that perturbations to the optical properties of the mode that occur when protein molecules adsorb and displace solvent molecules are independent of the optical field strength. It also assumes that the magnitude of the energy perturbation this protein represents is limited to the difference in the work that must be done to distort the electron distribution of the protein to align with the electric field relative to the electron distribution of the solvent. The molecules are assumed to bind at randomly distributed positions on the sensor surface, a notion in need of validation in light of the subsequent demonstration of optical gradient forces trapping larger species (i.e., nanoparticles) in the evanescent field of a WGM resonator by the same researchers[19] and hydrodynamic focusing in the flowing-sample mode of operation employed in SM1[20]. Nonetheless, this model is an excellent foundation upon which to advance our understanding of these devices. Experimental results presented in Vollmer (2002) and Arnold (2003) use resonators with $Q \approx 2 \times 10^6$ and unspecified coupled power to show that cross-sectional areas for bound proteins calculated from the measured $\Delta\lambda_R$ values agree well with crystallographic data.

The original inference of single-molecule detection with a WGM resonator in SM1[9] presented a model to relate the resonance shift to intuitively important physical parameters. The authors noted that, at high circulating optical power, the effect of a bound molecule may be enhanced due to the thermo-optical effect, wherein the refractive index varies with temperature increases that occur as a result of light absorption by the bound molecule. This dependence is determined by the thermo-optical coefficient, $\frac{dn}{dT}$. The relative single-molecule shift in resonant wavelength was estimated to be

$$\left[\frac{\delta\lambda_R}{\lambda_R}\right]_{SM} = \frac{\sigma\lambda\frac{dn}{dT}}{8\pi^2 n_R^2 \kappa_T V} Q P_D \int \frac{|u(\mathbf{r})|^2}{|\mathbf{r}| + \varepsilon} d\mathbf{r} \tag{6.5}$$

where σ is the absorption cross section of the protein, κ_T is the thermal conductivity of silica, V is the mode volume, $u(\mathbf{r})$ is the “whispering gallery mode field," and ε is a size parameter on the order of the physical radius of the molecule. The model neglects thermal coupling between the resonator and the surrounding fluid, only considering temperature changes within the silica cavity where greater than 95% of the mode energy resides.

Though the authors provide no derivation for Eq. (6.5), it appears to have been inspired by the work of Gorodetskii and Il'chenko[21]. This study describes the heat generated by absorption in a differential volume element, h_V, in terms of the bulk absorption coefficient, α_{abs}, and the energy density of the electric field at that point, $\tilde{W}_e$, as $h_V = \omega\alpha_{abs}\lambda\tilde{W}_e/2\pi n$. Without a detailed derivation of Eqn. (6.5) it is difficult to identify and evaluate all the assumptions that went into the model, but the absence of any time-dependent quantity or heat capacity suggests that steady-state thermal conditions were assumed. Noting a three order of magnitude unit-conversion error in the absorption cross sections of the molecules studied by Armani et al.[9], Arnold[11] argued that this model cannot explain the wavelength shifts that were reported. Though the model appears to poorly describe the data, it suggests that nonlinear physical processes may contribute to the sensor response. If the bound protein causes heating, the strength of the heat source will vary with time as the wavelength is swept and P_D varies. The temperature plume generated by a single bound protein could, through this thermal perturbation, affect a region hundreds of times larger than the molecule itself. This phenomenon, also referred to as photothermal lensing, has been applied with great success to image single molecules by detecting changes in light scattering due to the thermal plume[22,23].

More recently, Arnold et al.[11] consider the heat transfer to estimate the change in temperature experienced by the mode. They argue that the bound protein molecule can be treated as an induced dipole held in an electric field oscillating at frequency ω. The heat generated by the protein in watts, h, is then expressed as the change in the energy of the configuration with time, a quantity that is related to the absorption cross section of the molecule via

$$h = \langle \mathbf{E}(\mathbf{r}_a, t) \cdot \partial\mathbf{p}/\partial t \rangle = \tfrac{1}{2}\omega\varepsilon_0 n_m \sigma \left|\mathbf{E}_0(\mathbf{r}_a)\right|^2/k \tag{6.6}$$

where $\mathbf{E}(\mathbf{r}_a, t) = \mathbf{E}_0(\mathbf{r}_a, t)\exp(i\omega t)$ is the electric field at the position of the protein, $\mathbf{p}$ is the induced dipole moment, $\mathbf{r}_a$ is the position of the protein, ε_0 is the permittivity of vacuum, n_m is the refractive index of the medium surrounding the resonator, and k is the magnitude of the wave-vector in vacuum. This model describes the underlying physical processes that govern the steady-state response to a bound particle or molecule, but does not describe the transient signals produced by the swept-frequency experiments of Armani et al.[9] or any other researchers in the field. Thus, in spite of numerous efforts to model the extreme sensitivity of WGM biosensors, questions remain.

Physical Processes in WGM Sensing

Each of the aforementioned models incorporates simplifying assumptions in an effort to develop analytical descriptions of WGM biosensor resonance shifts. The discussion that follows explores the physical processes in an effort to develop a model that more accurately describes the the experimental system for which extreme sensitivity has been reported.

First, we consider the nature of the WGM sensing experiment. As noted above, the simplest models assume that the laser is continuously tuned to the resonance to enable steady-state operation despite this setup never having been demonstrated experimentally. In contrast, the experiments of Table 6.1 involve sweeping the laser output over a range of wavelengths to find resonance. To capture the widest variety of physical phenomena that may occur using this technique, we model experiments at high P_D and Q. Nanoparticle studies are thus irrelevant to the model under development since there no high-power, high-Q studies to compare with the model. As a result, we consider the single-molecule studies SM1 and SM2.

Excitation of the Optical Mode

Whispering gallery modes may be excited in a variety of closed dielectric structures including rings, disks, spheres, cylinders, tubes, and toroids[1,2]. Each of these geometries has unique mode structures, as illustrated in Figure 6.2 for spherical and toroidal cavities. Predicting how biomolecules that adsorb to the surface of these devices will interact with resonant light begins with an accurate description of this mode structure.

Light is coupled into the microcavity using a waveguide, which we assume here to be a tapered optical fiber waveguide as described above. An evanescent wave decays with distance from the surface of the waveguide; bringing the resonator within the evanescent field couples a traveling wave into the cavity. The extent to which the optical field from the waveguide overlaps the WGM in the resonator determines how much total power can be coupled into the device[24]. Previous studies ignore the method of coupling and assume that a single mode is populated in the WGM resonator[11]. This choice does not necessarily reflect experimental conditions as modes often overlap in wavelength-space, but it appears to be an acceptable approximation. Spherical and cylindrical cavities provide the advantage of well-developed analytical expressions for the electric and magnetic field profiles[25,26] for a variety of coupling methods. Oxborrow[27] presented a convenient, and much more general, method for calculating the mode profile for axisymmetric systems using COMSOL multiphysics, the same finite element solver that we employ below. The numerical solutions obtained via this method must, however, be rescaled to reflect the power coupled into the cavity for a given experiment. Another approximate expression for the mode in a toroid was derived using perturbation theory for quasi-TE and TM modes[28], although those expressions are not provided in their entirety.

Poynting's theorem for harmonic fields may be used to calculate the energy flux inside and outside of the resonator. In the case of no current flow, this is

$$2i\omega \int_V (\tilde{W}_e - \tilde{W}_m)\, dV + \oint_A \mathbf{S} \cdot \mathbf{n}\, da = 0, \tag{6.7}$$

where $\mathbf{S} = \frac{1}{2}\big(\mathbf{E} \times \mathbf{H}^*\big)$ is the time-averaged Poynting vector, $\mathbf{n}$ is the unit normal vector at the differential surface da, $\mathbf{E}$ is the electric field, $\mathbf{H}$ is the auxiliary field, and $\tilde{W}_m$ is the energy density of the magnetic field. The first term in this expression is integrated over the volume of the system and the second term is integrated over the surface area of the system.

For a resonator fabricated from a lossless dielectric, and with no scattering at the resonator boundaries, $\oint_A \mathrm{Re}(\,\mathbf{S} \cdot \mathbf{n})\, da = 0$ because there would be no net energy flow leaving the cavity for such an ideal device. The imaginary part of the Poynting vector for this system is a measure of the circulating, or stored, energy. The materials used in the laboratory are far from ideal, each with its own complex refractive index, so power will be coupled out of the resonator according to the real part of the Poynting vector as scattered and absorbed light. The time-averaged Poynting vector incorporates all the losses due to scattering and heating within both the glass and the surrounding water. It does not include the additional losses due to the perturbation of the system by the protein; these must be evaluated using the light remaining in the resonator ($\mathrm{Im}(\mathbf{S})$). This is similar to the attenuation of circulating power in a resonator by a point defect[29]. A typical value for the time-averaged energy flux at the surface of a microcavity with $Q \approx 10^8$ and $P_D \approx 1$ mW is 1–10×10^{13} W/m^2.

Since the excitation wavelength is scanned during the measurement of the transmission spectrum, the power coupled into the WGM changes as a Lorentzian function of time as the wavelength is scanned at rate $\frac{d\lambda}{dt}$ past the resonance (see Fig. 6.1). For the single-molecule experiments in Table 6.1, the typical time required for optical loss mechanisms and the "ring-up" of the mode to reach a steady state ($\tau_{WGM} < 10$ ns) is very small compared to both the total time for a wavelength scan ($\tau_{scan} \approx 5$ ms) and the time to scan across a single resonance of $Q \approx 10^8$ ($\tau_{res} \approx 5$ μs based on full width at half-maximum of Lorentzian profile). This useful relationship, which may be expressed as $\tau_{WGM} \ll \tau_{res} \ll \tau_{scan}$ suggests that optical timescales may be considered instantaneous.

Interaction of Resonant Light with Surrounding Materials

Here we consider the interaction between the electromagnetic fields in a resonator with $Q \approx 10^8$ and the various materials that play a role in a WGM sensing experiment. As light passes through matter, the time-varying electromagnetic fields interact with the electrons in a material according to its molecular or crystal structure. A single molecule, for example, may have a net dipole moment if it includes net charge or an asymmetric arrangement of atoms with varying electronegativities. Regardless of whether such a permanent dipole exists, an electric field will distort the flexible electron distribution in a material and generate an induced dipole according to the polarizability of the molecule. These dipoles will align themselves to the instantaneous orientation of the electric field. The interactions between light and matter result in a slower propagation than in a vacuum, and are collectively described by the complex refractive index $\tilde{n} = n + i\kappa$. The real part of the refractive index, n, is the ratio of the propagation velocity in vacuum, ν_{vac}, to that in a particular material, ν_{mat}, i.e., $n = \frac{\nu_{\text{vac}}}{\nu_{\text{mat}}} = \frac{\lambda_{\text{vac}}}{\lambda_{\text{mat}}}$. The imaginary part of the refractive index, κ, describes the attenuation of light due to loss mechanisms such as absorption or scattering.

Regardless of whether a protein molecule is present, light circulating within the WGM resonator interacts with the silica cavity and the water surrounding the device. Water molecules form strong hydrogen bonds with one another. The electron distribution in each material undergoes oscillating perturbations in response to the optical field. Water molecules, however, are free to alter their orientation to the extent allowed by their hydrogen bonds. In contrast, silica exists as a rigid amorphous solid whose covalent bonds prohibit any significant translational or rotational motion. The energy that induces this electron and molecular motion is dissipated as heat, leading to linear absorption by these materials in the electromagnetic field.

The presence of a bound protein molecule on the surface of the resonator complicates this response. Each of the amino acids in a protein molecule has a unique permanent dipole moment and molecular polarizability that reflects its composition. Exposure to an electric field induces an additional dipole moment, just as in the silica and water, but the protein can also change its conformation in response to the applied field. The tertiary structure of the protein is determined by the intramolecular forces as well as the energetic incentive to hide hydrophobic regions of the molecule from the surrounding water. What is often thought of as a rigid molecule is, in fact, in continuous flux. Thermal vibrations allow the molecule to sample a range of conformations, all of which are sensitive to interactions with surrounding species and external electric fields. Each conformation has a unique permanent dipole moment, however. Whereas the permanent dipole moment can be treated as a constant for silica and water, this flexibility causes the molecular conformation, induced dipole moment, and permanent dipole moment of the entire protein molecule to become functions of time in the presence of intense, temporally, and spatially varying electric and magnetic fields.

The behavior of the protein in these conditions is even more complex when considering the non-ideality of the interactions between light and matter. It is useful at this point to view the protein as a network of oscillators (i.e., polarizable amino acids) being forced by time-varying optical fields. The timescale of the variation of the electric field ($\tau_{field} \approx 10$ fs) is much shorter than that of molecular motion[30] ($\tau_{molecule} \approx$ 10–1000 fs), so there is a lag between the instantaneous alignment of the field and the orientation of the permanent dipole. In contrast, induced dipoles are established in time $\tau_{electron} \approx 10^{-3}$ fs $\ll \tau_{field}$. The existence of a lag in the alignment of the permanent dipole implies that the electric field must fight the rotational momentum it imparted on the protein during its last optical cycle, increasing the energetic cost as light propagates through the protein. We refer to the work required to align the induced and permanent dipoles as W_A; it depends on protein size, permanent dipole moment, and the polarizability of the constituent amino acids. Only the portion of this work related to the creation and alignment of the induced dipole is considered by Arnold and Vollmer[4,12].

The conformational changes that the protein undergoes may give rise to an additional lag between the orientation of the protein dipole and the electric field alignment. In this case it is more reasonable to view the protein not as a molecule, but as a polymer where each amino acid is responding independently. The 3-dimensional arrangement of these components reflects a vast array of intramolecular interactions that are stretched and bent when an electric field is applied to the molecule. Behaving like springs, these interactions can oppose molecular realignment and increase the amount of work that must be done by the optical fields, W_{IM}. The calculation of W_{IM} based on amino acid sequence or a known tertiary structure has yet to be demonstrated.

Finally, an accurate molecular-scale depiction of the protein must also include the thermal motion that constantly perturbs the tertiary structure of the molecule. The electric field must fight the thermal vibrations of the protein molecule as it changes its conformation. Since each amino acid responds differently to the field according to its physical properties and interactions with nearby amino acids, the degree of thermal vibration is likely nonuniform across the molecule. An electric field must overcome the thermal energy of the system ($E_{thermal} \approx k_B T$, where k_B is the Boltzmann constant) in order to maintain alignment of the dipoles. Therefore, thermal effects could be significant at high optical intensities because of increased absorptive heating, thereby increasing the work to overcome thermal motion, W_T.

The total work done by the propagating optical field on a protein molecule, W_{tot}, may be thus expressed in terms of these three sources

$$W_{tot}(T) = W_A + W_{IM} + W_T(T) \tag{6.8}$$

where W_A describes the work to overcome the forces resulting from a lag in alignment between the electric field and the protein dipole, W_{IM} is the work required to overcome intramolecular forces that introduce additional lag, and W_T is the work done correcting for misalignment due to thermal vibrations. This work is dissipated as heat when the field imparts kinetic energy on the molecule, and that energy is transferred to the surroundings via molecular collisions.

Energy may also be injected into the system as heat if the protein directly absorbs light. Absorption requires the incident light to be at a frequency that excites mechanical or electronic resonances in the molecule. At low optical intensities, the amount of heat generated is proportional to the amount of light absorbed. This process is typically described by the absorption cross section of the molecule, $\sigma(\lambda)$, which is the cross section that a black body absorber would have if it was absorbing as much light as the protein. The absorption cross section of a protein in solution may be calculated based on absorbance measurements in the dilute limit (where scattering and agglomeration may be neglected). Typically, non-fluorescent proteins do not absorb strongly near 680 nm (in contrast to $\lambda < 350$ nm where proteins absorb quite efficiently due to the electronic structure of aromatic amino acids). As a result, concentrations above 10 μM must be used for these absorption spectrophotometry measurements despite the potential for artifacts such as aggregation that may occur at such high concentrations.

The intense optical fields that build up within a WGM resonator with $Q \approx 10^8$ (irradiance $\approx 10^{13}$ W/m^2) suggest that linear absorption may account for only a portion of all energy that is absorbed by a surface-bound protein molecule and consequently dissipated as heat. To date, the contribution of nonlinear phenomena to WGM sensor response has been ignored, but it may be relevant due to the high irradiance experienced by adsorbed material. In fact, the intense circulating powers achievable in WGM resonators have been used to create lasers by doping the dielectric with a gain medium[31,32,33]. An important category of nonlinear effects is optical limiting, which is often studied in chromophores[34,35] with respect to optical limiting switches and other photonic applications[36,37]. This phenomena is characterized by a significant deviation from linear absorption behavior with increasing irradiance. Optical limiting of transmission is often explained by phenomena such as multiphoton absorption, a process involving absorption of an additional photon by a molecule that is already in an excited state. A large irradiance, and the frequent photon interactions that result, are necessary to exceed the threshold at which an additional photon arrives during the lifetime of the excited state. One can imagine that, even for meager absorption, exposure to a sufficiently high power of light would increase the vibrational energy of the protein molecule greatly and may vastly increase the amount of work required to overcome W_T.

Other nonlinear optical phenomena may play a role in WGM sensing as well, including second harmonic generation (SHG) and the Kerr effect. SHG is a second-order nonlinear process that involves the generation of light at $\lambda_{SHG} = \frac{1}{2}\lambda_{input}$, which, for the excitation wavelengths used in WGM biosensing experiments ($\lambda_{input} = 680$ nm), generates light in a range that is absorbed *far* more efficiently (10x or more) by proteins than the WGM excitation light. SHG is more likely to occur at a material interface because inversion symmetry is broken there[38], enabling a weak SHG signal to be generated even in materials such as silica that do not exhibit the phenomena in the bulk[38]. This technique was recently used to demonstrate coherent SHG from a small number of fluorescent molecules patterned on a spherical WGM resonator[39]. The Kerr effect, which is a third-order nonlinear process whereby the refractive index of a material is a function of the electric field strength, has been demonstrated relevant in silica for ultra-high Q resonators at room temperature[46].

Unfortunately, very little information is available on the physical constants describing nonlinear phenomena in non-fluorescent proteins. If a fluorescent species absorbs efficiently, its binding could cause both a resonance shift *and* a step change in the quality factor of the mode[9]. Non-fluorescent species absorb too little light to measure these physical properties using conventional fluorescence spectroscopy. Although it is difficult to generate continuous electromagnetic waves intense enough to probe nonlinear optical phenomena for proteins, ultra high Q WGM resonators generate the needed fields, possibly contributing to the previously reported sensitivities and enabling future study of nonlinear phenomena in biomolecules. Thus, the uv-vis spectrophotometric measurements used to describe simple, linear absorption are likely incomplete.

Heat Transfer

A non-fluorescent protein molecule that absorbs light will generate heat $h = \sigma \mathrm{Im}(\mathbf{S} \cdot \hat{\phi})$, where $\hat{\phi}$ is the unit vector in the direction of light propagation. A fluorescent protein dissipates some of its absorbed energy as light, however the remainder is converted to heat according to $h_f = (1-\eta_q)h$, where η_q is the quantum efficiency of the fluorophore under experimental conditions. The dissipated heat will be removed from the vicinity of the absorbing protein(s) by collisions with surrounding molecules. The thermal coupling of the protein to the resonator and to the surrounding fluid depends on the molecular configuration, which includes a patchy network of hydrophobic and hydrophilic regions, in contrast to the uniform surfaces of polymer beads that have been the subject of numerous studies (see Table 6.1). Recent molecular simulation studies suggest that these local regions of hydrophobicity in the protein can decrease the density of the surrounding water molecules immediately adjacent to those regions, drastically reducing the ability of the protein to transmit its thermal energy to the solvent[41].

Furthermore, in specific binding studies, the protein is not bound directly to the surface of the resonator. Instead, it is tethered to the resonator by the targeting species, which itself has been immobilized to the surface, possibly through covalent linkages. These molecular recognition agents that connect the protein to the resonator surface further differentiate the biomolecule sensing experiments from those involving beads. This may mean that, in the case of the protein, the most efficient means of dissipating energy could be through the high-affinity interactions with the targeting molecule attached to the sensor surface. This could have significant implications on the isotropy of heating that occurs in response to excitation of the protein by the resonant light, suggesting that the molecular properties of the targeting molecule (e.g., rigidity, polarizability, size, etc.) could play a role in the resonance shift observed upon analyte binding. To date, researchers have assumed that the interaction between the targeting species and the mode contributes only to the baseline of the resonance shift measurement and plays no role during the analyte sensing experiment.

The modeling of nanoscale heat transfer requires knowledge about these numerous and complex interactions between a particular protein species and its surroundings[42]. Lacking the data to describe these molecular-scale effects, we assume bulk material properties and energy transport models that apply to macroscopic systems. This assumption is quantitatively accurate within the silica and water, describing the formation of a temperature plume with characteristic radius $l_{plume} \sim (\rho C_P \tau_{res}/\kappa_T)^{-1/2}$, where ρ is the material density and C_P is the heat capacity. There is a transition from a discrete to a continuous system near the protein molecule that will affect the magnitude of the temperature perturbation within this plume and, ultimately, determine the magnitude of the resonance shift. Heat transfer in the continuous system may be described by the heat conduction equation,

$$\mathbf{q} = -\kappa_T \nabla T, \tag{6.9}$$

where the heat flux $\mathbf{q}$ is proportional to the local gradient in temperature. The energy balance for the WGM biosensor system may be expressed as

$$\rho C_P \frac{dT}{dt} + \kappa_T \nabla^2 T = \frac{\omega \alpha \lambda n |\mathbf{E}|^2}{2\pi} + h_{SM} \delta(\mathbf{r} - \mathbf{r_a}), \tag{6.10}$$

where the transient temperature profile, $T(\mathbf{r}, t)$, is evaluated at position $\mathbf{r}$ and time t. All physical properties are a function of $\mathbf{r}$ to account for the different materials. The right side of (6.10) describes heat generation in the system. The first of these terms describes the heat source due to bulk absorption by the resonator and its surroundings[21], while the second term represents that due to the protein at position $\mathbf{r_a}$. Here δ represents the Dirac delta function. In these experiments the protein sits at the interface between two materials, and so thermal dissipation will be anisotropic due to the different physical properties in the resonator and the surrounding fluid (see Supplemental Materials). Note also that the magnitude of the electric field, $|\mathbf{E}(\mathbf{r}, \mathbf{t})|$, is a function of position *and* time because the power is coupled into the resonator in a Lorentzian time pulse (as illustrated in Fig. 6.1) as the wavelength is swept past the resonance.

This Lorentzian functional form represents an ideal case. Its full width at half maximum, τ_{res} (see Fig. 6.1), is determined by the quality factor and the wavelength scan rate, $\frac{d\lambda}{dt}$, according to $Q = \lambda/\delta\lambda = \lambda/(\frac{d\lambda}{dt}\tau_{res})$, as described above. The shape of this function is a challenge to predict *a priori* because it can be strongly affected by bulk heating due to absorption, but the Lorentzian shape and its distortion have been modeled for axisymmetric systems[43]. As the wavelength is swept, absorption warms the resonator and surrounding medium, causing a shift in the resonant wavelength according to the thermo-optical effect. Since their thermo-optical coefficients have opposite signs, the warming of water will produce a resonance shift opposite in sign to that caused by warming silica. This results in an asymmetric broadening or narrowing of the resonance peak in the transmission spectrum depending on that fraction of the mode that overlaps each material[9] or the direction of the wavelength sweep (see Supplemental Material). This effect, discussed in further detail by Carmon, et al.[44], was also observed by Lu and colleagues in SP4 for $P_D \approx 10\ \mu$W and is experimentally demonstrated in the Supplemental Material to this paper. One consequence of this heating effect is that the up scan has a wider resonance peak, which allows power to be coupled in for a longer fraction of the scan, possibly increasing sensitivity. What appears to be a Lorentzian peak in the case of negligible absorption can become a complex function of the material properties and experimental parameters. Schmidt et al.[43], and Rokhsari et al.[40] explore in more detail the role of $\frac{d\lambda}{dt}$ and P_D on the appearance of the transmission spectrum. Transmission curves from biosensing experiments are rarely, if ever, reported. This handicaps efforts to validate any model, as these curves are needed to accurately gage distortion by bulk heating, and the subsequent effects on coupled power throughout the experiment.

The thermal effects that contribute to the distortion of the Lorentzian transmission peak used to identify the instantaneous value of λ_R in a WGM biosensing experiment emphasize the transient nature of the experiment. A measurement with time resolution of τ_{scan} is used to determine a quantity that varies on a timescale τ_{res}. By considering thermal diffusion, we introduce another timescale: the time for a heat source at the sensor surface to be experienced by the optical mode, τ_{HT}. This timescale may be expressed in terms of material properties and the relevant length scale over which diffusion must occur, l_{mode}. We assume that the radial distance from the sensor surface to the peak of the mode intensity as an acceptable approximation of l_{mode}, which gives $\tau_{HT} \approx \frac{r_a^2 \rho C_p}{\kappa_T} \approx 0.3\ \mu$s for the toroidal resonators used in SM1. This value is comparable to τ_{res}, implying that it will take the duration of the pulse before the entire mode experiences the full effect of the heat from a single-molecule source. Our efforts to solve the transient Equation (6.10) represent a significant deviation from previous efforts to model WGM biosensor response[4,12,19,9,11] where no heating or steady-state heating are assumed.

Changing Material Properties

It is evident from the analysis of molecular scale physical processes that no previous effort to describe the WGM sensor device response has modeled the transient sensing experiment in which attomolar sensitivities and single-molecule binding events were observed. By scanning the excitation wavelength in order to measure λ_R, the power coupled into the optical field becomes a function of time and position $\mathbf{r}$. Both linear and nonlinear optical phenomena introduce heat into the system, making the temperature a function of position and time t as well. The electric field and temperature change with time; so too will a number of important physical properties of the system. These include the refractive index and thermo-optical coefficient[47], absorption coefficient, and protein absorption cross section. The resonator may also expand due to bulk temperature increases on the order of 1-10 K according to the thermal expansion coefficient[44], α_{exp}. These effects are summarized in Table 6.2. At the level of the individual protein and its surroundings, any application of bulk material properties may be quite inaccurate due to local variations in density or energy.

Modeling WGM Biosensors

A rigorous model of the transient WGM biosensing experiment must take into account all of the physical processes outlined above, including the time-varying material properties of the system. Calculating the sensor response, $\Delta\lambda_R(t)$, therefore requires a numerical computation scheme like the one depicted in Fig. 6.3a, which involves evaluating the instantaneous value of λ_R at discrete points in time. In this case, accuracy demands that the time steps be sufficiently small to capture the rapid changes that occur in the system due to the Lorentzian shape of the curve in Fig. 6.1. In general, solving for $\Delta\lambda_R(t)$ requires beginning at $t = 0$ and continuing by: (i) evaluating the power coupled into the resonator based on $\lambda(t)$, (ii) determining the material properties of the system as a function of current temperature profile and position, (iii) calculating the 3-dimensional electromagnetic field profile, (iv) evaluating the amount of heat generated by the silica, water and protein according to the electromagnetic field profile, (v) solving for the updated temperature profile, taking into account thermal diffusion, (vi) calculate integral

$$\Delta n_{eff} \approx \frac{\int_V \frac{dn}{dT} \Delta T(\mathbf{r}) |\mathbf{E}(\mathbf{r})| dV}{\int_V |\mathbf{E}(\mathbf{r})| dV} \tag{6.11}$$

to determine $\Delta\lambda_R$, and (vii) stepping Δt in time and repeating this process. A more complete discussion of this computation method is included in the Supplemental Materials.

Simulating all simultaneous physical processes using the scheme in Fig. 6.3a is not presently possible due to the lack of information about how a single protein molecule may respond to the intense optical fields within a WGM resonator with $Q \approx 10^8$. We instead begin by evaluating the assumptions that may be made to simplify this enormous challenge. For example, thermal expansion due to temperature change may be considered negligible according to both theoretical predictions and experimental observations[48], suggesting that we may be able to omit the second term on the right hand side of Eq. 6.2. However, it remains unclear if the thermal perturbation from the protein heat source is significant enough to warrant repeating the mode structure calculation at each computation step in light of the local thermal expansion of the silica that may result. The full, 3-dimensional simulation of the mode structure and solution for the eigenfrequencies (i.e., resonant frequencies) of the mode, followed by the evaluation of the protein heat source and solution of micro-scale heat transfer, would accomplish the same goals as the computation scheme above, but would require a supercomputer to implement.

Finite element analysis has become a valuable tool in solving for such complex systems, and it is particularly well-applied here where computational accuracy and labor can be focused on regions in the geometry where it is needed by generating smaller mesh elements there. We use a commercially available software package, COMSOL Multiphysics, to solve for the electromagnetic field and the temperature profiles, as a function of time in the simple case of a point source of heat at the interface of silica and water blocks.

Here we used the computation scheme outlined in Fig. 6.3b to consider the limiting case where the only heat introduced into the system is due to linear absorption by the protein molecule during a frequency sweep, and the effect that this thermal perturbation has on the mode structure are negligible. These assumptions are identical to those made in previous evaluations of the thermo-optical model of WGM biosensor response [9,11], but our efforts include a consideration of transient heat transfer. We use the Oxborrow method[27] to calculate the electromagnetic field profiles for a toroidal resonator with major radius $r_a = 40\ \mu$m, minor radius $r_i = 2.5\ \mu$m, and material properties as detailed in the Supplemental Materials. We also assume that the analyte is the common tetrameric protein streptavidin[11] ($\mathrm{M_w} \approx 60$ kg/mol) for which $\sigma = 1 \times 10^{-23}\ \mathrm{m}^2$. At peak coupled power the protein molecule is exposed to an irradiance of $6 \times 10^{13}\ \frac{\mathrm{W}}{\mathrm{m}^2}$ and produces a heat of $h_{SM} = \sigma \mathrm{Im}(\mathbf{S} \cdot \hat{\phi}) \approx 6 \times 10^{-10}$ W. Quality factors ranging from 10^6 to 10^8 are also considered.

Results and Discussion

We model the WGM biosensor response to the adsorption of a single protein molecule, as in SM1, using the computational scheme outlined in Fig. 6.3b to solve for the mode structure, the intensity of the single-molecule heat source, and the 3-dimensional transient temperature profile. The results of our finite element model show an asymmetric thermal plume that evolves and expands over time into the silica and the water. A cross-section of the temperature profile at peak coupled power, as well as its overlap with the mode structure, is depicted in Figure 6.4. To better visualize the transient evolution of the plume, we look more closely at the temperature at two points of interest in Figure 6.5. These two points correspond to the location of the protein and the point of maximum mode intensity. Note that the maximum temperature that occurs at the mode peak lags that at the protein. This delay is the time required for the heat to diffuse from the interface to the location of the mode peak, a distance of roughly 0.5 μm according to the Fig. 6.2. The calculated time delay of $\tau_{delay} \approx 0.8\ \mu$s corresponds well to the value of τ_{HT} estimated above, although it should be noted that these simple scaling arguments do not capture the full complexity of the interactions of the thermal plume with the optical mode. This plume may also lead to localized thermal expansion of the resonator and affect sensor response. Modeling the thermal expansion near the protein, we conclude that the temperature rise that results from linear absorption is too small to measurably affect the resonance shift and omit it from further calculations.

We can now estimate the resonance shift by integrating over the calculated 3-dimensional temperature profile according to Eq. (6.11). This integral is evaluated at each time point for a range of quality factors, as shown in Fig. 6.6. The predicted shifts in resonant wavelength for Q values ranging from 10^6 to 10^8 fall between 0.05 to 1.6 am (10^{-18} m), as indicated by the maxima in the curves of Fig. 6.6. The resonance shift corresponding to $Q = 10^8$ is a factor of $10^3 - 10^4$ smaller than the sensor responses observed in SM1 and SM2, suggesting that linear absorption by the protein in the absence of bulk heating is insufficient to explain those experimental results. However, while decreasing Q may also decrease the intensity of the protein heat source, it extends the time power is coupled into the resonator and the duration of the heat pulse. This produces a nonlinear relationship between Q and $\delta\lambda_R$, and a deviation from power law behavior in the inset to Fig. 6.6.

We leave for future work the consideration of bulk heating, decreases in Q due to the accumulation of protein on the sensor, and nonlinear optical effects, the latter which pose a variety of challenges. Bulk heating demands that Eq. (6.10) include the first term on the right side of the equation, increasing the computational demands. Consideration of nonlinear optical effects requires additional knowledge about molecular properties that, if available in the literature, are difficult to locate.

Conclusions

Single-molecule sensitivity in WGM biosensors remains controversial due to the inability to reconcile experimental results with physical models. A review of the models to date reveals an oversimplified physical system and a failure to accurately model the single-molecule experiments. In particular, previous models ignore the exclusively transient nature WGM sensing experiments in the literature, instead adopting a steady-state assumption that precludes relevant physical processes. This time dependence implies that, as the wavelength is scanned during a measurement of λ_R, changes occur in the optical field intensity, the heat generated by the single-molecule source, the temperature profile, and the physical properties of the system. The model presented here incorporates the transient nature of the WGM experiments to predict the observed shift in λ_R, while still making simplifying physical assumptions: (i) the only heat added to the system comes from a protein undergoing linear absorption and (ii) temperature perturbations to the mode structure are negligible. We find that, in the limit of linear absorption by a single protein heat source and consequential thermo-optical effect, even the present, more rigorous model underestimates the reported sensitivity by a factor of $10^3 - 10^4$. Nonetheless, this model lays the groundwork for future studies. Present knowledge of the physical properties of biomolecules bound to the resonator surface limits our ability to model the sensor response. Data on the nonlinear optical coefficients for non-fluorescent proteins are needed, as is a fundamental understanding of energy transfer mechanisms at the single molecule level.

XLS and JMG contributed equally to the present work. The authors would like to thank the Jacobs Institute for Molecular Engineering for Medicine at the California Institute of Technology and the NASA Astrobiology Institute through the NAI Titan team managed at JPL under NASA Contract NAS7-03001 for the funding of this project, and the Ayrshire Foundation for their support in making computing resources available.

Bibliography

[1] A. B. Matsko and V. S. Ilchenko, IEEE J. Sel. Top. Quant. **12**, 3 (2006).

[2] V. S. Ilchenko and A. B. Matsko, IEEE J. Sel. Top. Quant. **12**, 15 (2006).

[3] F. Vollmer and S. Arnold, Nat. Methods **5**, 591 (2008).

[4] F. Vollmer, D. Braun, A. Libchaber, M. Khoshsima, I. Teraoka, and S. Arnold, Appl. Phy. Let. **80**, 4057 (2002).

[5] F. Vollmer, S. Arnold, and D. Keng, P. Natl. Acad. Sci. USA **105**, 20701 (2008).

[6] F. Vollmer and S. Arnold, in *Proc. SPIE*, Biosensing II, Vol. 7397, edited by M. Razhegi and H. Mohseni (2009) 739702-1.

[7] S. Arnold, D. Keng, S. I. Shopova, S. Holler, W. Zurawsky, and F. Vollmer, Opt. Express **17**, 6230 (2009).

[8] T. Lu, H. Lee, T. Chen, S. Herchak, J. Kim, S. Fraser, R. Flagan, and K. Vahala, P. Natl. Acad. Sci. USA **108**, 5976 (2011).

[9] A. M. Armani, R. P. Kulkarni, S. E. Fraser, R. C. Flagan, and K. J. Vahala, Science **317**, 783 (2007).

[10] A. Armani, "Single Molecule Detection Using Optical Microcavities," *Photonic Microresonator Research and Applications*, Springer Series in Optical Sciences, Vol. 156, Ed. I. Chremmos, N. K. Uzunoglu, and O. Schwelb (Springer, New York, 2010).

[11] S. Arnold, S. I. Shopova, and S. Holler, Optics Express **18**, 281 (2010).

[12] S. Arnold, M. Khoshsima, I. Teraoka, S. Holler, and F. Vollmer, Opt. Lett. **28**, 272 (2003).

[13] J. G. Zhu, S. K. Özdemir, Y. F. Xiao, L. Li, D. R. Chen, and L. Yang, Nat. Photonics **4**, 46 (2010).

[14] J. Zhu, c. S. K. Özdemir, L. He, D.-R. Chen, and L. Yang, Opt. Express **19**, 16195 (2011).

[15] H. K. Hunt, C. Soteropulos, and A. M. Armani, Sensors **10**, 9317 (2010).

[16] M. Gorodetsky, A. Savchenkov, and V. Ilchenko, Opt. Lett. **21**, 453 (1996).

[17] X. M. Zhang, H. S. Choi, and A. M. Armani, Appl. Phys. Lett. **96**, 153304 (2010).

[18] A. Armani, *personal communication* **2011**.

[19] I. Teraoka, S. Arnold, and F. Vollmer, J. Opt. Soc. Am. B **20**, 1937 (2003).

[20] J. M. Gamba and R. C. Flagan, Appl. Phys. Lett. **99**, 253705 (2011)

[21] V. S. Il'chenko and M. L. Gorodetskii, Laser Phys. **2**, 1004 (1992).

[22] A. Gaiduk, M. Yorulmaz, P.V. Ruijgrok, and M. Orrit, Science **330**, 353 (2010).

[23] P. Kukura, M. Celebrano, A. Renn, and V. Sandoghar, J. Phys. Chem. Lett. **1**, 3323 (2010).

[24] M. Cai, O. Painter, and K. J. Vahala, Phys. Rev. Lett. **85**, 74 (2000).

[25] C. Bohren and D. Huffman, *Absorption and Scattering of Light by Small Particles* (Wiley-VCH, Weinheim, 2004).

[26] C. Liu, T. Kaiser, S. Lange, and G. Schweiger, Opt. Commun. **117**, 521 (1995).

[27] M. Oxborrow, IEEE T. Micro. Theory **55**, 1209 (2007).

[28] B. Min, L. Yang, and K. Vahala, Phys. Rev. A **76** (2007).

[29] J. Jackson, *Classical Electrodynamics*, 2^{nd} ed. (John Wiley & Sons, New York, 1975).

[30] A. H. Zewail, J. of Phys. Chem. A **104**, 5660 (2000).

[31] V. Sandoghdar, F. Treussart,J. Hare, V. Lefèvre-Seguin, J. M. Raimond, and S. Haroche , Phys. Rev. A **54**, R1777 (1996).

[32] B. Min, T. J. Kippenberg, L. Yang, K. J. Vahala, J. Kalkman, and A. Polman, Phys. Rev. A **70**, 033803 (2004).

[33] H.-S. Hsu, C. Cai, and A. M. Armani, Opt. Express **17**, 23265 (2009).

[34] J. W. Perry, K. Mansour, I.-Y. S. Lee, X.-L. Wu, P. V. Bedworth, C.-T. Chen, D. Ng, S. R. Marder, P. Miles, T. Wada, M. Tian, and H. Sasabe, Science **273**, 1533 (1996).

[35] G. de la Torre, P. Vázquez, F. Agulló-López, and T. Torres, Chem. Rev. **104**, 3723 (2004).

[36] B. LutherDavies and M. Samoc, Curr. Opin. Solid State M. **2**, 213 (1997).

[37] P. Ormos, L. Fabian, L. Oroszi, E. K. Wolff, J. J. Ramsden, and A. Der, App.Phys. Lett. **80**, 4060 (2002).

[38] Y. Shen, Ann.Rev. of Phys. Chem. **40**, 327 (1989).

[39] J. L. Dominguez-Juarez, G. Kozyreff, and J. Martorell, Nat. Commun. **2**, 254 (2011).

[40] H. Rokhsari and K. J. Vahala, Opt. Lett. **30**, 427 (2005).

[41] S. Sarupria and S. Garde, Phys. Rev. Lett. **103**, 037803 (2009).

[42] D. G. Cahill, W. K. Ford, K. E. Goodson, G. D. Mahan, A. Majumdar, H. J.Maris, R. Merlin, and S. Phillpot, J. of Appl.Phys. **93**, 793 (2003).

[43] C. Schmidt, A. Chipouline, T. Käsebier, E. -B. Kley, A. Tünnermann, and T. Pertsch, Appl. Phys. B-Lasers O. **104**, 503 (2011).

[44] T. Carmon, L. Yang, and K. J. Vahala, Opt. Express **12**, 4742 (2004).

[45] C. Schmidt, A. Chipouline, T. Pertsch, A. Tunnermann, O. Egorov, F. Lederer, and L. Deych, Opt. Express **16**, 6285 (2008).

[46] H. Rokhsari, S. M. Spillane, and K. J. Vahala, Appl. Phys. Lett. **85**, 3029 (2004).

[47] G. Abbate, U. Bernini, E. Ragozzino, and F. Somma, J. of Phys. D Appl. Phys. **11**, 1167 (1978).

[48] T. Le, A. Savchenkov, N. Yu, L. Maleki, and W. H. Steier, Appl. Optics **48**, 458 (2009).

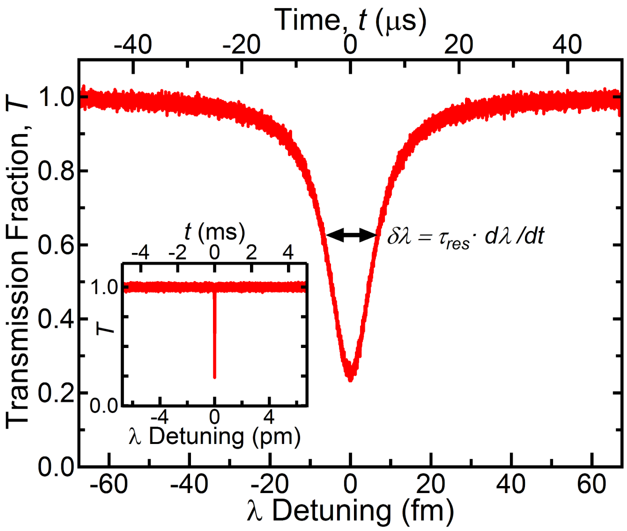

Figure 6.1: Part of a simulated transmission spectrum that might be observed by measuring the photodetector output using an oscilloscope while the wavelength is swept at $\frac{d\lambda}{dt} = 1.35\ \mathrm{nm\,s^{-1}}$ across a resonance with $Q = 10^8$. The full wavelength scan is shown in the inset. The lower horizontal axis is in terms of wavelength detuning from λ_R while the upper is in terms of time.

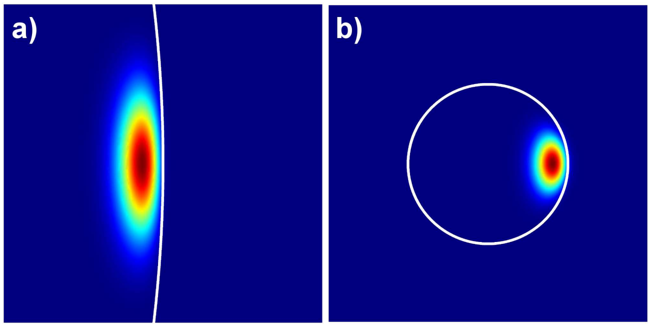

Figure 6.2: The normalized mode intensity for $\lambda_R \approx 680$ nm in a (a) spherical ($R = 42.5\ \mu$m) and (b) toroidal ($r_a = 40\ \mu$m, $r_i = 2.5\ \mu$m) WGM resonator.

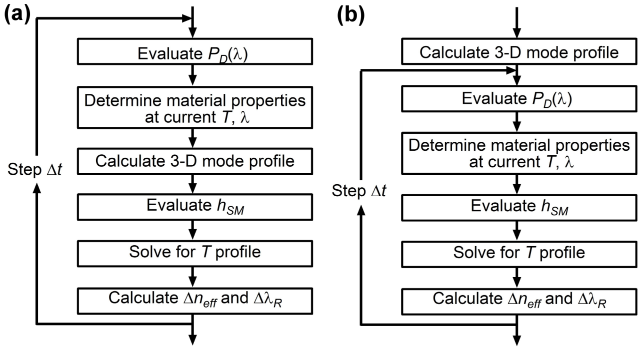

Figure 6.3: (a) Rigorous and (b) modified computation schemes for calculating the WGM sensor response.

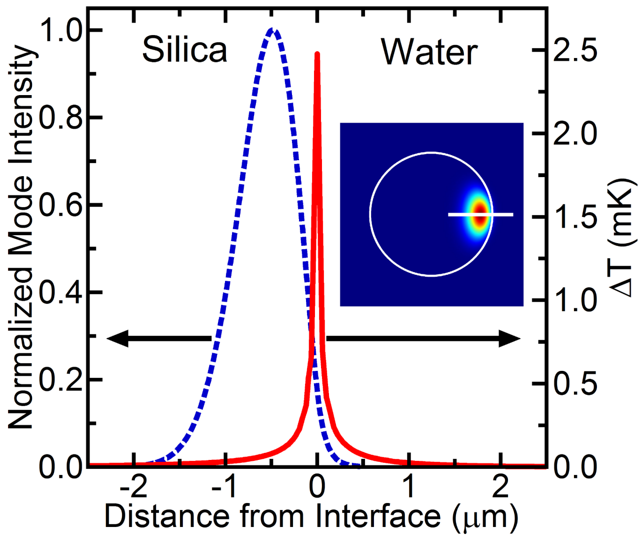

Figure 6.4: The normalized mode profile in a toroidal resonator with major radius $r_a = 40$ μm and minor radius $r_i = 2.5$ μm corresponding to the shown cut line (inset) and the thermal plume resulting from a single-molecule protein heat source exposed to a mode with $Q = 10^8$ and $P_D = 1$ mW resulting in linear absorption by the molecule.

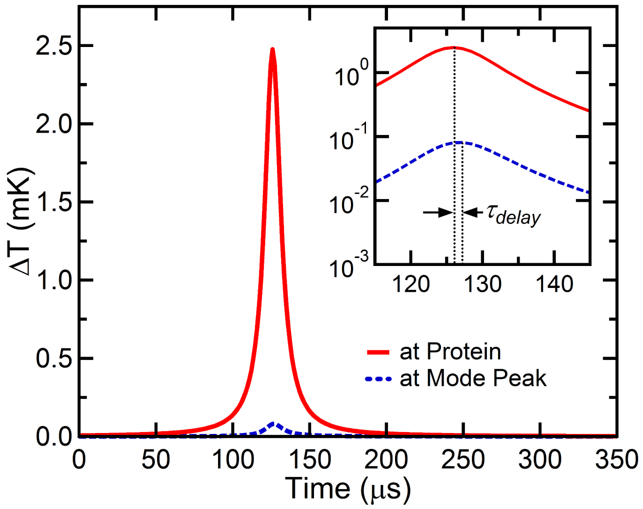

Figure 6.5: The temperature at the location of the protein (red) and mode peak (blue) as a function of time where the only heating comes from a protein exhibiting linear absorption bound to the surface of the toroidal sensor with $Q = 10^8$, $P_D = 1$ mW, and $\frac{d\lambda}{dt} = 1.35\ \mathrm{nm\,s^{-1}}$.

Table 6.1: Single-molecule and Single-particle Detection Using $\Delta\lambda_R$ for WGM Optical Biosensors

	Resonator		**Analyte**						
Code	**Shape**	**Size**[1] (μm)	**Species**[2]	**Size**[3] (nm)	$\boldsymbol{\lambda}$ (nm)	**Q**	$\mathbf{P_D}$	$\boldsymbol{\delta\lambda_R}$ (fm)	**Ref.**
SM1	Toroid	$r_a = 40$ $r_i = 4$	Interleukin-2	< 5	680	$1 - 2 \times 10^8$	≈ 1 mW	$1 - 30$	[9]
SM2	Toroid	[4]	Streptavidin	< 5	680	[4]	[4]	$2 - 30$	[10]
SP1	Sphere	$R = 45$	PSL[5]	200	1310	[4]	[4]	≈ 168	[5]
			PSL[5]	500	1310	[4]	[4]	≈ 655	
			Virion (InfA)	≈ 50	765	6.4×10^5	[4]	11.4	
SP2	Sphere	$R = 53$	PSL[5]	750	1060	1.5×10^6	32μW	≈ 500	[7]
SP3	Sphere	$R = 27$	PSL[5]	500	633	1×10^6	[4]	≈ 550	[6]
SP4	Toroid	[4]	PSL[5]	25	680	1×10^8	$10\ \mu$W	≈ 0.35	[8]
			PSL[5]	50	680	3×10^7	$10\ \mu$W	≈ 0.5	
			PSL[5]	100	680	8×10^6	$10\ \mu$W	≈ 11	
			Virion (InfA)	≈ 50	680	[4]	$10\ \mu$W	$1 - 11$	

---

[a] Outer radii (R) are given for spheres; major (r_a) and minor (r_i) radii are given for toroids

[b] All analytes are detected in aqueous solution

[c] Approximate analyte diameter

[d] Information not provided by the authors

[e] PSL: Polystyrene latex nanoparticle

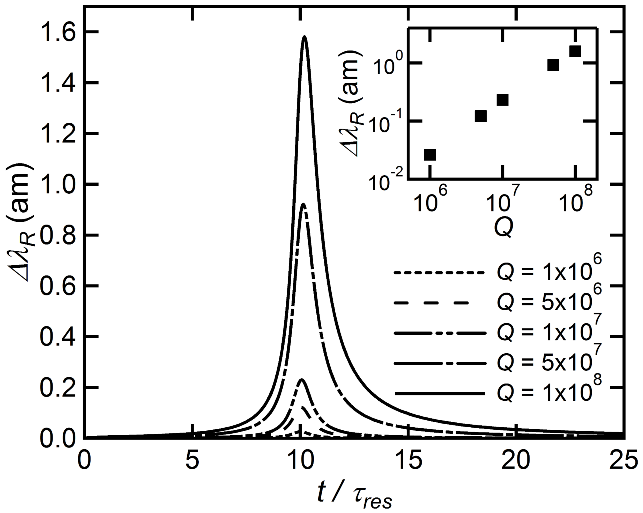

Figure 6.6: The resonance shift due to a single-molecule protein heat source for toroidal resonators ($r_a = 40\ \mu\text{m}, r_i = 2.5\ \mu\text{m}$) with $P_D = 1$ mW and $\frac{d\lambda}{dt} = 1.35\ \text{nm}\,\text{s}^{-1}$ for varying quality factor. This shift is plotted against a relative time t/τ_{res} to simplify comparison. The maximum signal is plotted as a function of Q in the inset.

Table 6.2: Summary of Functional Dependencies of Physical Properties

Refractive Index	$n(T, \|\mathbf{E}\|, \mathbf{r})$
Resonator Radius	$R_{res}(T)$
Bulk Absorption Coefficient	$\alpha_{abs}(T, \|\mathbf{E}\|, \mathbf{r})$
Protein Absorption Cross Section	$\sigma(T, \|\mathbf{E}\|)$

Chapter 7

Future Work

Description of Ion/Molecule-Particle Interaction

We have examined the ion/molecule orbit about the particle/cluster in the limit of a particle that is much more massive than the ion/molecule, as the ion is assumed to orbit about a stationary particle. For small particles, the model should accurately capture their orbit about the center of mass. Using a center of mass formulation may improve differentiation between the fluxes of different ion species, since it will account for differences in ion mass and size.

In addition, the description of the interaction between the ion and the particle upon collision is not well-characterized. What is the accommodation coefficient or "sticking" probability of the ion? Does the resultant charge remain where it lands, or is there transport within the particle? The answer to the first question will, of course, massively change the resultant steady-state charge distribution; the answer to the second could cause significant changes to the calculation of the electromagnetic potential between a charged particle and an ion, especially for a large particle. Presently, this model assumes unity sticking and that particles store their charge at their center. Answering these questions will require very specific chemical knowledge of the ion and particle species involved. And, this will also require some careful thought and expansion to the model, since one would have to take an average of the possible potentials experienced by an ion depending on where the surface charge was on the particle and bear in mind the relative positions of the ion and the surface of the particle. Another method would just be to use a Monte Carlo simulation to deal with the kinetic regime.

Titan and Earth Multi-Species Steady-State Charge Distributions

The current theoretical and experimental description of Titan's atmosphere still has huge gaps in knowledge. A vertical mapping of the steady-state charge distribution throughout the atmosphere would contribute significantly to our understanding of the processes that go on at each altitude, but the current charging model will have to be slightly expanded to accommodate this work. Specifically, the current model is limited to two species of ions, positive and negative. For, at least, portions of Titan's atmosphere current research suggests that at least three ion species are necessary to obtain an accurate model. This means that the rate equations will have to be expanded to accommodate a new possible reaction, and that the currently singular ion recombination term will have to be split into at least two terms. It may be worthwhile to expand it significantly further, so that it can accommodate n-species of ions. Of course, once this is implemented, it would also be worthwhile to make a more careful studies of Earth systems where there are multi-component ionic systems, and the ions that make up the majority of the population are well-characterized. This is not to suggest that a more complex system is always necessary. Several studies have shown that ion composition on Earth varies greatly depending upon the gaseous component in the air at that location

Another component of the steady-state charge distribution that is currently not well characterized is the size-dependence of the number of charge states required to accurately model a distribution. An analytical description of the number of charges required for a given environment and ion population would be very useful in any experimental setting, especially if multi-component ion systems are studied.

In this model the description of the particles in the particle-ion/molecule system has been extended to allow the particle to have any dielectric constant or be a perfect conductor, but what if it was imperfect? What if it was, instead, highly resistive? In this case it would require a finite time for the charge to redistribute, which could significantly affect the trajectory of an inbound molecule or ion.

Particle Nucleation and Growth

In the current model of vapor flux, there is no mechanism for taking into account changes of state, either due to cluster nucleation, evaporation from a particle, or condensation. In order to fully describe the physical processes involved in particle nucleation and growth these aspects of the process must be accounted. Prior to building up such a complex microphysical model, one could begin to estimate the change in the particle vapor pressure due to electromagnetic forces by modeling a molecule at the particle's surface with some velocity directed away from the particle. If this is done for the entire distribution of speeds that the molecule may have, then one can begin to determine the fraction of such molecules that actually escape, from which one can infer a change in the vapor pressure of the particle. In this way the electromagnetic forces acting on a cluster may increase its stability.

Appendix A

Limit of Charge Ratio in Steady State Charge Distribution

The ratio of concentration in successive charge states was earlier found to be

$$\frac{N_k}{N_{k-1}} = \frac{\beta_{k-1,1} n_1}{\beta_{k,-1} n_{-1} (1 + \frac{\beta_{k,1} n_1}{\beta_{k,-1} n_{-1}} - \frac{\beta_{k+1,-1}}{\beta_{k,-1}} \frac{N_{k+1}}{N_k})}. \tag{A.1}$$

In order to evaluate the full steady-state charge distribution, it is instructive, at this point, to examine the asymptotic behavior of $\frac{\beta_{k+1,-1}}{\beta_{k,-1}}$ and $\frac{N_{k+1}}{N_k}$ as $k \to \infty$. The former ratio, shown in Fig. A.1a, approaches 1 at large k. This is to be expected since, for a large enough absolute value of k, a difference of 1 charge is fractionally insignificant to the potential. We see a strong size dependence, with the largest changes per charge step occurring in the kinetic regime, while the continuum regime shows little change throughout. This is caused by the potential increasing the collision cross-section between an ion and a particle within the limiting sphere, but only up to the size of the limiting sphere. In the continuum regime, where the particles are already very near the size of the limiting sphere, the capture cross-section is almost unaffected. The latter ratio, that of the charged populations, is calculated by running the transient model until steady state values are achieved. The results, shown here in Fig. A.1b, follow an exponential decay, approaching 0 with increasing k across all particle sizes. The constant of this decay follows a power law relationship with respect to particle size as shown in Fig. A.1c and is very nearly linear above 300 nm. This physical behavior agrees with our intuition. Each successive charge state becomes harder to fill, and the population of each charge state drops precipitously. Large particles can more easily support higher charge states because of the increased distance between charges.

Applying these results to Eq. (A.1), we can make simplifications. The second factor in the denominator,

$$(1 + \frac{\beta_{k,1} n_1}{\beta_{k,-1} n_{-1}} - \frac{\beta_{k+1,-1}}{\beta_{k,-1}} \frac{N_{k+1}}{N_k}), \tag{A.2}$$

has two terms that both independently approach 0. The second term in Eq. (A.2) becomes vanishingly small as forces between a highly charged particle and an ion increase. This leads to a vanishingly small flux for the repulsive case in the numerator, and a large flux for the attractive case in the denominator. In the third term, $\frac{\beta_{k+1,-1}}{\beta_{k,-1}}$ goes to 1. Fig. A.1 shows that $\frac{N_{k+1}}{N_k} \to 0$ for large k at all sizes. For $k \to K$ large enough such that both terms are arbitrarily close to 0, Eq. (A.1) can be approximated by

$$\frac{N_K}{N_{K-1}} = \frac{\beta_{K-1,1} n_1}{\beta_{K,-1} n_{-1}}. \tag{A.3}$$

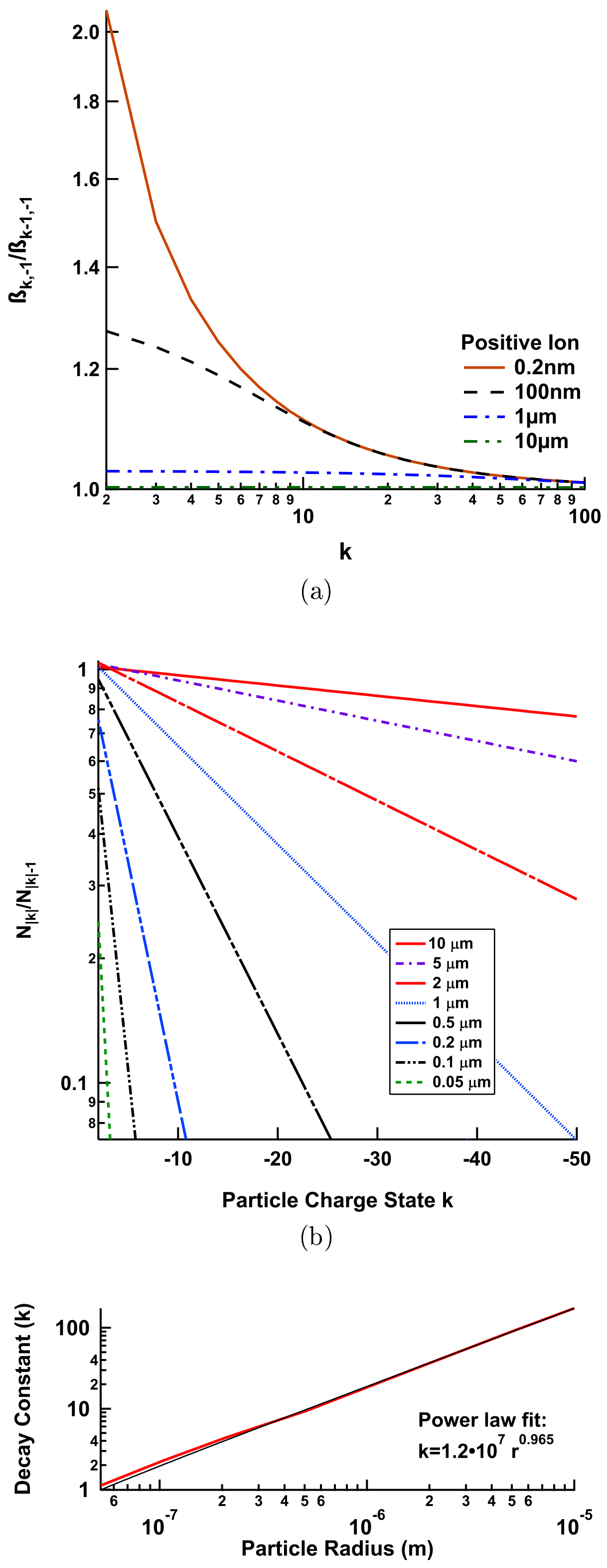

(a)

(b)

(c)

Figure A.1: Ratios of sequential positive ion flux coefficients, β_k/β_{k-1}, and sequential charged populations, $N_{|k|}/N_{|k|-1}$, versus charge state, k. The size dependence of the decay constant for $N_{|k|}/N_{|k|-1}$ is also shown.

Appendix B

Empirical Fits for Ion Flux Coefficients and Steady State Charge Distribution

Flux coefficients and the steady state charge distribution were calculated for particle sizes between $a_p = 0.2$ nm and $a_p = 10$ μm. The approximate formula used for either is $g(k) = 10^{\sum_{i=0}^{11} B_i(k) \log_{10}(a_p)}$ in the style of Wiedensohler (1988). $B_i(k)$ are fit coefficients determined by a least square regression analysis. The fit coefficients for each case covered in the paper are given in the tables in the online Supplemental Information up to $\pm 2e$ particle charge along with the relative error. Delimited tables are available in the individual text files corresponding to the tables presented here with the B_i necessary to calculate both the flux coefficients of particles with charge up to $\pm 10e$ ($\pm 2e$ for water ions) and the steady state charge distribution for particles with charge up to $\pm 5e$ ($\pm 2e$ for water ions).

To calculate the steady state fractional population of particles with charge $> |5e|$, the expression from Gunn and Woessner (1956) may be used,

$$\frac{N_k}{N_T} = \frac{e}{(8\pi^2 a_p k_B T)^{\frac{1}{2}}} \exp\left(\frac{-\left(|k| + \frac{k}{|k|} \frac{4\pi\epsilon_0 a_p k_B T}{e^2} \ln \frac{n_- \mu_-}{n_+ \mu_+} \right)^2}{2\left(\frac{4\pi\epsilon_0 a_p k_B T}{e^2} \right)} \right). \tag{B.1}$$

Table B.1: Flux Coefficients for negative "air" ions to conductive particles where $\beta_{k,i} \geq 10^{-15}$ at 101325 Pa and 298.15 K.

	k				
$B_i(k)$	-2	-1	0	+1	+2
B_0	$-2.47\cdot10^{3}$	$3.22\cdot10^{3}$	$9.47\cdot10^{3}$	$9.34\cdot10^{3}$	$-8.93\cdot10^{3}$
B_1	$-2.51\cdot10^{3}$	$3.04\cdot10^{3}$	$1.06\cdot10^{4}$	$1.07\cdot10^{4}$	$-9.55\cdot10^{3}$
B_2	$-9.75\cdot10^{2}$	$1.09\cdot10^{3}$	$4.93\cdot10^{3}$	$5.09\cdot10^{3}$	$-4.21\cdot10^{3}$
B_3	$-1.59\cdot10^{2}$	$1.61\cdot10^{2}$	$1.19\cdot10^{3}$	$1.26\cdot10^{3}$	$-9.51\cdot10^{2}$
B_4	-1.97	$9.52\cdot10^{-1}$	$1.41\cdot10^{2}$	$1.53\cdot10^{2}$	$-1.03\cdot10^{2}$
B_5	2.30	-2.08	2.52	3.19	$-8.07\cdot10^{-1}$
B_6	$6.04\cdot10^{-2}$	$-3.48\cdot10^{-2}$	-1.26	-1.37	$9.38\cdot10^{-1}$
B_7	$-3.89\cdot10^{-2}$	$3.07\cdot10^{-2}$	$-9.10\cdot10^{-2}$	$-1.05\cdot10^{-1}$	$5.35\cdot10^{-2}$
B_8	$-1.04\cdot10^{-3}$	$5.19\cdot10^{-4}$	$9.71\cdot10^{-3}$	$1.05\cdot10^{-2}$	$-7.36\cdot10^{-3}$
B_9	$7.33\cdot10^{-4}$	$-5.08\cdot10^{-4}$	$1.81\cdot10^{-3}$	$2.04\cdot10^{-3}$	$-1.15\cdot10^{-3}$
B_{10}	$8.26\cdot10^{-5}$	$-5.07\cdot10^{-5}$	$1.04\cdot10^{-4}$	$1.20\cdot10^{-4}$	$-5.95\cdot10^{-5}$
B_{11}	$2.73\cdot10^{-6}$	$-1.50\cdot10^{-6}$	$2.17\cdot10^{-6}$	$2.54\cdot10^{-6}$	$-1.13\cdot10^{-6}$
relative error (min)	$-8.66\cdot10^{-3}$	$-9.06\cdot10^{-3}$	$-8.14\cdot10^{-3}$	$-1.21\cdot10^{-2}$	$-1.53\cdot10^{-2}$
relative error (max)	$9.04\cdot10^{-3}$	$9.84\cdot10^{-3}$	$5.34\cdot10^{-3}$	$1.60\cdot10^{-2}$	$1.67\cdot10^{-2}$

Table B.2: Flux Coefficients for positive "air" ions to conductive particles where $\beta_{k,i} \geq 10^{-15}$ at 101325 Pa and 298.15 K.

	k				
$B_i(k)$	-2	-1	0	+1	+2
B_0	$-1.16\cdot10^{4}$	$9.66\cdot10^{3}$	$1.38\cdot10^{4}$	$-4.89\cdot10^{3}$	$-1.15\cdot10^{4}$
B_1	$-1.25\cdot10^{4}$	$1.10\cdot10^{4}$	$1.53\cdot10^{4}$	$-4.80\cdot10^{3}$	$-1.13\cdot10^{4}$
B_2	$-5.57\cdot10^{3}$	$5.21\cdot10^{3}$	$7.04\cdot10^{3}$	$-1.81\cdot10^{3}$	$-4.18\cdot10^{3}$
B_3	$-1.28\cdot10^{3}$	$1.28\cdot10^{3}$	$1.68\cdot10^{3}$	$-2.86\cdot10^{2}$	$-6.41\cdot10^{2}$
B_4	$-1.41\cdot10^{2}$	$1.55\cdot10^{2}$	$1.95\cdot10^{2}$	-3.89	-2.82
B_5	-1.44	3.15	3.17	3.78	9.18
B_6	1.28	-1.39	-1.76	$1.03\cdot10^{-1}$	$1.47\cdot10^{-1}$
B_7	$7.74\cdot10^{-2}$	$-1.05\cdot10^{-1}$	$-1.22\cdot10^{-1}$	$-5.87\cdot10^{-2}$	$-1.50\cdot10^{-1}$
B_8	$-1.00\cdot10^{-2}$	$1.07\cdot10^{-2}$	$1.36\cdot10^{-2}$	$-1.60\cdot10^{-3}$	$-2.56\cdot10^{-3}$
B_9	$-1.63\cdot10^{-3}$	$2.06\cdot10^{-3}$	$2.46\cdot10^{-3}$	$1.02\cdot10^{-3}$	$2.75\cdot10^{-3}$
B_{10}	$-8.67\cdot10^{-5}$	$1.20\cdot10^{-4}$	$1.40\cdot10^{-4}$	$1.11\cdot10^{-4}$	$2.89\cdot10^{-4}$
B_{11}	$-1.69\cdot10^{-6}$	$2.54\cdot10^{-6}$	$2.88\cdot10^{-6}$	$3.52\cdot10^{-6}$	$9.12\cdot10^{-6}$
relative error (min)	$-1.65\cdot10^{-2}$	$-1.03\cdot10^{-2}$	$-1.56\cdot10^{-2}$	$-8.94\cdot10^{-3}$	$-7.71\cdot10^{-3}$
relative error (max)	$1.85\cdot10^{-2}$	$1.37\cdot10^{-2}$	$1.04\cdot10^{-2}$	$9.37\cdot10^{-3}$	$6.49\cdot10^{-3}$

Table B.3: Steady State distribution for "air" ions and conductive particles where $\frac{N_k}{Z} \geq 1\mathrm{e}-4$ at 101325 Pa and 298.15 K.

	k				
$B_i(k)$	-2	-1	0	+1	+2
B_0	$-4.32\cdot10^{3}$	$-6.18\cdot10^{3}$	$-6.00\cdot10^{3}$	$-1.54\cdot10^{3}$	$-1.18\cdot10^{4}$
B_1	$-4.12\cdot10^{3}$	$-6.85\cdot10^{3}$	$-6.45\cdot10^{3}$	$-1.84\cdot10^{3}$	$-1.13\cdot10^{4}$
B_2	$-1.51\cdot10^{3}$	$-3.17\cdot10^{3}$	$-2.88\cdot10^{3}$	$-9.31\cdot10^{2}$	$-4.12\cdot10^{3}$
B_3	$-2.30\cdot10^{2}$	$-7.60\cdot10^{2}$	$-6.67\cdot10^{2}$	$-2.48\cdot10^{2}$	$-6.23\cdot10^{2}$
B_4	-1.94	$-9.00\cdot10$	$-7.53\cdot10$	$-3.32\cdot10$	-3.32
B_5	3.12	-1.61	$-9.72\cdot10^{-1}$	$-9.93\cdot10^{-1}$	8.53
B_6	$6.58\cdot10^{-2}$	$8.08\cdot10^{-1}$	$6.80\cdot10^{-1}$	$2.92\cdot10^{-1}$	$1.44\cdot10^{-1}$
B_7	$-4.88\cdot10^{-2}$	$5.81\cdot10^{-2}$	$4.41\cdot10^{-2}$	$2.64\cdot10^{-2}$	$-1.34\cdot10^{-1}$
B_8	$-1.07\cdot10^{-3}$	$-6.24\cdot10^{-3}$	$-5.29\cdot10^{-3}$	$-2.22\cdot10^{-3}$	$-2.37\cdot10^{-3}$
B_9	$8.57\cdot10^{-4}$	$-1.16\cdot10^{-3}$	$-9.07\cdot10^{-4}$	$-4.92\cdot10^{-4}$	$2.35\cdot10^{-3}$
B_{10}	$9.11\cdot10^{-5}$	$-6.60\cdot10^{-5}$	$-5.00\cdot10^{-5}$	$-3.03\cdot10^{-5}$	$2.43\cdot10^{-4}$
B_{11}	$2.87\cdot10^{-6}$	$-1.37\cdot10^{-6}$	$-1.01\cdot10^{-6}$	$-6.64\cdot10^{-7}$	$7.51\cdot10^{-6}$
relative error (min)	$-6.58\cdot10^{-3}$	$-1.60\cdot10^{-2}$	$-3.43\cdot10^{-3}$	$-2.08\cdot10^{-2}$	$-7.52\cdot10^{-3}$
relative error (max)	$6.90\cdot10^{-3}$	$1.46\cdot10^{-2}$	$4.12\cdot10^{-3}$	$1.59\cdot10^{-2}$	$7.12\cdot10^{-3}$

Table B.4: Flux Coefficients for negative water ions to conductive particles where $\beta_{k,i} \geq 10^{-15}$ at 101325 Pa and 298.15 K.

	k				
$B_i(k)$	-2	-1	0	+1	+2
B_0	$-2.42\cdot10^{3}$	$3.31\cdot10^{3}$	$9.47\cdot10^{3}$	$8.73\cdot10^{3}$	$-8.95\cdot10^{3}$
B_1	$-2.46\cdot10^{3}$	$3.12\cdot10^{3}$	$1.06\cdot10^{4}$	$1.00\cdot10^{4}$	$-9.57\cdot10^{3}$
B_2	$-9.56\cdot10^{2}$	$1.12\cdot10^{3}$	$4.93\cdot10^{3}$	$4.79\cdot10^{3}$	$-4.22\cdot10^{3}$
B_3	$-1.56\cdot10^{2}$	$1.66\cdot10^{2}$	$1.19\cdot10^{3}$	$1.19\cdot10^{3}$	$-9.53\cdot10^{2}$
B_4	-1.95	1.02	$1.41\cdot10^{2}$	$1.46\cdot10^{2}$	$-1.03\cdot10^{2}$
B_5	2.26	-2.14	2.52	3.10	$-8.12\cdot10^{-1}$
B_6	$5.95\cdot10^{-2}$	$-3.64\cdot10^{-2}$	-1.26	-1.30	$9.40\cdot10^{-1}$
B_7	$-3.82\cdot10^{-2}$	$3.17\cdot10^{-2}$	$-9.10\cdot10^{-2}$	$-1.00\cdot10^{-1}$	$5.36\cdot10^{-2}$
B_8	$-1.02\cdot10^{-3}$	$5.45\cdot10^{-4}$	$9.71\cdot10^{-3}$	$9.95\cdot10^{-3}$	$-7.38\cdot10^{-3}$
B_9	$7.20\cdot10^{-4}$	$-5.25\cdot10^{-4}$	$1.81\cdot10^{-3}$	$1.95\cdot10^{-3}$	$-1.15\cdot10^{-3}$
B_{10}	$8.12\cdot10^{-5}$	$-5.25\cdot10^{-5}$	$1.04\cdot10^{-4}$	$1.15\cdot10^{-4}$	$-5.97\cdot10^{-5}$
B_{11}	$2.69\cdot10^{-6}$	$-1.56\cdot10^{-6}$	$2.17\cdot10^{-6}$	$2.44\cdot10^{-6}$	$-1.14\cdot10^{-6}$
relative error (min)	$-8.71\cdot10^{-3}$	$-9.12\cdot10^{-3}$	$-8.14\cdot10^{-3}$	$-1.47\cdot10^{-2}$	$-1.53\cdot10^{-2}$
relative error (max)	$9.07\cdot10^{-3}$	$9.89\cdot10^{-3}$	$5.34\cdot10^{-3}$	$1.93\cdot10^{-2}$	$1.67\cdot10^{-2}$

Table B.5: Flux Coefficients for positive water ions to conductive particles where $\beta_{k,i} \geq 10^{-15}$ at 101325 Pa and 298.15 K.

			k		
$B_i(k)$	-2	-1	0	+1	+2
B_0	$-1.16\cdot10^{4}$	$9.29\cdot10^{3}$	$1.38\cdot10^{4}$	$-4.82\cdot10^{3}$	$-1.15\cdot10^{4}$
B_1	$-1.25\cdot10^{4}$	$1.06\cdot10^{4}$	$1.53\cdot10^{4}$	$-4.74\cdot10^{3}$	$-1.12\cdot10^{4}$
B_2	$-5.57\cdot10^{3}$	$5.03\cdot10^{3}$	$7.04\cdot10^{3}$	$-1.78\cdot10^{3}$	$-4.16\cdot10^{3}$
B_3	$-1.28\cdot10^{3}$	$1.24\cdot10^{3}$	$1.68\cdot10^{3}$	$-2.82\cdot10^{2}$	$-6.37\cdot10^{2}$
B_4	$-1.41\cdot10^{2}$	$1.50\cdot10^{2}$	$1.95\cdot10^{2}$	-3.84	-2.80
B_5	-1.44	3.07	3.17	3.73	9.13
B_6	1.28	-1.34	-1.76	$1.01\cdot10^{-1}$	$1.46\cdot10^{-1}$
B_7	$7.74\cdot10^{-2}$	$-1.02\cdot10^{-1}$	$-1.22\cdot10^{-1}$	$-5.79\cdot10^{-2}$	$-1.49\cdot10^{-1}$
B_8	$-1.00\cdot10^{-2}$	$1.03\cdot10^{-2}$	$1.36\cdot10^{-2}$	$-1.58\cdot10^{-3}$	$-2.55\cdot10^{-3}$
B_9	$-1.63\cdot10^{-3}$	$2.00\cdot10^{-3}$	$2.46\cdot10^{-3}$	$1.00\cdot10^{-3}$	$2.73\cdot10^{-3}$
B_{10}	$-8.67\cdot10^{-5}$	$1.17\cdot10^{-4}$	$1.40\cdot10^{-4}$	$1.09\cdot10^{-4}$	$2.88\cdot10^{-4}$
B_{11}	$-1.69\cdot10^{-6}$	$2.47\cdot10^{-6}$	$2.88\cdot10^{-6}$	$3.47\cdot10^{-6}$	$9.07\cdot10^{-6}$
relative error (min)	$-1.65\cdot10^{-2}$	$-1.12\cdot10^{-2}$	$-1.56\cdot10^{-2}$	$-9.05\cdot10^{-3}$	$-7.69\cdot10^{-3}$
relative error (max)	$1.86\cdot10^{-2}$	$1.48\cdot10^{-2}$	$1.04\cdot10^{-2}$	$9.44\cdot10^{-3}$	$6.51\cdot10^{-3}$

Table B.6: Steady State distribution for water ions and conductive particles where $\frac{N_k}{Z} \geq 1\mathrm{e}-4$ at 101325 Pa and 298.15 K.

			k		
$B_i(k)$	-2	-1	0	+1	+2
B_0	$-4.28\cdot10^{3}$	$-5.82\cdot10^{3}$	$-6.00\cdot10^{3}$	$-9.26\cdot10^{2}$	$-1.18\cdot10^{4}$
B_1	$-4.08\cdot10^{3}$	$-6.45\cdot10^{3}$	$-6.45\cdot10^{3}$	$-1.18\cdot10^{3}$	$-1.13\cdot10^{4}$
B_2	$-1.49\cdot10^{3}$	$-2.98\cdot10^{3}$	$-2.89\cdot10^{3}$	$-6.34\cdot10^{2}$	$-4.11\cdot10^{3}$
B_3	$-2.29\cdot10^{2}$	$-7.17\cdot10^{2}$	$-6.68\cdot10^{2}$	$-1.79\cdot10^{2}$	$-6.21\cdot10^{2}$
B_4	-1.91	$-8.51\cdot10$	$-7.53\cdot10$	$-2.55\cdot10$	-3.30
B_5	3.09	-1.53	$-9.73\cdot10^{-1}$	$-9.03\cdot10^{-1}$	8.51
B_6	$6.52\cdot10^{-2}$	$7.63\cdot10^{-1}$	$6.80\cdot10^{-1}$	$2.22\cdot10^{-1}$	$1.44\cdot10^{-1}$
B_7	$-4.84\cdot10^{-2}$	$5.51\cdot10^{-2}$	$4.41\cdot10^{-2}$	$2.21\cdot10^{-2}$	$-1.33\cdot10^{-1}$
B_8	$-1.06\cdot10^{-3}$	$-5.90\cdot10^{-3}$	$-5.29\cdot10^{-3}$	$-1.67\cdot10^{-3}$	$-2.36\cdot10^{-3}$
B_9	$8.50\cdot10^{-4}$	$-1.10\cdot10^{-3}$	$-9.08\cdot10^{-4}$	$-4.02\cdot10^{-4}$	$2.34\cdot10^{-3}$
B_{10}	$9.03\cdot10^{-5}$	$-6.26\cdot10^{-5}$	$-5.00\cdot10^{-5}$	$-2.55\cdot10^{-5}$	$2.42\cdot10^{-4}$
B_{11}	$2.84\cdot10^{-6}$	$-1.30\cdot10^{-6}$	$-1.01\cdot10^{-6}$	$-5.69\cdot10^{-7}$	$7.49\cdot10^{-6}$
relative error (min)	$-6.63\cdot10^{-3}$	$-1.71\cdot10^{-2}$	$-3.43\cdot10^{-3}$	$-2.42\cdot10^{-2}$	$-7.50\cdot10^{-3}$
relative error (max)	$6.95\cdot10^{-3}$	$1.48\cdot10^{-2}$	$4.12\cdot10^{-3}$	$1.78\cdot10^{-2}$	$7.10\cdot10^{-3}$

Table B.7: Flux Coefficients for negative “air” ions to conductive particles where $\beta_{k,i} \geq 10^{-15}$ at 4480 Pa and 218.15 K.

	k				
$B_i(k)$	-2	-1	0	+1	+2
B_0	$2.35\cdot10^{3}$	$1.64\cdot10^{3}$	$6.26\cdot10^{3}$	$-1.13\cdot10^{4}$	$-1.65\cdot10^{4}$
B_1	$2.23\cdot10^{3}$	$1.58\cdot10^{3}$	$7.15\cdot10^{3}$	$-1.23\cdot10^{4}$	$-1.85\cdot10^{4}$
B_2	$7.96\cdot10^{2}$	$5.72\cdot10^{2}$	$3.38\cdot10^{3}$	$-5.58\cdot10^{3}$	$-8.58\cdot10^{3}$
B_3	$1.14\cdot10^{2}$	$8.56\cdot10$	$8.32\cdot10^{2}$	$-1.30\cdot10^{3}$	$-2.06\cdot10^{3}$
B_4	$-8.24\cdot10^{-1}$	$3.59\cdot10^{-1}$	$1.01\cdot10^{2}$	$-1.47\cdot10^{2}$	$-2.43\cdot10^{2}$
B_5	-1.66	-1.16	2.07	-1.88	-4.14
B_6	$-1.74\cdot10^{-3}$	$-1.67\cdot10^{-2}$	$-9.03\cdot10^{-1}$	1.33	2.18
B_7	$2.65\cdot10^{-2}$	$1.77\cdot10^{-2}$	$-6.87\cdot10^{-2}$	$8.53\cdot10^{-2}$	$1.54\cdot10^{-1}$
B_8	$4.62\cdot10^{-5}$	$2.53\cdot10^{-4}$	$6.93\cdot10^{-3}$	$-1.04\cdot10^{-2}$	$-1.69\cdot10^{-2}$
B_9	$-4.80\cdot10^{-4}$	$-3.03\cdot10^{-4}$	$1.34\cdot10^{-3}$	$-1.76\cdot10^{-3}$	$-3.08\cdot10^{-3}$
B_{10}	$-4.51\cdot10^{-5}$	$-3.01\cdot10^{-5}$	$7.87\cdot10^{-5}$	$-9.60\cdot10^{-5}$	$-1.75\cdot10^{-4}$
B_{11}	$-1.29\cdot10^{-6}$	$-8.89\cdot10^{-7}$	$1.67\cdot10^{-6}$	$-1.91\cdot10^{-6}$	$-3.61\cdot10^{-6}$
relative error (min)	$-1.12\cdot10^{-3}$	$-7.27\cdot10^{-4}$	$-8.85\cdot10^{-3}$	$-1.96\cdot10^{-2}$	$-1.41\cdot10^{-2}$
relative error (max)	$8.57\cdot10^{-4}$	$5.72\cdot10^{-4}$	$8.43\cdot10^{-3}$	$1.53\cdot10^{-2}$	$1.25\cdot10^{-2}$

Table B.8: Flux Coefficients for positive “air” ions to conductive particles where $\beta_{k,i} \geq 10^{-15}$ at 4480 Pa and 218.15 K.

	k				
$B_i(k)$	-2	-1	0	+1	+2
B_0	$-1.78\cdot10^{4}$	$-1.26\cdot10^{4}$	$7.15\cdot10^{3}$	$7.63\cdot10^{2}$	$6.20\cdot10^{2}$
B_1	$-1.99\cdot10^{4}$	$-1.38\cdot10^{4}$	$8.09\cdot10^{3}$	$7.18\cdot10^{2}$	$5.43\cdot10^{2}$
B_2	$-9.24\cdot10^{3}$	$-6.24\cdot10^{3}$	$3.81\cdot10^{3}$	$2.53\cdot10^{2}$	$1.71\cdot10^{2}$
B_3	$-2.21\cdot10^{3}$	$-1.46\cdot10^{3}$	$9.28\cdot10^{2}$	$3.62\cdot10$	$1.93\cdot10$
B_4	$-2.60\cdot10^{2}$	$-1.66\cdot10^{2}$	$1.12\cdot10^{2}$	$-6.99\cdot10^{-2}$	$-9.04\cdot10^{-1}$
B_5	-4.35	-2.21	2.21	$-4.87\cdot10^{-1}$	$-2.70\cdot10^{-1}$
B_6	2.34	1.50	-1.00	$-2.93\cdot10^{-3}$	$1.44\cdot10^{-2}$
B_7	$1.64\cdot10^{-1}$	$9.75\cdot10^{-2}$	$-7.50\cdot10^{-2}$	$7.23\cdot10^{-3}$	$3.54\cdot10^{-3}$
B_8	$-1.81\cdot10^{-2}$	$-1.17\cdot10^{-2}$	$7.69\cdot10^{-3}$	$3.72\cdot10^{-5}$	$-2.47\cdot10^{-4}$
B_9	$-3.28\cdot10^{-3}$	$-2.00\cdot10^{-3}$	$1.47\cdot10^{-3}$	$-1.21\cdot10^{-4}$	$-5.21\cdot10^{-5}$
B_{10}	$-1.86\cdot10^{-4}$	$-1.10\cdot10^{-4}$	$8.59\cdot10^{-5}$	$-1.09\cdot10^{-5}$	$-9.45\cdot10^{-7}$
B_{11}	$-3.83\cdot10^{-6}$	$-2.20\cdot10^{-6}$	$1.81\cdot10^{-6}$	$-2.96\cdot10^{-7}$	$8.26\cdot10^{-8}$
relative error (min)	$-1.23\cdot10^{-2}$	$-1.95\cdot10^{-2}$	$-8.98\cdot10^{-3}$	$-5.84\cdot10^{-4}$	$-6.95\cdot10^{-4}$
relative error (max)	$1.35\cdot10^{-2}$	$1.63\cdot10^{-2}$	$8.55\cdot10^{-3}$	$4.69\cdot10^{-4}$	$7.72\cdot10^{-4}$

Table B.9: Steady State distribution for “air” ions and conductive particles where $\frac{N_k}{Z} \geq 1\mathrm{e}-4$ at 4480 Pa and 218.15 K.

			k		
$B_i(k)$	-2	-1	0	+1	+2
B_0	$1.43\cdot10^{3}$	$1.78\cdot10^{4}$	$-1.02\cdot10^{3}$	$1.74\cdot10^{4}$	$-2.71\cdot10^{2}$
B_1	$1.36\cdot10^{3}$	$1.99\cdot10^{4}$	$-9.89\cdot10^{2}$	$1.94\cdot10^{4}$	$-3.09\cdot10^{2}$
B_2	$4.74\cdot10^{2}$	$9.22\cdot10^{3}$	$-4.05\cdot10^{2}$	$8.98\cdot10^{3}$	$-1.46\cdot10^{2}$
B_3	$6.45\cdot10$	$2.20\cdot10^{3}$	$-8.69\cdot10$	$2.14\cdot10^{3}$	$-3.10\cdot10$
B_4	$-8.52\cdot10^{-1}$	$2.58\cdot10^{2}$	-9.19	$2.50\cdot10^{2}$	-1.46
B_5	$-8.71\cdot10^{-1}$	4.19	$-9.10\cdot10^{-2}$	3.99	$4.56\cdot10^{-1}$
B_6	$9.61\cdot10^{-3}$	-2.32	$8.24\cdot10^{-2}$	-2.25	$3.30\cdot10^{-2}$
B_7	$1.23\cdot10^{-2}$	$-1.61\cdot10^{-1}$	$5.32\cdot10^{-3}$	$-1.55\cdot10^{-1}$	$-8.80\cdot10^{-3}$
B_8	$-1.91\cdot10^{-4}$	$1.80\cdot10^{-2}$	$-6.33\cdot10^{-4}$	$1.74\cdot10^{-2}$	$-5.70\cdot10^{-4}$
B_9	$-1.94\cdot10^{-4}$	$3.23\cdot10^{-3}$	$-1.12\cdot10^{-4}$	$3.12\cdot10^{-3}$	$1.82\cdot10^{-4}$
B_{10}	$-1.39\cdot10^{-5}$	$1.82\cdot10^{-4}$	$-6.45\cdot10^{-6}$	$1.75\cdot10^{-4}$	$2.52\cdot10^{-5}$
B_{11}	$-2.78\cdot10^{-7}$	$3.73\cdot10^{-6}$	$-1.36\cdot10^{-7}$	$3.59\cdot10^{-6}$	$9.33\cdot10^{-7}$
relative error (min)	$-2.28\cdot10^{-3}$	$-2.17\cdot10^{-2}$	$-2.76\cdot10^{-3}$	$-2.24\cdot10^{-2}$	$-2.00\cdot10^{-3}$
relative error (max)	$2.19\cdot10^{-3}$	$2.27\cdot10^{-2}$	$1.77\cdot10^{-3}$	$2.43\cdot10^{-2}$	$2.32\cdot10^{-3}$

Table B.10: Flux Coefficients for negative water ions to conductive particles where $\beta_{k,i} \geq 10^{-15}$ at 4480 Pa and 218.15 K.

			k		
$B_i(k)$	-2	-1	0	+1	+2
B_0	$2.40\cdot10^{3}$	$1.69\cdot10^{3}$	$6.26\cdot10^{3}$	$-1.32\cdot10^{4}$	$-2.29\cdot10^{4}$
B_1	$2.28\cdot10^{3}$	$1.63\cdot10^{3}$	$7.15\cdot10^{3}$	$-1.44\cdot10^{4}$	$-2.55\cdot10^{4}$
B_2	$8.13\cdot10^{2}$	$5.92\cdot10^{2}$	$3.38\cdot10^{3}$	$-6.49\cdot10^{3}$	$-1.18\cdot10^{4}$
B_3	$1.17\cdot10^{2}$	$8.87\cdot10$	$8.32\cdot10^{2}$	$-1.51\cdot10^{3}$	$-2.83\cdot10^{3}$
B_4	$-8.12\cdot10^{-1}$	$3.92\cdot10^{-1}$	$1.01\cdot10^{2}$	$-1.70\cdot10^{2}$	$-3.33\cdot10^{2}$
B_5	-1.70	-1.20	2.07	-2.10	-5.61
B_6	$-2.40\cdot10^{-3}$	$-1.77\cdot10^{-2}$	$-9.03\cdot10^{-1}$	1.54	2.99
B_7	$2.72\cdot10^{-2}$	$1.84\cdot10^{-2}$	$-6.87\cdot10^{-2}$	$9.78\cdot10^{-2}$	$2.11\cdot10^{-1}$
B_8	$5.81\cdot10^{-5}$	$2.69\cdot10^{-4}$	$6.93\cdot10^{-3}$	$-1.20\cdot10^{-2}$	$-2.31\cdot10^{-2}$
B_9	$-4.93\cdot10^{-4}$	$-3.15\cdot10^{-4}$	$1.34\cdot10^{-3}$	$-2.02\cdot10^{-3}$	$-4.21\cdot10^{-3}$
B_{10}	$-4.64\cdot10^{-5}$	$-3.13\cdot10^{-5}$	$7.87\cdot10^{-5}$	$-1.10\cdot10^{-4}$	$-2.39\cdot10^{-4}$
B_{11}	$-1.34\cdot10^{-6}$	$-9.29\cdot10^{-7}$	$1.67\cdot10^{-6}$	$-2.18\cdot10^{-6}$	$-4.94\cdot10^{-6}$
relative error (min)	$-1.14\cdot10^{-3}$	$-7.61\cdot10^{-4}$	$-8.85\cdot10^{-3}$	$-2.24\cdot10^{-2}$	$-1.59\cdot10^{-2}$
relative error (max)	$8.69\cdot10^{-4}$	$5.78\cdot10^{-4}$	$8.43\cdot10^{-3}$	$2.82\cdot10^{-2}$	$2.03\cdot10^{-2}$

Table B.11: Flux Coefficients for positive water ions to conductive particles where $\beta_{k,i} \geq 10^{-15}$ at at 4480 Pa and 218.15 K.

			k		
$B_i(k)$	-2	-1	0	+1	+2
B_0	$-2.56 \cdot 10^{4}$	$-1.51 \cdot 10^{4}$	$7.15 \cdot 10^{3}$	$8.24 \cdot 10^{2}$	$6.58 \cdot 10^{2}$
B_1	$-2.85 \cdot 10^{4}$	$-1.65 \cdot 10^{4}$	$8.09 \cdot 10^{3}$	$7.77 \cdot 10^{2}$	$5.79 \cdot 10^{2}$
B_2	$-1.32 \cdot 10^{4}$	$-7.47 \cdot 10^{3}$	$3.81 \cdot 10^{3}$	$2.75 \cdot 10^{2}$	$1.85 \cdot 10^{2}$
B_3	$-3.15 \cdot 10^{3}$	$-1.74 \cdot 10^{3}$	$9.28 \cdot 10^{2}$	$3.97 \cdot 10$	$2.14 \cdot 10$
B_4	$-3.70 \cdot 10^{2}$	$-1.98 \cdot 10^{2}$	$1.12 \cdot 10^{2}$	$-3.34 \cdot 10^{-2}$	$-8.97 \cdot 10^{-1}$
B_5	-6.17	-2.58	2.21	$-5.34 \cdot 10^{-1}$	$-3.03 \cdot 10^{-1}$
B_6	3.32	1.79	-1.00	$-4.04 \cdot 10^{-3}$	$1.39 \cdot 10^{-2}$
B_7	$2.33 \cdot 10^{-1}$	$1.16 \cdot 10^{-1}$	$-7.50 \cdot 10^{-2}$	$7.97 \cdot 10^{-3}$	$4.09 \cdot 10^{-3}$
B_8	$-2.57 \cdot 10^{-2}$	$-1.39 \cdot 10^{-2}$	$7.69 \cdot 10^{-3}$	$5.51 \cdot 10^{-5}$	$-2.38 \cdot 10^{-4}$
B_9	$-4.67 \cdot 10^{-3}$	$-2.37 \cdot 10^{-3}$	$1.47 \cdot 10^{-3}$	$-1.34 \cdot 10^{-4}$	$-6.26 \cdot 10^{-5}$
B_{10}	$-2.65 \cdot 10^{-4}$	$-1.30 \cdot 10^{-4}$	$8.59 \cdot 10^{-5}$	$-1.23 \cdot 10^{-5}$	$-2.08 \cdot 10^{-6}$
B_{11}	$-5.45 \cdot 10^{-6}$	$-2.60 \cdot 10^{-6}$	$1.81 \cdot 10^{-6}$	$-3.41 \cdot 10^{-7}$	$4.60 \cdot 10^{-8}$
relative error (min)	$-1.70 \cdot 10^{-2}$	$-2.18 \cdot 10^{-2}$	$-8.98 \cdot 10^{-3}$	$-6.23 \cdot 10^{-4}$	$-7.06 \cdot 10^{-4}$
relative error (max)	$2.28 \cdot 10^{-2}$	$2.73 \cdot 10^{-2}$	$8.55 \cdot 10^{-3}$	$4.85 \cdot 10^{-4}$	$7.79 \cdot 10^{-4}$

Table B.12: Steady State distribution for water ions and conductive particles where $\frac{N_k}{Z} \geq 1\mathrm{e}-4$ at at 4480 Pa and 218.15 K.

			k		
$B_i(k)$	-2	-1	0	+1	+2
B_0	$1.46 \cdot 10^{3}$	$2.01 \cdot 10^{4}$	$-1.25 \cdot 10^{3}$	$1.91 \cdot 10^{4}$	$-2.56 \cdot 10^{2}$
B_1	$1.38 \cdot 10^{3}$	$2.24 \cdot 10^{4}$	$-1.25 \cdot 10^{3}$	$2.12 \cdot 10^{4}$	$-2.94 \cdot 10^{2}$
B_2	$4.83 \cdot 10^{2}$	$1.03 \cdot 10^{4}$	$-5.25 \cdot 10^{2}$	$9.77 \cdot 10^{3}$	$-1.40 \cdot 10^{2}$
B_3	$6.59 \cdot 10$	$2.46 \cdot 10^{3}$	$-1.16 \cdot 10^{2}$	$2.32 \cdot 10^{3}$	$-3.01 \cdot 10$
B_4	$-8.39 \cdot 10^{-1}$	$2.86 \cdot 10^{2}$	$-1.27 \cdot 10$	$2.69 \cdot 10^{2}$	-1.45
B_5	$-8.91 \cdot 10^{-1}$	4.50	$-1.61 \cdot 10^{-1}$	4.14	$4.44 \cdot 10^{-1}$
B_6	$9.19 \cdot 10^{-3}$	-2.58	$1.14 \cdot 10^{-1}$	-2.43	$3.28 \cdot 10^{-2}$
B_7	$1.26 \cdot 10^{-2}$	$-1.77 \cdot 10^{-1}$	$7.69 \cdot 10^{-3}$	$-1.65 \cdot 10^{-1}$	$-8.60 \cdot 10^{-3}$
B_8	$-1.84 \cdot 10^{-4}$	$2.00 \cdot 10^{-2}$	$-8.75 \cdot 10^{-4}$	$1.88 \cdot 10^{-2}$	$-5.66 \cdot 10^{-4}$
B_9	$-1.99 \cdot 10^{-4}$	$3.56 \cdot 10^{-3}$	$-1.59 \cdot 10^{-4}$	$3.34 \cdot 10^{-3}$	$1.78 \cdot 10^{-4}$
B_{10}	$-1.45 \cdot 10^{-5}$	$2.00 \cdot 10^{-4}$	$-9.18 \cdot 10^{-6}$	$1.87 \cdot 10^{-4}$	$2.48 \cdot 10^{-5}$
B_{11}	$-2.97 \cdot 10^{-7}$	$4.07 \cdot 10^{-6}$	$-1.94 \cdot 10^{-7}$	$3.80 \cdot 10^{-6}$	$9.20 \cdot 10^{-7}$
relative error (min)	$-2.30 \cdot 10^{-3}$	$-3.66 \cdot 10^{-2}$	$-2.94 \cdot 10^{-3}$	$-3.65 \cdot 10^{-2}$	$-2.01 \cdot 10^{-3}$
relative error (max)	$2.23 \cdot 10^{-3}$	$2.80 \cdot 10^{-2}$	$1.90 \cdot 10^{-3}$	$2.83 \cdot 10^{-2}$	$2.34 \cdot 10^{-3}$

Table B.13: Flux Coefficients for negative “air” ions to polystyrene particles where $\beta_{k,i} \geq 10^{-15}$ at 101325 Pa and 298.15 K.

	k				
$B_i(k)$	-2	-1	0	+1	+2
B_0	$6.37\cdot10^{3}$	$3.97\cdot10^{3}$	$2.58\cdot10^{3}$	$4.55\cdot10^{3}$	$-1.45\cdot10^{4}$
B_1	$6.21\cdot10^{3}$	$3.86\cdot10^{3}$	$3.06\cdot10^{3}$	$5.49\cdot10^{3}$	$-1.57\cdot10^{4}$
B_2	$2.29\cdot10^{3}$	$1.43\cdot10^{3}$	$1.51\cdot10^{3}$	$2.74\cdot10^{3}$	$-7.01\cdot10^{3}$
B_3	$3.49\cdot10^{2}$	$2.21\cdot10^{2}$	$3.85\cdot10^{2}$	$7.10\cdot10^{2}$	$-1.61\cdot10^{3}$
B_4	$8.31\cdot10^{-1}$	2.13	$4.94\cdot10$	$9.19\cdot10$	$-1.79\cdot10^{2}$
B_5	-5.07	-2.95	1.29	2.43	-1.93
B_6	$-6.87\cdot10^{-2}$	$-6.49\cdot10^{-2}$	$-4.35\cdot10^{-1}$	$-8.12\cdot10^{-1}$	1.62
B_7	$8.32\cdot10^{-2}$	$4.56\cdot10^{-2}$	$-3.72\cdot10^{-2}$	$-6.91\cdot10^{-2}$	$9.96\cdot10^{-2}$
B_8	$1.22\cdot10^{-3}$	$1.02\cdot10^{-3}$	$3.29\cdot10^{-3}$	$6.18\cdot10^{-3}$	$-1.27\cdot10^{-2}$
B_9	$-1.54\cdot10^{-3}$	$-7.90\cdot10^{-4}$	$7.08\cdot10^{-4}$	$1.31\cdot10^{-3}$	$-2.08\cdot10^{-3}$
B_{10}	$-1.60\cdot10^{-4}$	$-8.33\cdot10^{-5}$	$4.35\cdot10^{-5}$	$7.97\cdot10^{-5}$	$-1.12\cdot10^{-4}$
B_{11}	$-5.01\cdot10^{-6}$	$-2.59\cdot10^{-6}$	$9.60\cdot10^{-7}$	$1.74\cdot10^{-6}$	$-2.20\cdot10^{-6}$
relative error (min)	$-4.51\cdot10^{-3}$	$-3.52\cdot10^{-3}$	$-7.36\cdot10^{-3}$	$-1.31\cdot10^{-2}$	$-1.88\cdot10^{-2}$
relative error (max)	$4.19\cdot10^{-3}$	$3.79\cdot10^{-3}$	$9.58\cdot10^{-3}$	$1.80\cdot10^{-2}$	$2.22\cdot10^{-2}$

Table B.14: Flux Coefficients for positive “air” ions to polystyrene particles where $\beta_{k,i} \geq 10^{-15}$ at 101325 Pa and 298.15 K.

	k				
$B_i(k)$	-2	-1	0	+1	+2
B_0	$-1.76\cdot10^{4}$	$6.91\cdot10^{3}$	$4.73\cdot10^{3}$	$2.40\cdot10^{3}$	$2.00\cdot10^{2}$
B_1	$-1.91\cdot10^{4}$	$8.14\cdot10^{3}$	$5.46\cdot10^{3}$	$2.28\cdot10^{3}$	$1.29\cdot10^{2}$
B_2	$-8.56\cdot10^{3}$	$3.98\cdot10^{3}$	$2.62\cdot10^{3}$	$8.18\cdot10^{2}$	$1.69\cdot10$
B_3	$-1.98\cdot10^{3}$	$1.01\cdot10^{3}$	$6.51\cdot10^{2}$	$1.21\cdot10^{2}$	-4.16
B_4	$-2.21\cdot10^{2}$	$1.28\cdot10^{2}$	$8.06\cdot10$	$3.52\cdot10^{-1}$	$-8.96\cdot10^{-1}$
B_5	-2.51	3.09	1.81	-1.63	$7.80\cdot10^{-2}$
B_6	2.00	-1.13	$-7.16\cdot10^{-1}$	$-2.16\cdot10^{-2}$	$1.77\cdot10^{-2}$
B_7	$1.24\cdot10^{-1}$	$-9.26\cdot10^{-2}$	$-5.69\cdot10^{-2}$	$2.48\cdot10^{-2}$	$-2.25\cdot10^{-3}$
B_8	$-1.56\cdot10^{-2}$	$8.66\cdot10^{-3}$	$5.46\cdot10^{-3}$	$3.41\cdot10^{-4}$	$-3.04\cdot10^{-4}$
B_9	$-2.59\cdot10^{-3}$	$1.78\cdot10^{-3}$	$1.10\cdot10^{-3}$	$-4.24\cdot10^{-4}$	$5.61\cdot10^{-5}$
B_{10}	$-1.40\cdot10^{-4}$	$1.07\cdot10^{-4}$	$6.59\cdot10^{-5}$	$-4.21\cdot10^{-5}$	$9.93\cdot10^{-6}$
B_{11}	$-2.76\cdot10^{-6}$	$2.30\cdot10^{-6}$	$1.42\cdot10^{-6}$	$-1.25\cdot10^{-6}$	$4.13\cdot10^{-7}$
relative error (min)	$-2.32\cdot10^{-2}$	$-1.47\cdot10^{-2}$	$-9.74\cdot10^{-3}$	$-4.45\cdot10^{-3}$	$-4.26\cdot10^{-3}$
relative error (max)	$2.62\cdot10^{-2}$	$2.02\cdot10^{-2}$	$1.26\cdot10^{-2}$	$4.74\cdot10^{-3}$	$4.81\cdot10^{-3}$

Table B.15: Steady State distribution for “air” ions and polystyrene particles where $\frac{N_k}{Z} \geq 1\mathrm{e}-4$ at 101325 Pa and 298.15 K.

	k				
$B_i(k)$	-2	-1	0	+1	+2
B_0	$2.06\cdot10$	$-1.04\cdot10^{4}$	$-6.12\cdot10^{3}$	$-5.93\cdot10^{3}$	$-4.32\cdot10^{3}$
B_1	$1.65\cdot10^{2}$	$-1.17\cdot10^{4}$	$-6.56\cdot10^{3}$	$-6.59\cdot10^{3}$	$-4.11\cdot10^{3}$
B_2	$1.10\cdot10^{2}$	$-5.41\cdot10^{3}$	$-2.93\cdot10^{3}$	$-3.05\cdot10^{3}$	$-1.49\cdot10^{3}$
B_3	$2.55\cdot10$	$-1.30\cdot10^{3}$	$-6.77\cdot10^{2}$	$-7.36\cdot10^{2}$	$-2.24\cdot10^{2}$
B_4	1.12	$-1.55\cdot10^{2}$	$-7.62\cdot10$	$-8.74\cdot10$	$-7.34\cdot10^{-1}$
B_5	$-3.74\cdot10^{-1}$	-2.77	$-9.68\cdot10^{-1}$	-1.58	3.15
B_6	$-2.25\cdot10^{-2}$	1.39	$6.88\cdot10^{-1}$	$7.84\cdot10^{-1}$	$4.69\cdot10^{-2}$
B_7	$6.82\cdot10^{-3}$	$9.99\cdot10^{-2}$	$4.45\cdot10^{-2}$	$5.67\cdot10^{-2}$	$-5.04\cdot10^{-2}$
B_8	$3.57\cdot10^{-4}$	$-1.07\cdot10^{-2}$	$-5.35\cdot10^{-3}$	$-6.06\cdot10^{-3}$	$-8.15\cdot10^{-4}$
B_9	$-1.33\cdot10^{-4}$	$-1.98\cdot10^{-3}$	$-9.16\cdot10^{-4}$	$-1.12\cdot10^{-3}$	$9.11\cdot10^{-4}$
B_{10}	$-1.70\cdot10^{-5}$	$-1.13\cdot10^{-4}$	$-5.04\cdot10^{-5}$	$-6.42\cdot10^{-5}$	$9.46\cdot10^{-5}$
B_{11}	$-6.00\cdot10^{-7}$	$-2.35\cdot10^{-6}$	$-1.01\cdot10^{-6}$	$-1.33\cdot10^{-6}$	$2.95\cdot10^{-6}$
relative error (min)	$-2.20\cdot10^{-3}$	$-1.21\cdot10^{-2}$	$-6.33\cdot10^{-3}$	$-1.10\cdot10^{-2}$	$-2.66\cdot10^{-3}$
relative error (max)	$2.50\cdot10^{-3}$	$1.01\cdot10^{-2}$	$7.05\cdot10^{-3}$	$7.36\cdot10^{-3}$	$3.06\cdot10^{-3}$

Bibliography

[1] Gunn, R. and Woessner, R.H. (1956). Measurements of the Systematic Electrification of Aerosols. *J. Colloid. Sci.* **11**:254-259.

[2] Wiedensohler, A. (1988). An Approximation of the Bipolar Charge Distribution for Particles in the Submicron Size Range. *J. Aerosol Sci.* **19**:387-389.

Appendix C

Supplemental Material to: The Physics of Extreme Sensitivity in Whispering Gallery Mode Optical Biosensors

Finite Element Model

Calculating the 3-dimensional, transient temperature distribution $T(\mathbf{r}, t)$ at position $\mathbf{r}$ and time t that results from a single-molecule heat source at the interface between a toroidal WGM optical resonator and the surrounding medium is challenging. This task requires integrating the energy balance equation for an arbitrary differential volume element, an expression which may be written as

$$\rho C_P \frac{dT}{dt} + \kappa_T \nabla^2 T = \frac{\omega \alpha \lambda n |\mathbf{E}|^2}{2\pi} + h_{SM} \delta(\mathbf{r} - \mathbf{r_a}), \tag{S1}$$

where ρ is the material density, C_P is the heat capacity , κ_T is the thermal conductivity, and $|\mathbf{E}(\mathbf{r}, t)|$ is the magnitude of the electric field. The right hand side of Eqn. (S1) represent the generation of heat due to absorption by the bulk materials, i.e., silica and water, (first term) and heat due to absorption by a single-molecule bound to the sensor at position $\mathbf{r_a}$ giving off heat at a rate h_{SM} (second term). Here, δ represents the Dirac function.

Calculations were performed numerically, using the finite element (FE) mathematics software COMSOL Multiphysics 4.2. The present work makes the assumption that the thermal plume created by a single molecule will be small enough that the interface between the resonator and the surrounding medium may be approximated as planar, leading to the geometry drawn in Figure C.1. The FE method allows the user to concentrate computation power on regions of the geometry over which the equations apply where the dependent variables change rapidly with position by controlling the size of local mesh elements. We take advantage of this feature by creating numerous subdomains in the geometry, within which the mesh element size is independently described to cut down on computation time by assuming changes in the temperature profile are small near the boundaries of (see Fig. C.1b). The simulated geometry extends 20 μm into each material and 40 μm in each direction along the interface. A cubic subdomain 3 μm in length was defined at the center of the geometry with a maximum mesh size of 50 nm and surrounded by a larger cubic domain 6 μm in length with a maximum mesh size of 1 μm, which encompassed the entire region where temperature changes due to heating exceeded 10^{-7} K.

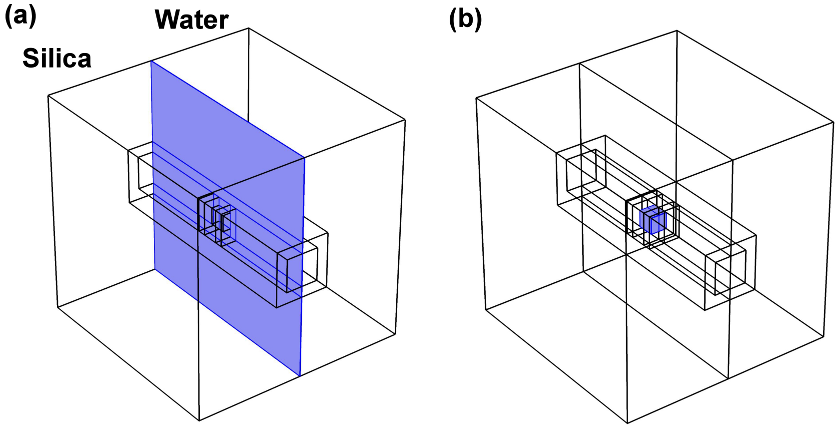

Figure C.1: The geometry used in COMSOL Multiphysics to solve Eqn. (S1) for the transient temperature profile resulting from the excitation of a single-molecule heat source located at what is assumed to be a locally planar interface (blue plane) between a toroidal WGM optical resonator and the water surrounding it. The interior lines are boundaries between subdomains created within the geometry to allow for convenient control over local mesh element size, reducing computation time and memory requirements.

Solving Equation (S1) requires boundary conditions that are applied to all mesh elements that touch an outer boundary of the geometry. The total volume of the system was large compared to the thermal plume that evolves during the WGM sensing experiment to allow us to apply a boundary condition at the extremities holding temperature constant at the ambient value of $T = 298$ K. The boundaries between all other mesh elements was left at their default boundary setting, which COMSOL refers to as *continuity.* This implies that temperature and thermal flux are continuous across each mesh element interface. The point at the center of the geometry, which lies on the interface between silica and water, was designated as a point source of heat that obeys a transient intensity function of

$$h_{SM} = \frac{\sigma \cdot \mathrm{Im}(\mathbf{S})}{4(t-t_0)^2 + \tau_{res}^2}, \tag{S2}$$

where σ is the absorption cross-section of the protein, $\mathrm{Im}(\mathbf{S})$ is the imaginary part of the Poynting vector at the position of the protein, t_0 is the time during the wavelength scan when $\lambda = \lambda_R$, and $\tau_{res} = \lambda/(\frac{d\lambda}{dt}Q)$. This expression describes the Lorentzian profile expected in the absence of bulk heating.

Since we considered resonators with varying quality factors, we evaluate the temperature profile over the geometry at a range of times that were scaled according to τ_{res}. The center of the Lorentzian profile was set to occur at $t = t_0 = 10\tau_{res}$ for all cases. For $0 < t < (t_0 - 2\tau_{res})$ and $(t_0 + 2\tau_{res}) < t < 3t_0$, the time resolution of the calculation was set to $\tau_{res}/6$, while time resolution was improved to $\tau_{res}/60$ during the part of the experiment when significant heat was being generated by the protein, i.e., $(t_0 - 2\tau_{res}) < t < (t_0 + 2\tau_{res})$.

In order to calculate the mode profile, we used methods outlined by Oxborrow [1]. This technique, which uses the axial symmetry of a WGM resonator to simplify the calculation, could not be used directly with our assumption of a locally-planar material interface. We instead mapped the mode onto the planar geometry by using the axisymmetric solution for the mode cross-section as the basis for an interpolation function in the plane normal to propagation and by assuming that the time-averaged mode does not vary in the direction of propagation. The mode profile was used for the weighted calculation of the change in effective refractive index, Δn_{eff}, experienced by the resonant light which may be approximated in terms of the electric field intensity, $|\mathbf{E}(\mathbf{r})|$, using the expression

$$\Delta n_{eff} \approx \frac{\int_V \frac{dn}{dT} \Delta T(\mathbf{r}) |\mathbf{E}(\mathbf{r})| dV}{\int_V |\mathbf{E}(\mathbf{r})| dV}. \tag{S3}$$

The electric field intensity may be easily calculated from the axisymmetric mode profile [1].

The experimental parameters used to predict the WGM optical biosensor response to the binding of a single protein molecule to the surface of an ultra-high Q toroidal resonator in the absence of bulk heating or nonlinear optical phenomena are shown in Table C.1. Material properties for silica and water are also included in Table C.2.

Table C.1: Experimental Parameters for Modeling WGM Biosensing Experiment

Parameter	**Symbol**	**Value**
Quality factor	Q	1×10^8
Driving power	P_D	1 mW
Wavelength scan rate	$\frac{d\lambda}{dt}$	1.35 $\frac{\text{nm}}{\text{s}}$
Wavelength Scan Duration	τ_{scan}	5 ms
Driving pulse FWHM	t_{pulse}	5 μs
Energy flux at the protein	$\text{Im}(\mathbf{S})$	6×10^{13} $\frac{\text{W}}{\text{m}^2}$

Table C.2: Physical Properties of Silica and Water at 298 K and 680 nm

Property	**Symbol**	**Units**	**Silica**	**Water**
Thermal Conductivity	κ_T	$(\frac{\mathrm{W}}{\mathrm{m \cdot K}})$	1.38	0.58
Density	ρ	$(\frac{\mathrm{kg}}{\mathrm{m}^3})$	2203	997
Heat Capacity	C_p	$(\frac{\mathrm{J}}{\mathrm{kg \cdot K}})$	703	4186
Thermo-Optical Coefficient	$\frac{dn}{dT}$	$(\frac{1}{\mathrm{K}})$	1.3×10^{-5}	-9.9×10^{-5}
Refractive Index (Real)	n		1.4694	1.33322
Refractive Index (Imaginary)	k		1.74×10^{-10}	1.41×10^{-8}
Absorption Coefficient	α_{abs}	$(\frac{1}{\mathrm{m}})$	0.0034	0.28

Thermal Effects in WGM Optical Resonators

Absorption by the resonator and its surrounding medium, though often negligible at low coupled power and low quality factor, can be significant for the ultra high Q WGM optical biosensors for which extreme limits of detection have been reported. The warping of the Lorentzian transmission trough that results from absorptive heating and subsequent thermo-optical resonance shift during the wavelength scan could help explain the sensitivity observed in SM1 and SM2. Though no raw data (i.e., transmission spectra) are available for those studies, we can see how similar conditions in Figure SC.2, which include 2.6 mW coupled into a toroidal resonator in water with $Q \approx 10^7$ at $\lambda = 765$ nm, can produce significant broadening of the transmission trough for positive scan rate and narrowing of the trough for negative scan rate. This implies that the methods described above, which assume a Lorentzian time profile for the transient point source of heat, may significantly underestimate the amount of heat put into the system. If taken with a positive wavelength scan rate, data collected during a sensing experiment may be influenced by a heat source with a lifetime that could be orders of magnitude longer than τ_{res}.

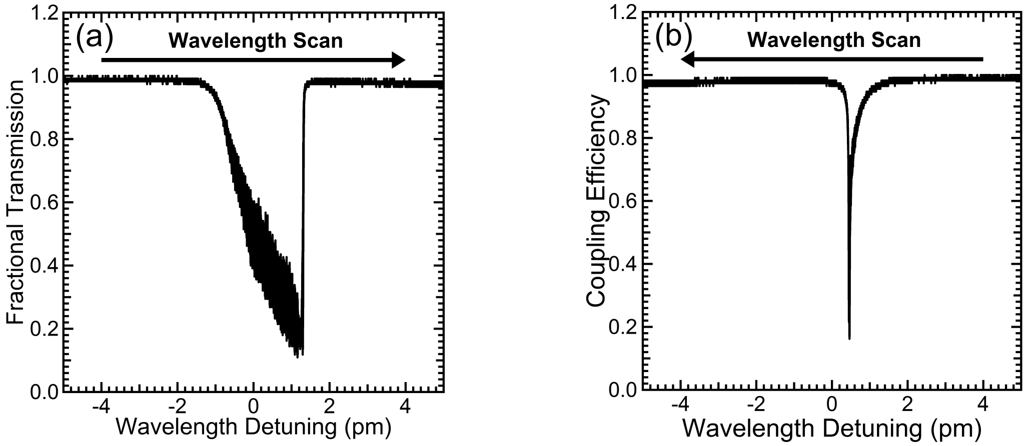

Figure C.2: Transmission spectrum for a toroid of major radius $r_a = 40$ μm and minor radius $r_i = 5$ μm and $Q \approx 10^7$ at wavelength scan rates of (a) $\frac{d\lambda}{dt} = 7.6$ nm/s and (b) -7.6 nm/s. The resonator is submerged in water and is being excited using a 765 nm external cavity tunable laser, with a maximum coupled power of 2.6 mW. The difference in resonance linewidth and transmission minimum is due to thermal distortion of the Lorentzian trough, where λ_R shifts during the scan when light is absorbed and the system warms. Since this warming results in a red shift of λ_R, a positive scan rate leads to an artificially broad line and a negative scan rate yields an artificially narrow line.

Bibliography

[1] Oxborrow, M. (2007). Traceable 2-D finite-element simulation of the whispering-gallery modes of axisymmetric electromagnetic resonators, *IEEE T. Micro. Theory* **55**, 1209.